



UNIVERSIDAD  
**NACIONAL**  
DE COLOMBIA

# **Modelado y simulación del transporte de masa, momentum y energía en una extrusora de plástico mono husillo**

**Fabian Alirio Luna Camacho**

Universidad Nacional de Colombia  
Facultad de Minas, Departamento de Procesos y Energía  
Medellín, Colombia  
2025

# **Modelado y simulación del transporte de masa, momentum y energía en una extrusora de plástico mono husillo**

**Fabian Alirio Luna Camacho**

Tesis presentada como requisito parcial para optar al título de:

**Magister en Ingeniería Química**

Director:

PhD., Juan Carlos Maya López

Codirector:

PhD., Farid Chejne Janna

Línea de Investigación:

Modelamiento y simulación de procesos

Grupo de Investigación:

Termodinámica Aplicada y Energías Alternativas - TAYEA

Universidad Nacional de Colombia

Facultad de Minas, Departamento de Procesos y Energía

Medellín, Colombia

2025



UNIVERSIDAD  
**NACIONAL**  
DE COLOMBIA

# **Modeling and simulation of mass, momentum, and energy transport in a single-screw plastic extruder**

**Fabian Alirio Luna Camacho**

Universidad Nacional de Colombia  
Facultad de Minas, Departamento de Procesos y Energía  
Medellín, Colombia  
2025

# **Modeling and simulation of mass, momentum, and energy transport in a single-screw plastic extruder**

**Fabian Alirio Luna Camacho**

Thesis submitted in partial fulfillment of the requirements for the degree of:  
**Master's degree in chemical engineering**

Advisor:

PhD., Juan Carlos Maya López

Co-advisor:

PhD., Farid Chejne Janna

Research Line:

Modeling and simulation of physicochemical processes

Research Group:

Termodinámica Aplicada y Energías Alternativas - TAYEA

Universidad Nacional de Colombia

Facultad de Minas, Departamento de Procesos y Energía

Medellín, Colombia

2025

*To my mother, for always  
believing in me unconditionally.*

## Acknowledgments

To my mother, for being the person who has always believed in me unconditionally and supported me in every project I have undertaken.

To Minciencias for funding the project “Development of new advanced technologies of Industry 4.0 for SMEs and MSMEs for polymer processing to increase energy and productive efficiency” through contract 127-2022.

To Esenttia S.A., and especially to MSc. Enrique Giovanni Mogollón Rincon, for providing the polypropylene (PP) homopolymer ESENTTIA 05H82-AV material used to collect experimental data for this research.

To the *Instituto de Capacitación e Investigación del Plástico y del Caucho (ICIPC)* and Engineer Nicolás Andrés Muñoz Realpe for their support with time, infrastructure, equipment, and assistance in gathering experimental data.

Finally, to my advisor, Ph.D. Juan Carlos Maya López, and my co-advisor, Ph.D. Farid Chejne Jana, for their support, experience, and knowledge in the development of this research work.

## Resumen

### **Modelado y simulación del transporte de masa, momentum y energía en una extrusora de plástico mono husillo**

Con el objetivo de estudiar y mejorar la predicción de modelos aplicados al proceso de extrusión mono husillo, el proyecto inició con un estudio del estado del arte acerca de modelos utilizados para representar el proceso de extrusión en extrusoras mono husillo, destacando dos grandes enfoques: los modelos de base fenomenológica y los modelos basados en técnicas de soft computing, como redes neuronales artificiales (ANN), lógica difusa, algoritmos genéticos y sistemas expertos.

En este proyecto se desarrollaron y validaron dos metodologías complementarias: un modelo Semifísico de base fenomenológica, y otro basado en redes neuronales artificiales (ANN). Se desarrolló un modelo fenomenológico que contempla los balances dinámicos unidimensionales de masa, momentum y energía. El modelo mostró alta precisión en la predicción de la temperatura del fundido y la predicción del perfil de fundición, así como algunas leves desviaciones en los perfiles intermedios de presión sin perder precisión a la salida.

Seguido de esto se desarrolló un modelo basado en ANN para capturar la naturaleza altamente no lineal del proceso de extrusión, enfocándose en la predicción dinámica del perfil de presión en diferentes ubicaciones de la extrusora. Los resultados obtenidos mostraron una alta precisión obteniendo un coeficiente de determinación ( $R^2$ ) de 0.9889. Este modelo supera en ciertos aspectos al modelo fenomenológico, particularmente en términos de flexibilidad y rapidez ante variaciones operativas.

Finalmente, se recomienda integrar ambos enfoques creando una estrategia híbrida donde se contemplan las fortalezas de cada modelo, empleando el modelo de base fenomenológica para la predicción de la temperatura del fundido para usarla como entrada a la ANN y mejorar la estimación del perfil de presión cuando no se cuenta con sensores para medir esta variable.

**Palabras clave:** extrusión; extrusora mono husillo; modelamiento; perfil de presión; polímeros; polipropileno; predicción, redes neuronales artificiales.

# Abstract

## **Modeling and simulation of mass, momentum, and energy transport in a single-screw plastic extruder**

With the objective of studying and improving the prediction capabilities of models applied to the single-screw extrusion process, the project began with a state-of-the-art review of modeling approaches used to represent extrusion in single-screw extruders. Two main strategies were identified: phenomenological-based models and models based on soft computing techniques, such as artificial neural networks (ANNs), fuzzy logic, genetic algorithms, and expert systems.

In this project, two complementary methodologies were developed and validated: a semi-physical model with a phenomenological basis and another based on artificial neural networks (ANNs). A phenomenological model was developed that incorporates the one-dimensional dynamic balances of mass, momentum, and energy. This model demonstrated high accuracy in predicting melt temperature and the melting profile, with some deviations in intermediate pressure profiles, but without compromising precision at the extruder outlet.

Following this, an ANN-based model was developed to capture the highly nonlinear nature of the extrusion process, focusing on the dynamic prediction of the pressure profile at various points along the extruder. The results showed high accuracy, achieving a coefficient of determination ( $R^2$ ) of 0.9889. This model outperforms the phenomenological model in certain aspects, particularly in terms of flexibility and responsiveness to operational changes.

Finally, it is recommended to integrate both approaches by creating a hybrid strategy that leverages the strengths of each model. The phenomenological model can be used to predict melt temperature, which can then serve as an input to the ANN to improve pressure profile estimation in scenarios where direct temperature sensors are unavailable.

**Keywords:** artificial neural networks; extrusion; modeling; polymers; polypropylene; prediction; pressure profile; single-screw extruder.

# Content

	Pag.
<b>Resumen</b> .....	<b>VII</b>
<b>Figures</b> .....	<b>11</b>
<b>Tables</b> .....	<b>14</b>
<b>Nomenclature</b> .....	<b>15</b>
<b>Introduction</b> .....	<b>21</b>
<b>1. State of the Art</b> .....	<b>25</b>
1.1 Phenomenological-Based Semi-Physical Models .....	25
1.2 Soft Computing Models .....	28
1.2.1 Artificial Neural Networks .....	28
1.2.2 Fuzzy logic.....	29
1.2.3 Genetic Algorithm .....	30
1.2.4 Expert Systems.....	32
1.3 Conclusions.....	32
<b>2. Extrusion Process and Data</b> .....	<b>34</b>
2.1 Process Description .....	34
2.2 Molecular Arrangement of Polymers.....	35
2.3 Geometric Data .....	35
2.4 Experimental Data Collection and Preprocessing .....	37
2.4.1 Rheology .....	38
2.4.2 Determination of the transition temperatures and melting enthalpy of polypropylene .....	38
2.4.3 Extrusion Data .....	39
2.4.4 Operational Curves .....	41
2.5 Conclusions.....	42
<b>3. Phenomenological-Based Semi-physical Model</b> .....	<b>43</b>
3.1 Model Objective .....	43
3.2 Model Hypothesis and Level of Detail.....	43
3.3 Process Systems PS Definition .....	44
3.4 Application of the Conservation Principle and Basic Structure of the Model .....	45
3.5 Basic Structure of the Model .....	47
3.6 Variables, Structural Parameters, and Constants .....	49
3.7 Constitutive and Assessment Equations for Structural and Functional Parameters and the Definition of Constants .....	49
3.8 Degree of Freedom Analysis .....	52

---

3.9	Initial and boundary conditions.....	52
3.10	Computational Model Construction and Validation .....	54
3.11	Model Solution and Result Analysis.....	57
3.12	Conclusions.....	64
<b>4.</b>	<b>Artificial Neural Network Model .....</b>	<b>65</b>
4.1	Model Objective .....	65
4.2	Dimensionality Reduction.....	65
4.3	Feedforward Artificial Neural Networks .....	67
4.4	Results and Discussion.....	68
4.5	Conclusions .....	73
<b>5.</b>	<b>Conclusions and Recommendations .....</b>	<b>74</b>
5.1	Conclusions .....	74
5.2	Recommendations .....	75
<b>A.</b>	<b>Appendix: Development of a Dynamic Model for a Single-Screw Extruder.....</b>	<b>77</b>
	<b>References .....</b>	<b>105</b>

## Figures

	Pag.
Figure 1. Schematic of a single-screw extruder. ....	34
Figure 2. Conventional screw geometry with a diameter ratio $L/D = 30.44$ and a channel width $W = 41.1$ mm. ....	35
Figure 3. Unwrapped channel geometric variables. ....	36
Figure 4. Viscosity of isotactic polypropylene homopolymer. ....	38
Figure 5. DSC Thermograms for Isotactic Polypropylene (ASTM D3418-21).....	39
Figure 6. Single-screw extruder EN045-30, Extrudex Kunststoffmaschinen GmbH (Mühlacker, Germany) with a conventional screw and a smooth feed zone. ....	40
Figure 7. Data collected at 1 s intervals during the extrusion of polypropylene (PP) in a single-screw extruder. The measured data ranges are $Imot$ (0–67.5 A), $\omega$ (0–160.3 rpm), $RDie$ (4.08–4.46 turns), $Tm$ (178.8–213.9 °C), $p1$ (0– 141.1 bar), $p2$ (0–269.5 bar), $p3$ (0–226.6 bar), and $p4$ (11.9–260.8 bar). ....	41
Figure 8. Operational curves. ....	42
Figure 9. Process systems for polypropylene extrusion. ....	44
Figure 10. Fluid elements for balance equations. ....	46
Figure 11. Behavior of polypropylene viscosity in response to shear. ....	51
Figure 12. Pseudocode of the algorithm for the numerical solution of the extrusion process model. ....	55
Figure 13. Experimental data from three independent runs at a fixed die restriction of $RDie = 4.46$ turns, showing the variation of the screw rotational speed ( $\omega$ ) from 0 to 40 rpm, held constant for 230 s; data were collected at 1 Hz. ....	56
Figure 14. Experimental pressure-profile data along the channel of a single-screw extruder at a fixed die restriction of $RDie = 4.46$ turns. Pressures were measured at $p1$ ( $10.3 D$ ), $p2$ ( $18.3 D$ ), $p3$ ( $26.5 D$ ), and $p4$ ( $35.2 D$ ). The screw rotational speed ( $\omega$ ) was ramped from 0 to 40 rpm and then held at 40 rpm for a total of 230 s, with data collected at 1 Hz. a) first run, b) second run, and c) third run. Atmospheric pressure was imposed as the boundary condition at both the inlet ( $p(0D)$ ) and at the outlet $pL$ . ....	56
Figure 15. Experimental melt temperature data obtained from three repetitions of the extrusion process in a single-screw extruder each collected over 230 s at a sampling rate of 1 Hz. ....	57
Figure 16. Initial conditions when $\omega = 0$ for the simulation are applied to a) solid flow area ( $Acs$ ), b) melt flow area ( $Acm$ ), c) solid temperature ( $Ts$ ), d) melt temperature ( $Tm$ ), and e) pressure ( $p$ ). ....	58

Figure 17. Dynamic profiles obtained from the simulation: of a) solid flow area ( $A_{cs}$ ) and b) melt flow area ( $A_{cm}$ ), both as functions of the position $L$ along the extruder at different times. ....	59
Figure 18. Dynamic profiles obtained from the simulation: a) solid temperature ( $T_s$ ) and b) melt temperature ( $T_m$ ), both as functions of the position $L$ along the extruder at different times. ....	60
Figure 19. Dynamic profile obtained from the simulation of the pressure ( $p$ ) along the extruder, expressed as a function of the position ( $L$ ) at different time instants. ....	61
Figure 20. Model validation for the solid flow area $A_{cs}$ was performed by comparing the results with the Tadmor model and with a screw that was extracted from the extruder after the data collection was completed. ....	61
Figure 21. Comparison between the model prediction for the pressure profile and the experimental data corresponding to three repetitions. The gray band represents the standard deviation relative to the experimental mean. ....	62
Figure 22. Model validation for the melt temperature was carried out by comparing the simulation results with experimental measurements obtained using a Thermocomb device positioned at 32.6 D along the extruder. The data were recorded at one-second intervals. ....	63
Figure 23. Correlation matrix from PCA. $Imot$ shows a positive correlation with $\omega$ (0.20) and negative correlations with $T_m$ (-0.13) and $RDie$ (-0.22). Additionally, $\omega$ and $T_m$ exhibit an inverse correlation (-0.30), while $T_m$ and $RDie$ present a weak negative correlation (-0.26). ....	66
Figure 24. Percentage of variance explained by each principal component. Motor current demand ( $Imot$ ) explains most of the data variability (97.1%), while $\omega$ (1.8%), $T_m$ (1.0%), and $RDie$ (0.0%) contribute minimally to the explained variance. ....	67
Figure 25. Diagram of a three-hidden-layer artificial neural network used for predicting the pressure profile in a single-screw extruder, with interconnected neurons processing input features through nonlinear activation functions. ....	70
Figure 26. Scatter plot of the pressure profile ( $p_1, p_2, p_3, p_4$ ) with normalized test data ( $R^2 = 0.9863$ and $MSE = 0.0097$ ). ....	72
Figure 27. Screw radius. ....	79
Figure 28. Internal energy balance in and out of the fluid element in the solids conveying zone. ....	82
Figure 29. Mass balance in and out of the fluid element for the solid bed in the melting zone. ....	85
Figure 30. Internal energy balance in and out of the fluid element for the solid bed in the melting zone. ....	87
Figure 31. Mass balance in and out of the fluid element for melt pool in the melting zone. ....	89
Figure 32. Momentum balance in and out of the fluid element for melt pool in the melting zone. ....	90
Figure 33. Internal energy balance in and out of the fluid element for the solid bed in the melting zone. ....	96

---

Figure 34. Continuity equation in and out of the fluid element for melt in the melt conveying zone. ....	99
Figure 35. Momentum balance in and out of the fluid element for melt in the melt conveying zone. ....	100
Figure 36. Internal energy balance in and out of the fluid element for the solid bed in the melting zone. ....	102

# Tables

	<b>Pag.</b>
Table 1. Studies dedicated to extrusion modeling up to one dimension. ....	27
Table 2. Barrel and die temperature sensors along the extruder. ....	39
Table 3. Pressure sensors along the extruder. ....	40
Table 4. Microscopic and macroscopic balance equations. ....	45
Table 5. Transport equations for the polymer extrusion model. ....	47
Table 6. Gradients for the polymer extrusion model. ....	48
Table 7. Variables, structural parameters, and constants of the model. ....	49
Table 8. Heat transfer terms in PS. ....	49
Table 9. Values of fitted parameters and constants. ....	51
Table 10. Descriptive statistics of the experimental data for the pressure profile and melt temperature. ....	58
Table 11. Mean Absolute Error (MAE) values of the predictions made by the model. ....	63
Table 12. Results of the Feedforward Artificial Neural Network Architectures. ....	68

# Nomenclature

## Latin Letter Symbols

Symbol	Term	Units
$a_1$	Polynomial coefficient for the piecewise function of the screw radius	$m$
$a_2$	Polynomial coefficient for the piecewise function of the screw radius	$m^{-3}$
$a_T$	Temperature shift factor	–
$A$	Constant of the Bird-Carreau model	$Pa \cdot s$
$A$	Area	$m^2$
$A^i$	Activation function	–
$A_0$	Pre-exponential factor	$s^{-1}$
$A_c$	Channel flow area	$m^2$
$A_{cm}$	Melt pool flow area	$m^2$
$A_{cs}$	Solid bed flow area	$m^2$
$A_m$	Heat transfer area of the melt phase	$m^2$
$A_s$	Heat transfer area of the solid phase	$m^2$
$A_T$	Heat transfer area of the two phases	$m^2$
$b_2$	Polynomial coefficient for the piecewise function of the screw radius	$m^{-2}$
$b_3$	Polynomial coefficient for the piecewise function of the screw radius	–
$B$	Constant of the Bird-Carreau model	–
$B^i$	Bias	–
$c_2$	Polynomial coefficient for the piecewise function of the screw radius	$m^{-1}$
$C$	Constant of the Bird-Carreau model	$s$
$C_p$	Specific heat capacity	$\frac{J}{kg \cdot K}$
$C_{pm}$	Melt specific heat capacity	$\frac{J}{kg \cdot K}$
$C_{ps}$	Solid specific heat capacity	$\frac{J}{kg \cdot K}$
$d_2$	Polynomial coefficient for the piecewise function of the screw radius	$m$
$D$	Barrel diameter	$m$
$e_2$	Polynomial coefficient for the piecewise function of the screw radius	–
$E$	Epochs	–
$E_{asm}$	Activation energy for melt rate	$\frac{J}{mol}$
$E_{a\eta}$	Activation energy for viscosity	$\frac{J}{mol}$
$f$	Density of external forces	$\frac{mol}{kg \cdot m^2}$
$f_{ext}$	Extrusion process function	$s^2$
$h$	Channel height	–
		$m$

$HL$	Hidden layer	—
$I$	Identity matrix	$I$
<i>Inputs</i>	Input variables	—
$I_{mot}$	Motor current demand	$A$
$IL$	Input layer	—
$IW^{1,0}$	Weight matrix from the input layer to the first hidden layer	—
$J_k$	Diffusive flux of species $k$	$\frac{kg}{m^3s}$
$K_D$	Constant depending on the die geometry	$m^3$
$L$	Screw length	$m$
$L_c$	Channel length	$m$
$L_D$	Die length	$m$
$LW^{2,1}$	Weight matrix from the first hidden layer to the second hidden layer	—
$LW^{3,2}$	Weight matrices from the second hidden layer to the output layer	—
$M$	Mass	$kg$
$M_k$	Mass of species $k$	$kg$
$\dot{m}$	Mass flow rate	$\frac{kg}{s}$
$\dot{m}_{in}$	Inlet mass flow rate	$\frac{kg}{s}$
$\dot{m}_m$	Melt mass flow	$\frac{kg}{s}$
$\dot{m}_{out}$	Outlet mass flow rate	$\frac{kg}{s}$
$\dot{m}_s$	Solid mass flow	$\frac{kg}{s}$
$n$	Number of data points	—
$\mathbf{n}$	Unit vector	—
$NN$	Number of neurons	—
$Net^i$	Hidden layer equation	—
$O$	Activation function of output layer	—
$OL$	Output layer	—
<i>Ouputs</i>	Output variables	—
$p$	Pressure	$Pa$
$p_{amb}$	Ambient pressure	$Pa$
$p_{in}$	Inlet pressure	$Pa$
$p_{out}$	Outlet pressure	$Pa$
$p_1$	Pressure at $L = 10.3 D$ (solid conveying zone)	$Pa$
$p_2$	Pressure at $L = 18.3 D$ (melting zone)	$Pa$
$p_3$	Pressure at $L = 26.3 D$ (melting zone)	$Pa$
$p_4$	Pressure at $L = 35.2 D$ (melt flow in the die - backpressure)	$Pa$
$Q$	Quartile	—
$\dot{q}'''$	Heat flux	$\frac{J}{s m^3}$
$q_m$	Heat transfer from the barrel to the melt at the die	$\frac{J}{s m^2}$
$q_{zym}$	Heat transfer from the barrel to the melt	$\frac{J}{s m^2}$
$q_{zys}$	Heat transfer from the barrel to the solid	$\frac{J}{s m^2}$
$Q$	Quartile	—
$r$	Screw radius	$m$
$r_{ba}$	Barrel radius	$m$
$\dot{r}_i'''$	Source term for energy balance	$\frac{J}{m^3 s}$
$\dot{r}_k'''$	Source term for mass balance	$\frac{kg}{m^3 s}$

$\dot{r}_s'''$	Melting rate	$\frac{kg}{m^3 s}$
$\dot{r}_u'''$	Source term for momentum balance	$\frac{kg}{m^2 s^2}$
$R_{Die}$	Die restriction	—
$R_g$	Ideal gas constant	$\frac{J}{mol K}$
$R^2$	Coefficient of determination	—
$t$	Time	$s$
$t_f$	Final simulation time	$s$
$T$	Temperature	$K$
$T_{cris}$	Crystallization temperature	$K$
$T_{in}$	Inlet temperature	$K$
$T_{out}$	Outlet temperature	$K$
$T_m$	Melt temperature	$K$
$T_{melting}$	Melting temperature	$K$
$T_{prof}$	Barrel and die temperature profile	$K$
$T_{ref}$	Reference temperature	$K$
$T_s$	Solid temperature	$K$
<i>throughput</i>	Productivity	$\frac{kg}{h m}$
$\mathbf{u}$	Velocity vector	$\frac{s}{m}$
$u_{in}$	Inlet velocity	$\frac{s}{m}$
$u_{out}$	Outlet velocity	$\frac{s}{m}$
$u_{z_m}$	Melt velocity	$\frac{s}{m}$
$u_{z_s}$	Solid velocity	$\frac{s}{m}$
$U_m$	Overall heat transfer coefficient of the melt	$\frac{W}{m^2 K}$
$U_s$	Overall heat transfer coefficient of the solid	$\frac{W}{m^2 K}$
$V$	Volume	$m^3$
$V_{cube}$	Volume of the fluid element for Cartesian coordinates	$m^3$
$V_m$	Volume of the melt in the channel	$m^3$
$V_s$	Volume of the solid in the channel	$m^3$
$V_T$	Total volume in the channel	$m^3$
$W$	Channel width	$m$
$W_m$	Melt pool width in the channel	$m$
$W_s$	Solid bed width in the channel	$m$
$W^i$	Weights	—
$x$	Axis coordinate	$m$
$X_{max}$	Maximum value of the measured data	—
$X_{min}$	Minimum value of the measured data	—
$X_i$	Measured data	—
$\hat{X}_i$	Predicted output	—
$\bar{x}$	Mean	—
$y$	Axis coordinate	$m$
$Y_i$	Normalized data	—
$\bar{Y}_i$	Mean value of the observed data	—
$\hat{Y}_i$	Predicted output	—
$Y_{max}$	Maximum value of the normalized data	—
$Y_{min}$	Minimum value of the normalized data	—

$z$	Axis coordinate	$m$
$z_I(t)$	Length of the solid transport zone	$m$
$z_{II}(t)$	Length of the melting zone	$m$

## Greek letter symbols

Symbol	Term	Units
$ \dot{\gamma} $	Shear rate	$s^{-1}$
$\dot{\gamma}$	Shear rate tensor	$s^{-1}$
$\Delta \hat{h}_{sm}$	Enthalpy of fusion	$\frac{J}{kg}$
$\delta$	Unit tensor	-
$\eta$	Non-Newtonian viscosity	$Pa \cdot s$
$\mu$	Newtonian viscosity	$Pa \cdot s$
$\lambda$	Adaptive learning rate	-
$\rho$	Density	$\frac{kg}{m^3}$
$\rho_k$	Density of species $k$	$\frac{kg}{m^3}$
$\rho_m$	Melt density	$\frac{kg}{m^3}$
$\rho_s$	Solid density	$\frac{kg}{m^3}$
$\rho_{sbulk}$	Bulk density of the solid	$\frac{kg}{m^3}$
$\sigma$	Standard deviation	-
$\omega$	Rotational screw speed	$rpm$

## Abbreviations

Abbreviation	Term
ABS	Acrylonitrile Butadiene Styrene
AI	Artificial Intelligence
ANFIS	Adaptive Neuro-Fuzzy Inference System
ANN	Artificial Neural Network
ARAC	Active Recognition and Adaptive Control
atol	Absolute tolerance
CFD	Computational Fluid Dynamics
CNN	Convolutional Neural Network
CSA	Cuckoo Search Algorithm
DA	Deep Autoencoder
DAE	Differential-Algebraic Equations
DoF	Degree of Freedom
ES	Expert System
FANN	Feedforward Artificial Neural Network
FRBS	Fuzzy Rule-Based System
FLC	Fuzzy Logic Controller
FSMC	Fuzzy Sliding Mode Control
GA	Genetic Algorithms
GPE	Grooved Plasticating Extruders
HDPE	High Density Polyethylene

---

IDE	Integrated Development Environment
LDPE	Low-Density Polyethylene
MAE	Mean Absolute Error
MAP	Mean Average Precision
maxfev	Maximum number of calls to the function
max_step	Maximum allowed step size
MFI	Melt flow index
ML	Machine Learning
MLP	Multilayer Perceptron
MSE	Mean Squared Error
NMSE	Normalized Mean Squared Error
ODE	Ordinary Differential Equations
PAM	Pellet Additive Manufacturing
PBSM	Phenomenological-Based Semi-Physical Models
PC	Principal Components
PCA	Principal Component Analysis
PDE	Partial Differential Equation
PDE-Net	Feedforward Deep Neural Networks
PE	Polyethylene
PID	Proportional-Integral-Derivative
PINN	Physics-Informed Neural Networks
PP	Polypropylene
Ps	Polystyrene
PS	Process System
PS <sub>I</sub>	Process System I (solids conveying zone)
PS <sub>II</sub>	Process System II (melting zone)
PS <sub>III</sub>	Process System III (melting zone – solid bed)
PS <sub>IV</sub>	Process System IV (melting zone – melt pool)
PS <sub>V</sub>	Process System V (melt conveying zone)
PS <sub>VI</sub>	Process System VI (melt flow zone in the die)
PS <sub>VII</sub>	Process System VII (total system)
PSO	Particle Swarm Optimization
PVC	Polyvinyl Chloride
RBFNN	Radial Base Function Neural Network
RF	Random Forests
RMSE	Root Mean Squared Error
RNN	Recurrent Neural Network
RPP	Regrind Polypropylene
RPSGAe	Reduced Pareto Set Genetic Algorithm with Elitism
RSM	Response Surface Methodology
rtol	Relative tolerance
SOSMC	Second Order Sliding Mode Control
SSEM	Single Screw Extrusion Model
UPVC	Unplasticized Polyvinyl Chloride
xtol	Relative tolerance

---



## Introduction

The global production of polymers is approximately 400 million tons per year (Plastics Europe, 2023). The equipment used in polymer processing consumes at least 60% of the total energy in the plant (Kent, 2018) and the specific energy required for its production is estimated to be around  $0.5 \frac{kWh}{kg}$  (Estrada & Janna, 2022). The increasing complexity in polymer manufacturing, driven by applications in industries such as automotive and aerospace, has focused efforts on optimizing these processes to improve product quality and efficiency. This has promoted the adoption of Industry 4.0 protocols and in-line sensors, thus enhancing process understanding and improving data collection for computational models with a high degree of accuracy (Abeykoon et al., 2021).

The simulation of a process is recommended when it presents a high level of complexity or when no simple analytical model that offers sufficient precision is available (Carson, 2005); in such cases, data acquisition eases parameter adjustment or data-driven models in the simulation. Solving mathematical models for various unit operations through simulations is common in chemical engineering; additionally, they are used to optimize and design equipment (De Tommaso et al., 2020). In polymer processes, such as plastic extrusion, where polymer flow occurs under thermal gradients and is subjected to high shear rates, there have been advancements in the modeling of complex physical phenomena such as viscoelastic behavior and crystallization (Hyvärinen et al., 2020). In a single-screw extruder, heat transfer by conduction and viscous dissipation are the predominant sources of heat (Rauwendaal, 2016). Plastic extrusion is achieved by pumping a molten mass of polymers and shaping it through a forming die. A plasticizing unit functions as a pressure builder; its pressure profiles are critical because productivity and process stability depend on them. The most common equipment in the extrusion process is the single-screw extruder (Rauwendaal, 2018), which typically consists of three main zones: feeding or solid transport zone, melting or transition zone, and pumping or metering zone (Dyadichev et al., 2019; Kadyirov et al., 2019).

Modeling extrusion involves addressing phenomena such as solid transport, melting, fluid transport, and melt mixing, and each one presents its own complexity. Melt transport models can be classified into two main categories: one based on geometric and physical conditions, and the other based on the mathematical methodology used (Marschik et al., 2022). The extrusion process can be simulated using CFD (Computational Fluid Dynamics), where most solution methods can solve the Navier-Stokes equations that describe the

conservation of mass, momentum, and energy (Hosain & Fdhila, 2015). CFD software such as Polyflow, developed by ANSYS, have been used recently to simulate single-screw and twin-screw plastic extruders. They predict variables such as residence time, shear stresses, flow patterns, and the variation of temperature and pressure along the screw (Hyvärinen et al., 2020). However, using CFD techniques could have a high computational cost or take too much time, thus hindering its implementation in plant operations (Udoewa & Kumar, 2012).

It is possible to represent polymer flow in plastic extruders using a global 1D or 2D model, provided that the material properties, operating conditions, and screw geometry are known. Most models overlook some relevant parameters to achieve simplifications (Hyvärinen et al., 2020). The melt exiting a polymer extruder must remain uniform throughout the process to ensure the quality of the final product. Variations in melt temperature over time can lead to pressure fluctuations, which may cause changes in production rate, unmelted particles at the outlet, non-uniform product properties, and more. Moreover, it appears that there are not many control techniques that make decisions based on melt quality (Abeykoon, 2016).

The complexity of the phenomena in polymer processing makes its modeling and control more difficult; therefore, the use of Artificial Intelligence (AI) techniques such as expert systems, neural networks, and fuzzy logic are more suitable in these cases (Abeykoon, 2016). For this type of problem, there are diverse types of Artificial Neural Networks (ANNs) such as Multilayer Perceptron (MLP) deep neural networks, which have nonlinear layers and are trained in a supervised manner. That is, input data is used along with their corresponding outputs, parameters are initialized randomly, and the neural network is trained using a gradient descent algorithm and backpropagation (Patel et al., 2018). When a validated model is available, it is possible to create a database under different operating conditions to train ANNs that can predict phenomena such as heat transfer (Kim et al., 2022).

The growth in data availability and computing capacity, data analysis, and advancements in AI have renewed some scientific disciplines. However, when analyzing biological, physico-chemical, or engineering systems, data acquisition is often expensive; therefore, they become inaccessible and lead to decision making based on incomplete information. This issue can be addressed by leveraging prior knowledge on physical and biological phenomena that can serve as regulator to constrain the solution space for neural networks, resulting in a broader perspective for the algorithm based on the supplied data (Raissi et al., 2019). The development of sensors and the increase in data storage capacity provide the opportunity to apply physical laws using data; for instance, Feedforward Deep Neural Networks (PDE-Net) to solve partial differential equations, or Physics-Informed Neural Networks (PINN) (Cai et al., 2021; Long et al., 2018). PINN, also known as Physics-Informed Machine Learning (PIML), incorporates physical differential equations into the loss function (Faegh et al., 2025). ANNs are a branch of AI and can be used in cases where parameters and mathematical models are lacking, or the models are too complex for the desired application.

One-dimensional models provide an adequate balance between computational complexity and accuracy, making them ideal for industrial applications. Therefore, developing a non-stationary one-dimensional model of a single-screw extruder that considers the feeding and melting zones can help control critical variables and optimize the process to obtain a high-quality final product (Chapter 1.1). On the other hand, a regression model based on artificial neural networks trained with data from a single-screw extruder can be implemented as a virtual sensor (Chapter 1.2.1).

### *Research question*

How can the plastification and pressure profiles along a single-screw extruder be predicted without using direct contact sensors with the melt?

### *Hypothesis*

It is possible to predict the plastification and pressure profile along a single-screw extruder using mathematical models and process data.

### *General Objective*

Evaluate the phenomena of plastification, energy consumption, and the transport of mass, momentum, and energy in the polymer extrusion process by coupling the solid transport zone and the plastification zone in a single-screw extruder.

### *Specific objectives*

1. To understand the stages and mechanisms of mass, momentum, and energy transport involved in the polymer extrusion process in single-screw extruders.
2. To develop a mathematical model capable of predicting mass, momentum, and energy transport phenomena in the polymer extrusion process using a single-screw extruder.
3. To predict the plastification profile along a single-screw extruder under different operating conditions.

This research is conducted within the framework of the project "*Desarrollo de nuevas tecnologías avanzadas de la industria 4.0 para pymes y mipymes de procesamiento de polímeros para el incremento de la eficiencia energética y productiva*" through contract 127-2022, which was selected in Call 914 of the *Minciencias* for funding. Within the dynamics of the project, this thesis contributed to the development of a mathematical model to predict the plastification profile and an AI model to predict the pressure profile along a single-screw extruder. This contribution enables the optimization of operating conditions and enhances the efficiency of the polymer extrusion process in single-screw extruders, facilitating the application of models in production while also contributing to the generation of new knowledge. The research outcomes include two simulation software and three scientific articles:

### *Software*

1. POLYEXTRUDER\_1”, is a simulation software for the extrusion process in single-screw extruders, which is registered with the *Dirección Nacional de Derecho de Autor (DNDA)* - *Ministerio del Interior Libro-Tomo-Partida: 13-102-114* with registration date December 23, 2024.
2. “PSensor-Ext (v1.0)”, is a pressure profile prediction software using ANN, with potential use as a virtual sensor, which is currently awaiting the registration certificate from the *DNDA*.

### *Scientific articles*

1. “Modeling and simulation of mass, momentum, and energy transport in a single-screw plastic extruder”, have been submitted.
2. “Predicting Pressure Profiles in Polymer Extrusion Processes Using Artificial Neural Networks”, has been accepted.
3. “Optimization and Sensitivity Analysis of Artificial Neural Networks for Predicting Melt Pressure in Polymer Extrusion Processes”, have been submitted.

### *Scientific contributions*

1. A one-dimensional dynamic model was developed that accurately predicts the melt temperature profile, the plastification profile, and the pressure profile along the screw, thus filling a gap in the literature by providing a 1D model capable of performing these predictions dynamically.
2. For the first time, the pressure profile along a single-screw extruder was predicted using feedforward neural networks. While the literature commonly reports the use of variables such as screw speed and barrel temperature, no studies were found that incorporated variables like motor current, die restriction, and melt temperature—key factors that enabled the model to achieve  $R^2$  values close to 0.99. The technical and computational feasibility of using feedforward neural networks as virtual sensors for predicting the pressure profile in single-screw extruders was demonstrated.
3. In an unprecedented analysis, an exhaustive exploration of artificial neural network models was applied, combining optimization and sensitivity analysis to predict melt pressure in extrusion.

# 1.State of the Art

## 1.1 Phenomenological-Based Semi-Physical Models

When the polymer extrusion process in a single-screw extruder is modeled one-dimensionally (1D), it results in lower complexity, reducing simulation time compared to two- and three-dimensional models, making it useful for industrial applications (Grimard et al., 2016). In the literature, several models have been applied to polymer extrusion in single-screw extruders. Due to the complexity of the phenomena involved in this process, most models are 2D or 3D and are typically solved using specialized software. The following are authors who have proposed up to 1D models based on simplifications that can be justified.

Kroesser & Middleman (1965) developed a model focused on non-Newtonian fluids characterized by the power-law to describe the flow characteristics in single-screw extruders. Using a momentum balance, they analyzed the screw's geometric characteristics, volumetric flow, and pressure, providing a theoretical framework for evaluating extruder performance under different operating conditions and geometries. Flumerfelt et al. (1969) formulated a steady-state mathematical model for two infinite parallel plates (generalized Couette flow) and analyzed fluids with non-Newtonian power-law viscosities. This model applies to single-screw extruders. Lovegrove & Williams (1973) proposed a steady-state model to study the role of gravitational force in pressure generation within the solid conveying zone, enabling estimates of the number of screw revolutions required to establish the pressure buildup process. They used Polyethylene (PE) as reference material.

A dynamic model of plasticizing extruder for the melting zone was developed by Tadmor et al. (1974), considering the fusion and transport of solids and melt. They obtained dynamic profiles of the solid bed width, pressure, and temperature by varying operating conditions such as screw speed. The model was qualitatively validated through simulations and experimental observations using Low Density Polyethylene (LDPE). Worth et al. (1977) analyzed the effect of wall slip on flow and energy consumption in the metering zone through the construction of a one-dimensional model. The viscosity for non-Newtonian fluids was described using a power-law. High Density Polyethylene (HDPE), LDPE, and silicone fluid were used for model validation. Guerrero & Carreau (1993) formulated a macroscopic energy balance model for the five heating zones of the single-screw extruder barrel they used, achieving dynamic predictions of barrel and polymer temperatures as well

as pressure profiles. The model's predictions were validated using experimental data obtained from the processing of LDPE and Polystyrene (Ps).

Wilczyński (1996) proposed a stationary one-dimensional computational model, incorporating the hopper, solid conveying, delay, melting, melt conveying, and die zones. To calculate the velocity of the molten film and temperature profiles in the melt, a power-law model with temperature-dependent viscosity was used. The model enables predictions of mass flow rates, pressure profiles, and temperature distributions and was validated using experimental data obtained from LDPE processing. Lai & Wen (2000) analyzed the plasticizing process using algebraic equations derived from conservation laws, resulting in a steady-state one-dimensional model. The model successfully predicts solid bed width, as well as temperature and pressure profiles, and was validated using experimental data from the processing of HDPE and LDPE.

The implementation of software to simulate the process was carried out by K. Wilczyński et al. (2013). They used the Single Screw Extrusion Model (SSEM) software, which is based on Tadmor's melting model. They proposed models under starved feeding conditions for a two-stage melting mechanism. The first stage involves conductive melting in the partially filled screw zone, where melting occurs mainly due to heat conduction. The second stage involves dispersed melting in the fully filled zone, where melting is dominated by viscous dissipation. The proposed model incorporates mass and energy balances and was validated using experimental data from Polypropylene (PP) processing. The SSEM software was also used by Wilczyński et al. (2014) to iteratively simulate the process using elemental segments of the screw channel. The model incorporates energy, mass, and momentum balances, obtaining profiles of solid fraction, pressure, and temperature while considering all zones of the screw and the die. The model was validated using experimental data from the processing of LDPE and PP.

Roland & Miethlinger (2018) established a steady-state model for non-Newtonian flow considering a power-law for molten polymers and analyzed viscous dissipation in the melt conveying zone. They validated the calculations with analytical solutions for velocity and dissipation profiles in the Newtonian case. Estrada & Janna (2022) developed a steady-state one-dimensional model for Grooved Plasticating Extruders (GPE) based on mass, momentum and energy balances. They introduced the concept of "transition layer removal," which explained the improvement in production and energy efficiency of GPE. The model calculates the volume fraction and temperature profile of the solid region, transition region, and plasticized polymer. They used PP homopolymer for viscosity estimation and parameter fitting of the Carreau-Arrhenius viscosity model.

Campbell et al. (2022) developed a 1D model of the melting mechanism when the film does not encapsulate the solid bed, allowing the estimation of the beginning and end of the solid bed in the melting zone. They compared their results with the model by Tadmor et al. (1974). Pricci et al. (2023) analyzed the Pellet Additive Manufacturing (PAM) process in material extrusion based on an analytical model that describes the entire process, considering the solid conveying, delay, and compression zones. The model allows for the

determination of mass flow rate, pressure profile, and melting profile for a given screw speed. Additionally, it was validated using experimental data from Acrylonitrile Butadiene Styrene (ABS) processing and CFD simulations. Table 1 presents a summary of one-dimensional models derived from transport phenomena.

Table 1. Studies dedicated to extrusion modeling up to one dimension.

Reference	Material	Zone	Melt Viscosity Model	Global Model Dimension	Non-Steady State	Balances		
						Mass	Momentum	Energy
Kroesser & Middleman (1965)	-	Solid conveying, Melting, Melt conveying	Power-law	1	x	x	✓	x
Flumerfelt et al. (1969)	-	Melt conveying	Power-law	1	x	x	✓	x
Lovegrove & Williams (1973)	PE	Solid conveying	-	1	x	x	✓	x
Tadmor et al. (1974)	LDPE	Melting	Power-law	1	✓	✓	x	✓
Worth et al. (1977)	HDPE, LDPE	Melt conveying	Power-law	1	x	x	✓	x
Guerrero & Carreau (1993)	LDPE, Ps	Solid conveying, Melting, Melt conveying	-	0	✓	x	x	✓
Wilczyński (1996)	LDPE	Hopper, Solid conveying, Delay, Melting, Melt conveying, Die	Power-law	1	x	✓	✓	✓
Lai & Wen (2000)	HDPE, LDPE	Solid conveying, Melting, Melt conveying	Power-law	1	x	✓	✓	✓
Wilczyński et al. (2013)	PP	Melt conveying	Klein equation	1	x	✓	x	✓
Wilczyński et al. (2014)	LDPE, PP	Solid conveying, Delay, Melting, Melt conveying, Die	Klein equation	1	x	✓	✓	✓
Roland & Miethlinger (2018)	-	Melt conveying	Power-law	1	x	✓	✓	✓
Estrada & Janna (2022)	PP	Melting	Carreau-Arrhenius	1	x	✓	✓	✓
Campbell et al. (2022)	PP	Melting	-	1	✓	✓	✓	x
Pricci et al. (2023)	ABS	conveying, Delay, Melting	Power-law	1	x	✓	x	✓

## 1.2 Soft Computing Models

Several studies have been conducted to predict mass, pressure and temperature profile in solid transport zone, melting zone, and metering zone; however, due to the simplifications made to find analytical solutions, they are unable to capture the dynamic changes in the process. Some authors have opted for soft computing techniques to model plastic extrusion. The common techniques in soft computing include fuzzy logic, genetic algorithms, expert systems, and neural networks. The latter technique is part of deep learning, a branch of machine learning (Ibrahim, 2016; Kamble & Rewaskar, 2020; Nădăban, 2022).

### 1.2.1 Artificial Neural Networks

Machine Learning (ML) learns automatically from specific data, enabling the construction of models that automate tasks such as clustering, classification, and regression, thereby creating intelligent systems with greater efficiency. Deep Learning, a subset of ML, is based on Artificial Neural Networks (ANNs) and is capable of processing high-dimensional data, such as time sequences, text, and images (Janiesch et al., 2021). ANNs have proven to be a highly impactful tool, as these models have enabled the reduction of waste, optimization of operating parameters, and prediction of properties in extrusion processes. For this reason, research has increasingly adopted these techniques, as shown below.

Using experimental data from the micro-extrusion process, Mekras & Artemakis (2012) trained a deep neural network with two hidden layers. They considered three input features and nine outputs for the ANN. By calculating most of the process parameters required for sizing a microtube and the type of material, they achieved an approximation with an error of less than 1%. Ong et al. (2019) investigated the effects of process parameters on extruded PP filaments. To identify factors affecting the diameter, they used statistical methods and proposed predictive models, Radial Base Function Neural Network (RBFNN) and Response Surface Methodology (RSM), for filament diameter, achieving MSE values of 0.0245 and 0.0029, respectively. Cuckoo Search Algorithm (CSA) and Particle Swarm Optimization (PSO) were employed for parameter optimization. Adesanya et al. (2020) predicted process parameters in the insulation of electrical cables using thermoplastic Polyvinyl Chloride (PVC). They employed an MLP-ANN model with 9 input neurons, two hidden layers with 50 and 40 neurons, respectively, and 11 neurons in the output layer. The model achieved an MSE of  $8.496995 \times 10^{-6}$  and an  $R^2$  of 0.97736 on the test data.

Roland et al. (2021) predicted the nonlinear relationship between flow rate and pressure in single-screw extruders. They used ANN models, gradient boosted trees, and symbolic regression based on genetic programming. Their study relied on simulated data from ANSYS, modeling the melt transport of a non-Newtonian fluid with temperature-independent power-law behavior. They identified four independent parameters: the power-law exponent  $n$ , the dimensionless pressure gradient in the downstream channel, the screw pitch ratio, and the ratio of channel height to width, thus describing the flow rate prediction.

Wang et al. (2023) developed a soft sensor for material viscosity using physical sensors for four temperature signals and one pressure signal, a temperature estimator, and simulation software for calculating material properties. They used Random Forests (RF) and Convolutional Neural Network (CNN) in conjunction with a temperature estimator for their predictions. The use of the temperature estimator reduced the Mean Absolute Error (MAE) from 6.08 to 2.68, and the prediction error rate of the soft sensor decreased from 4% to 1.1%. To predict the melting pressure, Perera et al. (2023) trained an ANN with MLP architecture and achieved good predictive performance with a Normalized Mean Squared Error (NMSE) of  $0.045 \pm 0.003$ . Furthermore, they found that there are no previous works on predicting melting pressure using deep learning techniques.

Perera et al. (2024) proposed an intelligent controller based on an Adaptive Neuro-Fuzzy Inference System (ANFIS) to regulate melt pressure by manipulating screw speed to minimize fluctuations. They combined a Deep Autoencoder (DA) with an MLP-ANN and used the hyperparameters fine-tuned in their previous study by Perera et al. (2023). Experimental data collection was conducted using virgin HDPE. The neuro-fuzzy model learned 49 fuzzy rules and combined the conditions of each rule. They achieved an RMSE of 0.010003 after 10 iterations. Naghipour et al. (2024) optimized the production of Unplasticized Polyvinyl Chloride (UPVC) profiles using ANFIS by controlling variables such as temperature and screw speed. The model has three inputs and one output, with an architecture consisting of five layers: fuzzification, ruling, normalization, evaluation, and defuzzification. The model was trained using 5760 samples, achieving a Mean Average Precision (MAP) of 0.001, RMSE of 0.034, and  $R^2$  of 0.9997.

### 1.2.2 Fuzzy logic

Fuzzy Logic is based on the theory of fuzzy sets proposed by Zadeh (1965). Compared to classical logic, where variables are categorized as either true or false, Fuzzy Logic allows handling intermediate values between 0 and 1, known as degrees of membership. This capability enables the management of imprecision and uncertainty in highly complex systems. Such systems model dynamic processes through components like fuzzification, inference, and defuzzification, along with the use of if-then rules (EL & M, 2024; Mendel, 1995; Precup & Hellendoorn, 2011). In polymer extrusion using single-screw extruders, various authors have applied fuzzy logic for modeling, process control, and improving process parameters such as temperature and melt quality.

Guo et al. (1993) presented an Active Recognition and Adaptive Control (ARAC) system implementing fuzzy logic for the production of tubular structures. The system combines two models: one for pattern analysis to identify operating states and another for adaptive control to dynamically adjust fuzzy rules and membership functions. Taur et al. (1995) applied a fuzzy PID controller to regulate the temperature of an extrusion barrel with four heating zones. The setpoints were 190 °C, 200 °C, 210 °C, and 200 °C. They achieved overshoots of less than 3 °C and average steady-state errors below 0.5 °C. Tsai & Lu (1998) implemented a predictive PID control system supervised by fuzzy logic to regulate the

temperature of an extrusion barrel composed of four heating zones. Using a set of fuzzy rules, they minimized a quadratic cost function.

Chiu & Pong (2000) proposed a fuzzy PID control system to regulate the viscosity of molten polymers. They used screw speed as the manipulated variable, and their nonlinear dynamic model was calibrated using LDPE as the test material and data from five pressure measurements equipped on the extruder. Tan et al. (2004) addressed the modeling of polymer extrusion by building upon the dynamic model developed by Tadmor et al. (1974). They proposed sub models based on a Fuzzy Rule-Based System (FRBS) to approximate sensitive operating parameters, including the melting coefficient, heat transfer rate through the barrel wall, viscous dissipation rate, and viscosity, which were further optimized using Genetic Algorithms (GA-fuzzy). The model was validated through theoretical consistency of predictions and using HDPE melting temperature data obtained from the literature. Yusuf et al. (2010) designed of a Fuzzy Logic Controller (FLC) to regulate the temperature control of molten polymer. They used five membership functions for each variable and optimized their parameters using GA.

To improve thermal homogeneity in the melt, Abeykoon et al. (2011) proposed a control system based on fuzzy logic. They used screw speed and four-barrel temperatures as manipulated variables. To handle the nonlinearities of the process, they integrated two controllers that make decisions based on 30 linguistic if-then rules. The system was validated using HDPE. Abeykoon (2014) introduced a model-based control system integrating a soft sensor and fuzzy logic to predict the melt temperature profile using radial position, barrel temperatures, and screw speed as variables. This approach was validated using HDPE and Regrind Polypropylene (RPP), achieving normalized prediction errors below 3.18%. Shaalan et al. (2020) designed a Fuzzy Sliding Mode Control (FSMC) to regulate screw speed, ensuring a uniform flow within the barrel. They focused on avoiding the chattering phenomenon associated with traditional sliding modes. The performance was compared with a Second Order Sliding Mode Control (SOSMC) and a PID controller, significantly reducing MAE and RMSE with the proposed scheme.

### 1.2.3 Genetic Algorithm

Genetic Algorithms (GA) are inspired by biological selection and natural evolution and are used as search and optimization methods. Through operations such as selection, crossover, and mutation, they explore complex search spaces to optimize solutions for constrained and unconstrained problems. Possible solutions are represented as chromosomes, and their fitness determines the probability of reproduction and producing better-adapted offspring (Lambora et al., 2019; Schmitt, 2001). Over several generations, improved solutions have been generated. GA has been applied in various studies in the field of polymer extrusion to optimize parameters and enhance the quality and efficiency of the process.

In a cable coating extrusion process, McKay et al. (1996) compared the results of GA and Recurrent Neural Networks (RNN) for estimating polymer viscosity, using screw speed and dose rate as inputs. They employed a base polymer and chemical additives (monosil). The RNN achieved an RMSE of 0.122, while the GA achieved 0.116, making GA more robust concerning the nonlinear dynamics of the extrusion process. Cunha et al. (1998) used GA to optimize the extrusion process through an inverse problem. They formulated an objective function and, using GA, identified operating conditions that maximize the objective function. The inputs included the temperatures of three-barrel zones and screw speed, while the outputs were mass throughput and product quality. Gaspar-Cunha & Covas (2004) applied a Reduced Pareto Set Genetic Algorithm with Elitism (RPSGAe). The algorithm uses a clustering scheme to classify solutions and maintains an elitist population, efficiently exploring the search space. The model's objective was to select the geometric and operational variables that maximize the degree of mixing and mass output. McAfee & Thompson (2007) optimized dynamic modeling using a grey-box technique that combined empirical models based on experimental data with GA for control purposes. The proposed viscosity model achieved an RMS of 0.95 %, while the pressure model reached 2.2 %, successfully capturing nonlinear dynamics with high precision.

To identify the most desirable characteristics, Denysiuk et al. (2018) proposed a multi-objective approach. They used RPSGA and Non-dominated Sorting Genetic Algorithm (NSGA-II) combined with mass, momentum, and energy equations, with RPSGA yielding better results. Pareto solutions were generated, enabling the minimization of energy consumption while maximizing production. Nastaj & Wilczyński (2020) optimized extrusion under flood-fed and starve-fed conditions. They utilized Global Screw Extrusion Model (GSEM) and Genetic Algorithms Screw Extrusion Optimization (GASEO) programs. The GSEM integrates screw-die interactions and was used to simulate the process, while GASEO was employed to optimize process parameters, minimizing specific energy consumption and maximizing extrusion throughput.

Nastaj & Wilczyński (2022) developed a computer system for scaling single-screw extruders, evaluating flood-fed and starve-fed conditions using HDPE for testing. They started with process simulation using the GSEM and applied Genetic Algorithms Screw Extrusion Scaling (GASES) for the scaling process. Variables such as melt temperature, plastification profiles, specific energy consumption, and extrusion throughput were considered. The extrusion throughput increased by 63.10 % for flood-fed and 43.37 % for starve-fed conditions. For the optimization of flow and viscous dissipation in the melt conveying zone, Herzog et al. (2024) used a hybrid approach to predict the generalized characteristics of viscous dissipation and pumping. They simulated polymer flows with power-law behavior using ANSYS Fluent software and, to overcome errors from traditional approximations, applied genetic programming with the HeuristicLab software, implementing symbolic regression models.

## 1.2.4 Expert Systems

Expert Systems (ES) are software programs built based on human expert knowledge to make decisions in specific areas. ES consist of a knowledge database, heuristics, and an inference engine that evaluates rules to provide a response. These types of models can be applied where complete data is unavailable and can address flexible and imprecise reasoning. Additionally, they utilize expert knowledge through if-then rules, enabling them to handle both structured and unstructured problems. These models are applied across various industries to solve problems and assist in decision-making (Janjanam et al., 2021; Liao, 2005; C. F. Tan et al., 2016). Various studies have been conducted in the polymer extrusion industry focusing on the development of ES, where they have been used to diagnose production issues and optimize operating conditions.

In the plastic sheet extrusion process, Witt & Gish (1996) proposed an expert system to preserve the knowledge of highly experienced operators, enabling problem-solving on the production floor and achieving high-quality products. The system used decision trees to provide recommendations based on documented information from 50 man-years of accumulated experience, which was implemented into rules and operational procedures. Rawal & Davies (2005) developed an expert system to optimize the production of net structures through melt extrusion. This system combines theoretical modeling and empirical observations to predict the shape and area of filaments. They used LDPE and HDPE and, following an experimental design, evaluated temperature, die speed, extruder speed, melt flow index (MFI), and take-up speed. Expert knowledge was crucial in the development of the autonomous system described by Resonnek & Schöppner (2019). They relied on fuzzy logic to develop an expert system and optimize barrel temperatures across six zones based on the processing of PP and Ps. Golpour Kandeh et al. (2022) developed an expert system for PP production. The system detects and diagnoses faults based on expert knowledge and historical data structured with problem-question-solution rules. They identified extruder stoppage as one of the most frequent failures in the plant and analyzed its faults and possible causes.

## 1.3 Conclusions

The literature review revealed that the majority of single-screw extrusion models are developed in 2D or 3D to capture the rheological and thermal complexity of the process. However, these models are generally computationally expensive, and very few one-dimensional (1D) models were found. Among the few studies identified, none were found to simulate the dynamic 1D profiles of mass, pressure, and temperature in a fully coupled manner throughout the entire extruder. This gap led to the development of a dynamic 1D model.

The complexity of modeling and simulation, along with the high computational cost of extrusion processes, has led various authors to adopt artificial intelligence techniques for the prediction of variables and parameters. In the context of predicting the pressure

---

profile—a variable that serves as a quality indicator of the process—along single-screw extruders, only one study was found that focused on predicting the melt pressure at a single point of the extruder using artificial neural networks. No AI-based model reported to date offers a dynamic reconstruction of the pressure profile, which could be used in situations where physical sensors fail or are unavailable, thus ensuring process continuity while also functioning as a virtual sensor.

## 2. Extrusion Process and Data

### 2.1 Process Description

In polymer extrusion, various physical phenomena occur simultaneously, where solid particles are transported and gradually change to the melt pool due to heat conduction and viscous dissipation (Zhou et al., 2014). The extrusion process in a single-screw extruder can be divided into five zones: I) solid conveying zone, II) pre-melting zone (delay zone), III) melting zone, IV) melt conveying zone, and V) melt flow zone in the die (K. Wilczyński et al., 2019), from which four main zones can be identified as shown in Figure 1.

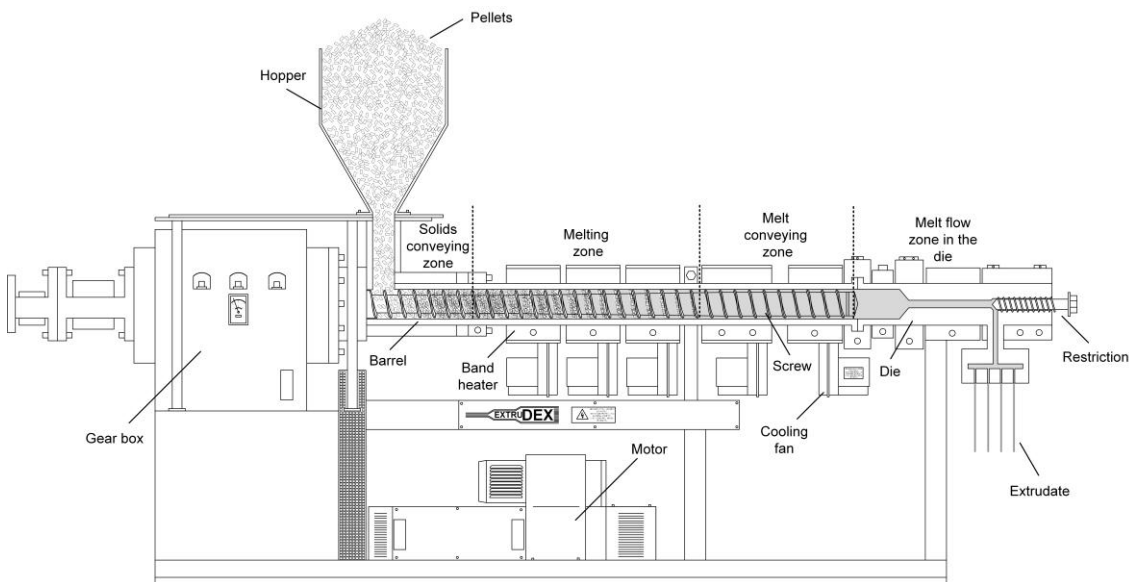


Figure 1. Schematic of a single-screw extruder.

Solids conveying or feeding zone, where pellets or powders are fed from the hopper into the barrel; once the material is in the channel, it is compacted and transported through the screw. Next is the melting or transition zone, which is the section of the extruder where the polymer melts. Then comes the metering or pumping zone (melt conveying), which is the most critical part of the extruder, where the appropriate pressures must be achieved for pumping the molten polymer (Abeykoon, Li, McAfee, Martin, Niu, et al., 2011). Finally, in the melt flow zone in the die, the molten polymer is shaped at the end.

## 2.2 Molecular Arrangement of Polymers

Polymers have different molecular configurations that define their macroscopic characteristics and applications (Greene, 2021; Stokes, 2020). The chains of amorphous polymers are randomly distributed, resulting in a disordered structure that gives them flexibility, transparency, and a well-defined glass transition. However, they do not have a distinct melting point (Mills et al., 2020a). In semicrystalline polymers, ordered regions are interspersed with amorphous zones. In contrast to amorphous polymers, they have a well-defined melting point, greater rigidity, and the presence of lamellar and spherulitic structures, which play a crucial role in their thermal and mechanical behavior (Mills et al., 2020b).

On the other hand, thermosetting polymers exhibit a three-dimensional crosslinked network that stabilizes during the curing process (Xie, Li, et al., 2023). This configuration, based on permanent covalent bonds, provides the material with high thermal and mechanical resistance, as well as dimensional stability, although it limits the possibility of reprocessing (Yue et al., 2020). The fixed structure of thermosets significantly distinguishes them from thermoplastics, and this differentiation is crucial for selecting appropriate materials in applications that require specific durability and performance characteristics.

## 2.3 Geometric Data

Experimental data collection was conducted on a Single-screw extruder EN045-30, Extrudex Kunststoffmaschinen GmbH, Mühlacker, Germany with a conventional screw and a smooth feed zone. The barrel diameter ( $D$ ) is 45 mm, the length to diameter ratio ( $L/D$ ) is 30, and the channel width ( $W$ ) is 41.1 mm. The screw radius ( $r$ ), the barrel radius ( $r_{ba}$ ), and channel height ( $h$ ) are shown in Figure 2. Figure 3 shows the geometric variables of interest for the zones of the single-screw extruder when the channel is unwrapped.

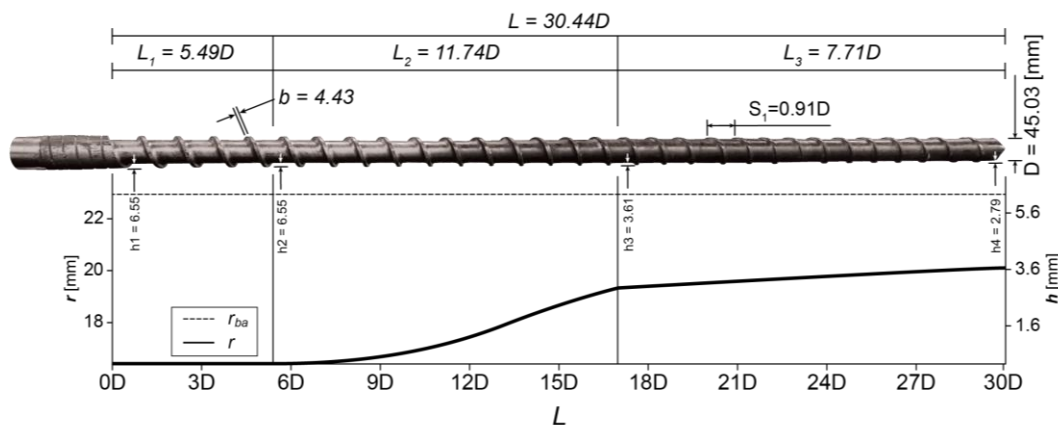


Figure 2. Conventional screw geometry with a diameter ratio  $L/D = 30.44$  and a channel width  $W = 41.1$  mm.

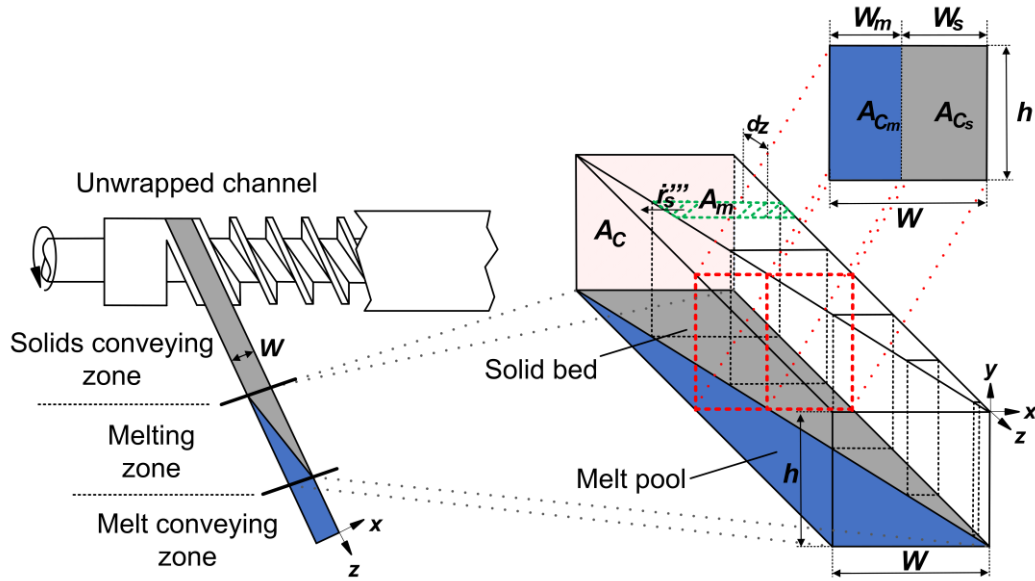


Figure 3. Unwrapped channel geometric variables.

where  $A_c$  is the channel flow area,  $A_{C_s}$  is the solid bed flow area,  $A_{C_m}$  is the melt pool flow area.  $W_s$  and  $W_m$  are the widths of the solid bed and the melt pool in the channel, respectively. The total flow area or cross-sectional area of the channel is given by

$$A_c = A_{C_s} + A_{C_m} \quad (1)$$

$$A_c = hW \quad (2)$$

$$A_{C_s} = hW_s \quad (3)$$

$$A_{C_m} = hW - hW_s \quad (4)$$

from the geometric measurements data taken for the radius  $r$  in Figure 2, a polynomial was fitted for each section of the screw in meters, which is shown in the piecewise function of Equation (5).

$$r = \begin{cases} a_1, & \text{if } z < 0.72 \\ a_2z^4 + b_2z^3 + c_2z^2 + d_2z + e_2, & \text{if } 0.72 \leq z < 1.94 \\ a_3z + b_3, & \text{if } z \geq 1.94 \end{cases} \quad (5)$$

Where  $a_1 = 16.41 \times 10^{-3}$ ,  $a_2 = -27.51 \times 10^{-4}$ ,  $b_2 = 12.82 \times 10^{-3}$ ,  $c_2 = -19.39 \times 10^{-3}$ ,  $d_2 = 12.45 \times 10^{-3}$ ,  $e_2 = 13.49 \times 10^{-3}$ ,  $a_3 = 54.60 \times 10^{-5}$ , and  $b_3 = 18.28 \times 10^{-3}$ . The channel height  $h$  is given by

$$h = r_{ba} - r \quad (6)$$

The heat transfer area of the solid bed with the barrel wall can be viewed as a trapezoid, as shown below

$$A_s = A_T - A_m = \left( W_s|_z + W_s|_{z+\partial z} \right) \frac{\partial z}{2} = \left( A_{c_s}|_z + A_{c_s}|_{z+\partial z} \right) \frac{\partial z}{2h} \quad (7)$$

$$A_m = Wdz - A_s \quad (8)$$

where  $A_T$ ,  $A_s$  and  $A_m$  are the heat transfer area of the two phases, the solid phase, and the melt phase, respectively.  $W_s|_z$  and  $W_s|_{z+\partial z}$  are the channel width of the solid bed at  $z$  and  $z + \partial z$ , respectively. The volume of the solid phase  $V_s$  and the melt phase  $V_m$  in the fluid element are given by

$$V_s = A_s h \quad (9)$$

$$V_m = V_T - V_s \quad (10)$$

$$V_T = A_c dz \quad (11)$$

the total volume  $V_T$  in the fluid element can also be defined as  $V_T = V_s + V_m$ . Additionally, we have  $h = f(z)$ ,  $W_s = f(t, z)$  and  $W_m = f(t, z)$ , where  $t$  is time and  $z$  is the axial coordinate.

## 2.4 Experimental Data Collection and Preprocessing

For experimental data collection, virgin Polypropylene (PP) (semi-crystalline polymer) homopolymer, commercially known as PP, was used. The melt flow index (MFI) is 4.80  $g/10 \text{ min}$  at 230 °C – 2.16 kg (Esentia, 2021). The density of PP is 0.906  $g/cm^3$ , determined using the ISO 1183-1:2019 method (ISO, 2019).

## 2.4.1 Rheology

In polymer engineering, rheology studies the behavior of complex materials during deformation induced by flow (van Puyvelde & Grizzuti, 2020). Rheology is crucial for determining how a polymeric material will respond to processing conditions (Santamaría, 2020). Additionally, viscosity is the most commonly used polymer parameter to determine its behavior during processing. Experimental PP viscosity data were obtained using a Texas Instruments Ares-G2 capillary rheometer (New Castle, Delaware, USA) at temperatures of 190 °C, 210 °C, and 230 °C, with the angular frequency varying between  $0.1 \text{ s}^{-1}$  and  $628 \text{ s}^{-1}$ , as shown in Figure 4.

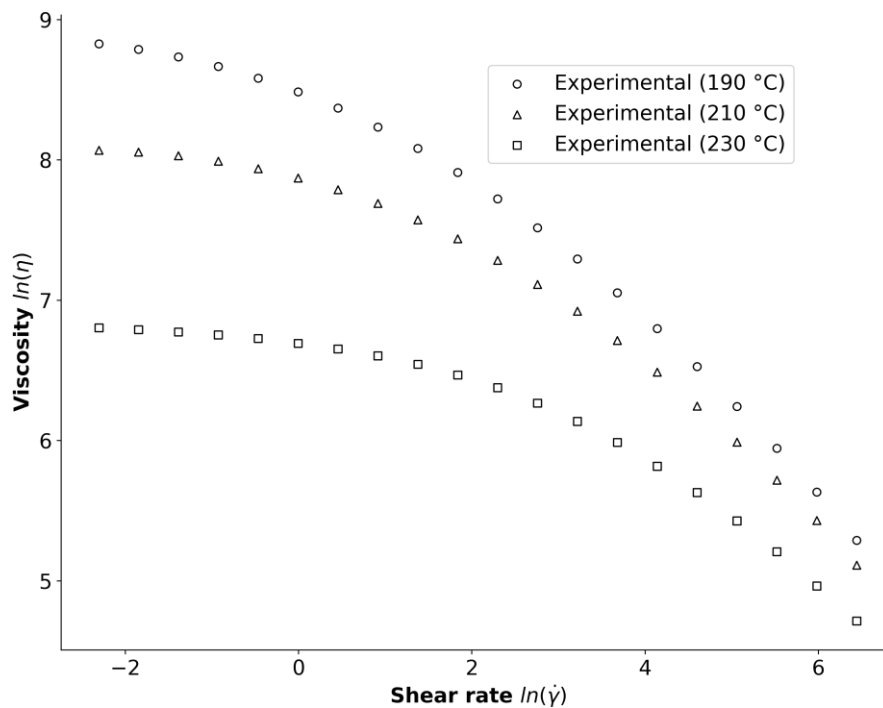


Figure 4. Viscosity of isotactic polypropylene homopolymer.

## 2.4.2 Determination of the transition temperatures and melting enthalpy of polypropylene

Figure 5 presents the differential-scanning-calorimetry (DSC) thermograms of the isotactic polypropylene (PP) homopolymer, recorded on a TA-Instruments DSC Q200 (New Castle, Delaware, USA) performed following the ASTM D3418-21 method (ASTM, 2021). The curve reveals a single, well-defined melting endotherm centered at  $T_{sm} = 164.87 \text{ °C}$ , with an associated enthalpy of fusion of  $\Delta\hat{h}_{sm} = 109.6 \text{ J/g}$ . The absence of secondary peaks confirms the high stereoregularity of the resin, while the magnitude of  $\Delta\hat{h}_{sm}$  is consistent with a crystallinity typical of commercial PP grades. Both thermal parameters fall well within the experimentally established ranges reported for comparable materials in recent studies

(Lanyi et al., 2020; Nabhan et al., 2024; Speranza et al., 2023; Tagashira et al., 2019), providing additional confidence in the quality and representativeness of the sample.

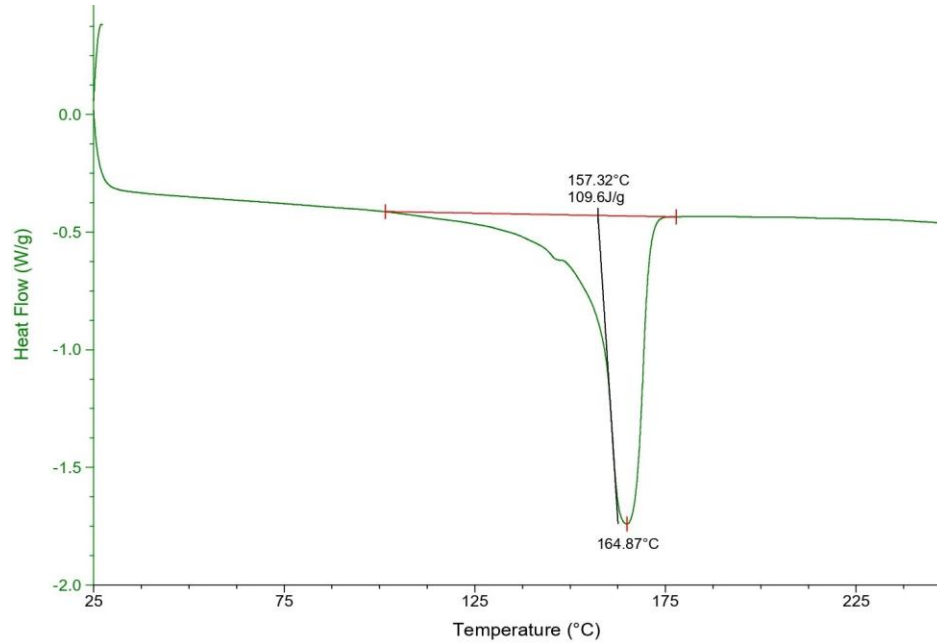


Figure 5. DSC Thermograms for Isotactic Polypropylene (ASTM D3418-21).

### 2.4.3 Extrusion Data

Table 2 presents the barrel and die temperature profile ( $T_{prof}$ ), the length ( $L$ ) at which it is located along the extruder, and the heating zone in which it is found. Each temperature has an independent control system.

Table 2. Barrel and die temperature sensors along the extruder.

Variables	Heating Zone										
	Barrel					Die					
	1	2	3	4	5	6	7	8	9	10	11
$T_{prof}[^{\circ}C]$	160	190	210	220	220	220	220	220	220	220	220
$L/D$	10.3	14.3	18.3	24.3	28.3	30.5	32.3	35.8	41.8	50	54.2

In the extrusion process, there are four independent variables: the material, barrel and die temperature profile ( $T_{prof}$ ), screw rotational speed ( $\omega$ ), and die restriction ( $R_{Die}$ ), the last three are controlled within the extruder (Estrada et al., 2020). Barrel temperature and rotational screw speed variables affect the melting pressure development in the extruder (Abeykoon et al., 2011). In this study,  $T_{prof}$  was not considered but the impact of other measured variables such as motor current demand ( $I_{mot}$ ), rotational screw speed ( $\omega$ ), melting temperature ( $T_m$ ), and die restriction ( $R_{Die}$ ) was evaluated. Table 3 shows the distance of the pressure sensors and the zone in which they were located on the extruder. Figure 6 shows the location of the pressure sensors, the heating zones in the extruder, and

the set of thermocouples in the die to measure the melting temperature (Thermocomb). To collect data on the pressure profile along the extruder, four Dynisco® pressure transducers were installed, as shown in Table 3.  $R_{Die}$  is determined by the mandrel protruding from the end of the extruder, which ranges from 0 to 10 turns, where 0 turns mean fully restricted, and 10 turns means no restriction. Each turn is graduated between 0 and 360°, with increments of 15°.  $I_{mot}$  and  $\omega$  were measured using sensors integrated into the extruder control system. The temperature profile was kept constant during the runs.

Table 3. Pressure sensors along the extruder.

No.	$D$	Zone	Dynisco® Model	Class	Range [bar]
1	10.3 D	Solid Conveying	MDA420-1/2-1.4M-15	1	0-1400
2	18.3 D	Melting	MDA420-1/2-1.4M-15	1	0-1400
3	26.3 D	Melting	MDA420-1/2-1.4M-15	1	0-1400
4	35.2 D	Melt Flow in the Die	Dyna-4-5c-T80	1	0-500

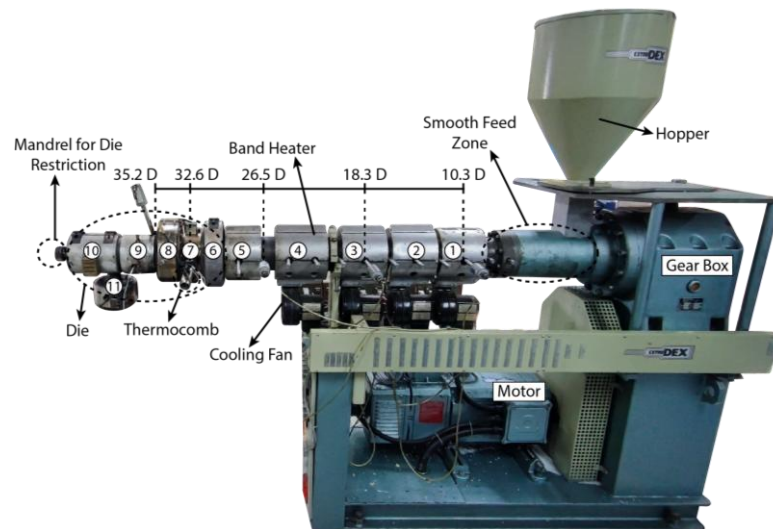


Figure 6. Single-screw extruder EN045-30, Extrudex Kunststoffmaschinen GmbH (Mühlacker, Germany) with a conventional screw and a smooth feed zone.

The sensors used during data acquisition were calibrated before operation, which minimized out-of-range data. Data were collected by varying the  $\omega$  between 0 *rpm* and 160 *rpm*, implementing speed change ramps from 0 *rpm* to 40 *rpm*, then from 40 *rpm* to 100 *rpm*, and finally from 100 *rpm* to 160 *rpm*.  $R_{Die}$  was modified between 4.08 *turns* and 4.46 *turns* to achieve the desired melting pressures. Experimental data collection was carried out in different sessions to ensure variability in the information, and then data were combined into a single dataset. In the first data collection, where  $\omega$  was changed from 0 *rpm* to 40 *rpm*, the process was stopped at 230 s, and the screw was extracted to verify the plastification profile. The extruder's software was configured to collect data at 1-second intervals, resulting in a total of 66,846 data points. System perturbations were conducted each time the process reached a steady state, after waiting for 12 to 15 minutes. During

data processing, adjustments were made to the  $T_m$  data acquired by the thermocouple array in the die (Thermocomb) and to the  $p$  data collected with sensors No. 1 and 2. For the  $T_m$ , due to the presence of 57 out-of-range samples in one of the runs, these values were replaced using linear interpolation, allowing for an estimation based on the adjacent data. Regarding the  $p$  data, some negative values were obtained from sensors No. 1 and 2, as the pressures reached in the solids conveying zone and at the start of the melting zone can be low and affect the sensitivity of the sensors. These data were substituted using linear interpolation based on neighboring values. In the end, the same initial number of data points was preserved for model development. Figure 7 shows the experimental dataset after processing.

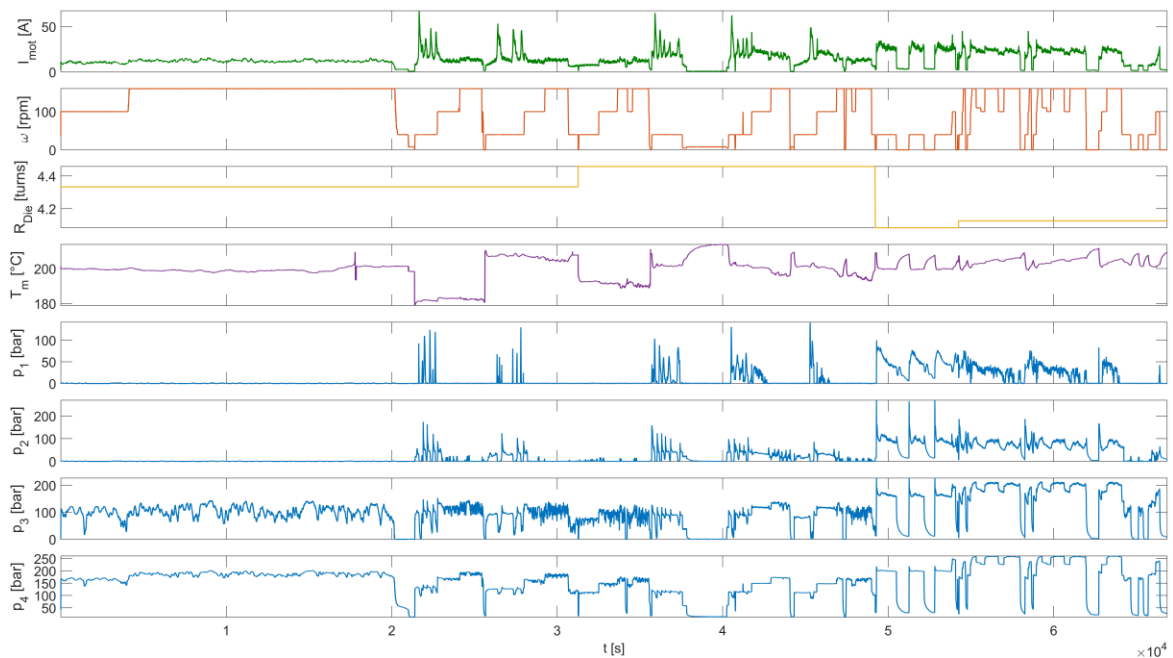


Figure 7. Data collected at 1 s intervals during the extrusion of polypropylene (PP) in a single-screw extruder. The measured data ranges are  $I_{mot}$  (0–67.5 A),  $\omega$  (0–160.3 rpm),  $R_{Die}$  (4.08–4.46 turns),  $T_m$  (178.8–213.9 °C),  $p_1$  (0–141.1 bar),  $p_2$  (0–269.5 bar),  $p_3$  (0–226.6 bar), and  $p_4$  (11.9–260.8 bar).

#### 2.4.4 Operational Curves

The operational curves for PP extrusion are shown in Figure 8, where the independent variables, rotational screw speed ( $\omega$ ) and die restriction ( $R_{Die}$ ), are correlated with the dependent variables, backpressure ( $p_4$ ) and throughput (productivity). These operational curves are highly useful for optimizing operating conditions. In constructing the curves, once the process reached a steady state for each run, every throughput point was measured five times, and pressure was measured once. Three runs were performed for each point to verify the reproducibility of the data, and an average was taken for each point to plot the graph. The three operational curves analyzed here correspond to the mean throughputs ( $throughput = 9.35, 20.32$  and  $27.46$  kg/h) obtained at die restrictions ( $R_{Die} =$

4.13, 4.33 and 4.46 turns), respectively; these operating points are represented by horizontal lines against the measured backpressure ( $p_4$ ). Although the raw dataset also includes an initial setting of  $R_{Die} = 4.08$  turns at the same three screw speeds, that condition lacked replicate runs and was therefore excluded from the present analysis, leaving the three fully replicated conditions (each performed in triplicate) described above.

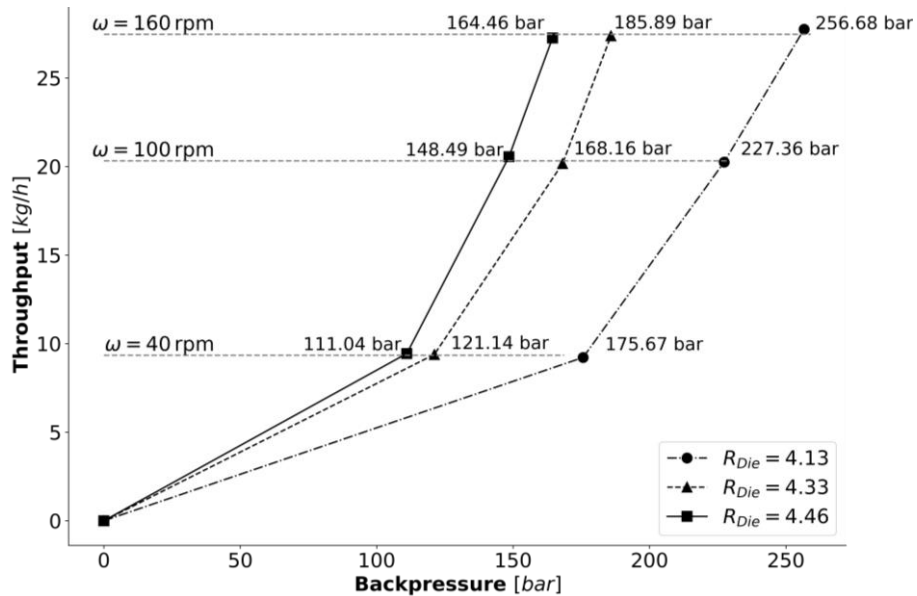


Figure 8. Operational curves.

## 2.5 Conclusions

The acquisition of experimental data and the characterization of the extrusion system highlighted the high complexity of single-screw extrusion processes, as evidenced by the detailed measurement of the screw and barrel geometry, as well as the determination of the rheological parameters and melting point of the polypropylene (PP). In addition, a database was created consisting of  $1 \text{ s}^{-1}$  sampling records of screw rotational speed, melt temperature, and pressure at four strategic points. These measurements were obtained under screw speed perturbations (0–160 rpm) and variations in die restriction.

## 3. Phenomenological-Based Semi-physical Model

The Phenomenological-Based Semi-physical Models (PBSM) is founded on conservation principles and uses empirical equations to evaluate the model parameters. PBSM is distinguished from other types of models by four characteristics: i) the fundamental structure of the model is unique, ii) modularity, iii) the combination of levels of detail, and iv) the interpretability of the parameters (David et al., 2020). Given the process conditions and the phenomena occurring, a PBSM for polypropylene (PP) extrusion is developed from a methodology (Alvarez et al., 2009; Lema et al., 2019; Presiga et al., 2023). The following sections detail how this strategy is applied.

### 3.1 Model Objective

The PBSM developed for a plastic extruder aims to answer the question: how do the plastification, temperature, and pressure change in the PP extrusion process in response to variations in rotational screw speed ( $\omega$ )? The model seeks to determine the profiles of plastification, temperature, and pressure of the polymer along the screw channel, considering the changes in the solid bed and melt pool.

### 3.2 Model Hypothesis and Level of Detail

When modeling the polymer extrusion process, it is necessary to perform a global model that considers the transport of solids, polymer melting, and pumping (K. Wilczyński et al., 2019). Therefore, the level of detail in the model is microscopic in the solid conveying, melting, and melt conveying zones, with the aim of describing the internal dynamics of polypropylene along the extrusion channel. The melt flow zone in the die is considered as a whole, thus the level of detail in this zone is macroscopic. The assumptions that complete the modeling hypothesis are:

- Unsteady state.
- The helical channel of the screw is considered as an unwrapped rectangular flat channel.
- The polypropylene pellets behave like a fluid in the feeding zone.
- The model's domain is two-dimensional, but the model itself is one-dimensional.

- Mass transfer by diffusion is negligible.
- The bulk density of the solid and melt are constant in all zones.
- The solid bed in the melting zone behaves as a rigid and compact solid.
- Gravitational effects are negligible.
- Thermal properties are independent of temperature and pressure.
- The solid bed is adhered to the screw walls.
- The screw walls are insulated; therefore, there is no heat transfer to the screw.
- There is no heat transfer between the solid bed and the melt pool.
- There is no heat transfer between the material and the screw.
- The melt pool has a combined flow of drag and pressure.
- The transient momentum transport in the axial direction dissipates before any substantial change in the location of the material occurs.

### 3.3 Process Systems PS Definition

Process System (PS) are an abstraction modeled over a total or partial volume of the process (David et al., 2020). Seven PS are defined for the PP extrusion process, as shown in Figure 9.

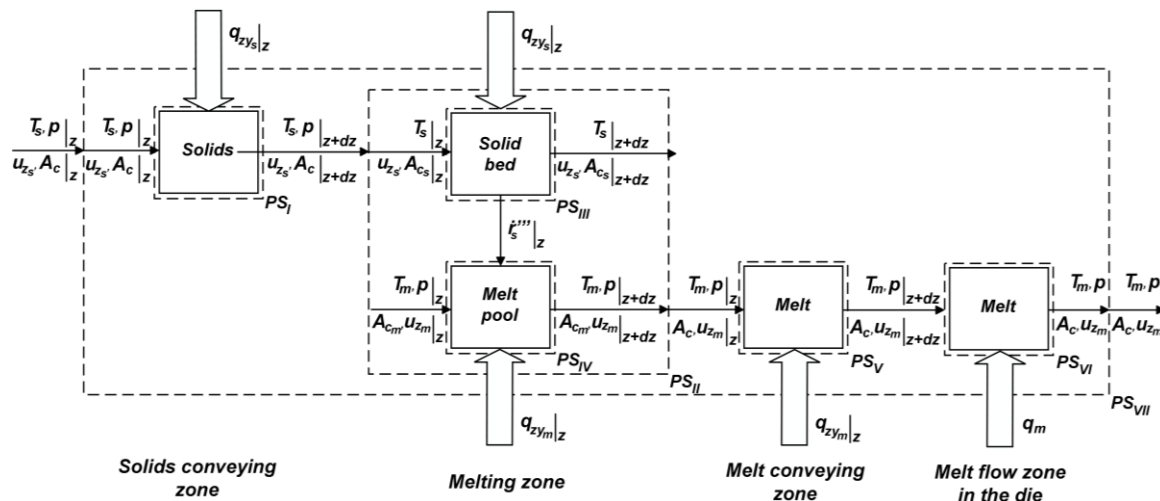


Figure 9. Process systems for polypropylene extrusion.

Depending on the zone, the variables may change with respect to time ( $t$ ), the axial axis ( $z$ ), or both. The following describes each PS:

- **PS<sub>I</sub> (solids conveying zone):** there is a continuous flow of the solids transported through the screw channel and the bulk density ( $\rho_s$ ) is taken as constant. The heat transfer from the barrel to the solid bed ( $q_{zy_s}$ ) occurs at the end of the solids conveying zone. The temperature of the solids ( $T_s$ ), the cross-sectional area of the channel ( $A_c$ ), and the pressure ( $p$ ) vary in this section of the extruder. The velocity of the solids ( $u_{z_s}$ ) may change depending on the length reached by the polymer in the screw channel.

- **PS<sub>II</sub> (melting zone)**: it is the melting process of PP as a whole and is composed of PS<sub>III</sub> and PS<sub>IV</sub>.
- **PS<sub>III</sub> (solid bed)**: the solid bed reaches the melting temperature and melts completely before exiting the melting zone. The temperature ( $T_s$ ), and flow area ( $A_{c_s}$ ) vary in the solid bed, but the bulk density of the solid bed ( $\rho_s$ ) remains constant. The velocity ( $u_{z_s}$ ) of the solid bed may change depending on the length reached by the polymer in the screw channel. There is heat transfer ( $q_{zy_s}$ ) from the barrel to the solid bed in the melting zone.
- **PS<sub>IV</sub> (melt pool)**: the bulk density of the melt pool ( $\rho_m$ ) is constant. The flow area ( $A_{c_m}$ ), temperature ( $T_m$ ), mass flow ( $\dot{m}_m$ ), velocity ( $u_{z_m}$ ), and pressure ( $p$ ) change in the melting pool. There is heat transfer ( $q_{zy_m}$ ) from the barrel to the melt pool in the melting zone. PS<sub>III</sub> interacts with PS<sub>IV</sub> through the melting rate of the solid bed ( $\dot{r}_s'''$ ).
- **PS<sub>V</sub> (melt conveying zone)**: the flow area ( $A_c$ ), temperature ( $T_m$ ), velocity ( $u_{z_m}$ ), mass flow ( $\dot{m}_m$ ), and pressure ( $p$ ) vary along the melt conveying zone until reaching the extruder die, and heat transfer ( $q_{zy_m}$ ) occurs from the barrel to the melt.
- **PS<sub>VI</sub> (melt flow zone in the die)**: temperature ( $T_m$ ), mass flow ( $\dot{m}_m$ ), velocity ( $u_{z_m}$ ), and pressure ( $p$ ) change in the melt flow zone in the die. There is heat transfer ( $q_m$ ) from the barrel to the melt pool.
- **PS<sub>VII</sub>**: it is the single-screw extruder as a whole, formed by the PS described above.

### 3.4 Application of the Conservation Principle and Basic Structure of the Model

The phenomena captured and the quantities considered in the balance equations have both temporal and spatial resolution and distinguish between different types. Fluid flow and heat transfer, based on the fundamental principles of mass, momentum, and energy conservation, form the foundation for the mathematical development of the polymer extrusion model. The microscopic and macroscopic balance equations are presented in Table 4.

Table 4. Microscopic and macroscopic balance equations.

Transport phenomena	Microscopic balance	Macroscopic balance
Continuity equation	$\frac{\partial \rho}{\partial t} + \nabla \cdot (\rho \mathbf{u}) = 0$ (12)	$\frac{dM}{dt} = \sum_{in} \dot{m}_{in} - \sum_{out} \dot{m}_{out}$ (13)
Mass balance per species	$\frac{\partial \rho_k}{\partial t} + \nabla \cdot (\rho_k \mathbf{u}) + \nabla \cdot \mathbf{J}_k = \dot{r}_k'''$ (14)	$\frac{dM_k}{dt} = \sum_{in} \dot{m}_{k_{in}} - \sum_{out} \dot{m}_{k_{out}} + V \dot{r}_k'''$ (15)

$$\begin{aligned}
 \text{Momentum balance} \quad \frac{\partial(\rho \mathbf{u})}{\partial t} + \nabla \cdot (\rho \mathbf{u} \mathbf{u}) &= -\nabla p + \eta \nabla \cdot (\nabla \mathbf{u}) + \rho \mathbf{f} + \dot{r}_u''' \quad (16) \\
 \text{Energy Balance} \quad \frac{\partial(\rho C_p T)}{\partial t} + \nabla \cdot (\mathbf{u} \rho C_p T) &= -\nabla \cdot \dot{\mathbf{q}}''' - \frac{1}{2} \eta (\dot{\gamma} : \dot{\gamma}) + \dot{r}_i''' \quad (18)
 \end{aligned}$$

$$\begin{aligned}
 \frac{d}{dt} \int \rho \mathbf{u} dV &= - \sum_{in} \left( \dot{m}_{in} \frac{\langle u_{in}^2 \rangle}{\langle u_{in} \rangle} + p_{in} A_{in} \right) \mathbf{n}_{in} \\
 &+ \sum_{out} \left( \dot{m}_{out} \frac{\langle u_{out}^2 \rangle}{\langle u_{out} \rangle} + p_{out} A_{out} \right) \mathbf{n}_{out} \\
 &+ \int (p \delta + \eta \nabla \cdot (\nabla \mathbf{u})) dA + \rho \mathbf{f} \\
 &+ V \dot{r}_u''' \quad (17) \\
 \frac{d(M C_p T)}{dt} &= \sum_{in} \dot{m}_{in} C_p (T_{in} - T_{ref}) - \sum_{out} \dot{m}_{out} C_p (T_{ref} - T) \\
 &+ \dot{Q} - \int_{V(t)} \frac{1}{2} \eta (\dot{\gamma} : \dot{\gamma}) dV \\
 &+ V \dot{r}_i''' \quad (19)
 \end{aligned}$$

Where  $t$  is time,  $\rho$  is density,  $\mathbf{u}$  is velocity vector,  $M$  is mass,  $\dot{m}$  is the mass flow rate,  $J$  is the diffusive mass flux,  $p$  is pressure,  $\mu$  is viscosity,  $\mathbf{f}$  is the density of external forces,  $\langle u \rangle$  is the average velocity,  $A$  is the flow area,  $\mathbf{n}$  is the unit vector,  $\delta$  is the unit tensor,  $\tau$  is the shear stress tensor,  $C_p$  is the specific heat capacity,  $T$  is temperature,  $\dot{\mathbf{q}}'''$  is the heat flux,  $\dot{\gamma}$  is the shear rate tensor and  $V$  is volume.  $\dot{r}_k'''$ ,  $\dot{r}_u'''$ , and  $\dot{r}_i'''$  are the source terms for mass, momentum, and energy, respectively. The subscripts  $k$ ,  $in$ , and  $out$  refer to species, inlet, and outlet, respectively.

The fluid is a continuum and macroscopic properties, along with their spatial and temporal derivatives, are used to describe how a fluid behaves. Figure 10 shows small fluid elements in both Cartesian coordinates. The fluid elements are sufficiently small that the first two terms of a Taylor series expansion adequately reflect the fluid characteristics on the faces.

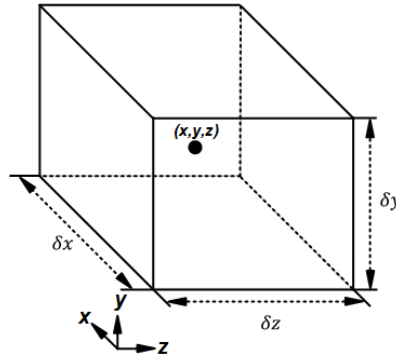


Figure 10. Fluid elements for balance equations.

The differential volume of the fluid element for Cartesian coordinates are given by

$$\delta V_{cube} = \delta x \delta y \delta z \quad (20)$$

for Equation (20), the flow area will be taken as

$$\delta A_c = \delta x \delta y \quad (21)$$

depending on the extrusion zone in which the process is located. However, since the analysis will be performed by differential volumes in slices,  $\delta A_c$  becomes  $A_c$ .

Based on the modeling assumptions, the transport equations for mass, momentum, and energy are defined for a single-screw extrusion process within the four main zones of the extruder, as appropriate. These equations are modified to account for the cross-sectional area or flow area in each region. For the zones within PS<sub>I</sub>, PS<sub>III</sub>, PS<sub>IV</sub>, PS<sub>V</sub>, microscopic balances were applied, while for the zone within PS<sub>VI</sub> macroscopic balances were applied. Below, some considerations taken into account during the model development are outlined.

In PS<sub>I</sub> (solid conveying zone), the solids are approximated as fluid. The physical properties, such as specific heat capacity ( $C_p$ ) and overall heat transfer coefficient ( $U$ ), and bulk densities of the solid ( $\rho_s$ ) and the melt ( $\rho_m$ ) are constant for both the solid and the melt across all PS zones. Since the gradient  $\frac{\partial u_{zm}}{\partial y} \gg \frac{\partial u_{zm}}{\partial z}$  in PS<sub>IV</sub> and PS<sub>V</sub>, it is assumed that  $\frac{\partial u_{zm}}{\partial z} \approx 0$ . In the momentum balances, integration is performed with respect to  $y$ , and the viscous dissipation term is included. From this equation, the average velocity  $\langle u_{zm} \rangle$  is obtained. The complete model development is described in Appendix A.

### 3.5 Basic Structure of the Model

Table 5 and Table 6 present the relevant information needed to answer the questions posed to the model in Section 3.1. The equations for each PS are provided, forming the basic structure of the PBSM that constitutes the single-screw extruder.

Table 5. Transport equations for the polymer extrusion model.

Process System	Transport Phenomena	Equation
PS <sub>I</sub> : solids conveying zone	Momentum	$\frac{\partial u_{zs}}{\partial z} = \omega \frac{\partial r}{\partial z} \quad (22)$
	Energy	$\frac{\partial T_s}{\partial t} = -u_{zs} \frac{\partial T_s}{\partial z} - \frac{u_{zs} T_s}{\rho_s} \frac{\partial \rho_s}{\partial z} - \frac{u_{zs} T_s}{A_c} \frac{\partial A_c}{\partial z} - T_s \frac{\partial u_{zs}}{\partial z} - \frac{1}{\rho_s C_{ps}} \frac{\partial q_{zys}}{\partial z} \Big _0^z - \frac{1}{\rho_s C_{ps} A_c} q_{zys} \Big _0^z \frac{\partial A_c}{\partial z} \quad (23)$
PS <sub>II</sub> : melting zone	Mass	$\dot{m} = \dot{m}_s + \dot{m}_m \quad (24)$
	Mass	$\frac{\partial A_{cs}}{\partial t} = -u_{zs} \frac{\partial A_{cs}}{\partial z} - A_{cs} \frac{\partial u_{zs}}{\partial z} + \frac{A_{cs}}{\rho_s} \dot{s}''' \quad (25)$
PS <sub>III</sub> : solid bed - melting zone	Momentum	$\frac{\partial u_{zs}}{\partial z} = \omega \frac{\partial r}{\partial z} \quad (26)$
	Energy	$\frac{\partial T_s}{\partial t} = -\frac{T_s}{A_{cs}} \frac{\partial A_{cs}}{\partial t} - u_{zs} \frac{\partial T_s}{\partial z} - T_s \frac{\partial u_{zs}}{\partial z} - \frac{u_{zs} T_s}{A_{cs}} \frac{\partial A_{cs}}{\partial z} - \frac{1}{\rho_s C_{ps}} \frac{\partial q_{zys}}{\partial z} \Big _0^z - \frac{1}{\rho_s C_{ps} A_{cs}} q_{zys} \Big _0^z \frac{\partial A_{cs}}{\partial z} - \frac{1}{\rho_s C_{ps}} \Delta \hat{h}_{sm} \dot{s}''' \quad (27)$

	Mass	$\frac{\partial \dot{m}_m}{\partial z} = -\rho_s \frac{\partial A_{cm}}{\partial t} - A_{cm} \dot{s}'''$	(28)
		$\frac{\partial p}{\partial z} = 6 \frac{\eta u_{zs}}{h^2} - 12 \frac{\eta u_{zm}}{h^2} - \frac{p}{A_{cm}} \frac{\partial A_{cm}}{\partial z}$	(29)
PS <sub>IV</sub> : melt pool - melting zone	Momentum	$\frac{\partial u_{zm}}{\partial z} = \frac{1}{\rho_m A_{cm}} \frac{\partial \dot{m}_m}{\partial z} - \frac{\dot{m}_m}{\rho_m A_{cm}^2} \frac{\partial A_{cm}}{\partial z}$	(30)
		$\left\langle \frac{\partial u_{zm}}{\partial y} \right\rangle_{\{0,h\}} = -\frac{u_{zs}}{h}$	(31)
	Energy	$\begin{aligned} \frac{\partial T_m}{\partial t} = & -\frac{T_m}{A_{cm}} \frac{\partial A_{cm}}{\partial t} - \frac{\dot{m}_m}{\rho_m A_{cm}} \frac{\partial T_m}{\partial z} - \frac{T_m}{\rho_m A_{cm}} \frac{\partial \dot{m}_m}{\partial z} - \frac{1}{\rho_m C_{pm}} \frac{q_{zym}}{\partial z} \Big _0^z - \frac{1}{\rho_m C_{pm} A_{cm}} q_{zym} \Big _0^z \frac{\partial A_{cm}}{\partial z} \\ & + 2 \frac{\eta}{\rho_m C_{pm}} \left( \frac{\partial u_{zm}}{\partial z} \right)^2 + 2 \frac{\eta u_{zm}}{\rho_m C_{pm} A_{cm}} \frac{\partial u_{zm}}{\partial z} \frac{\partial A_{cm}}{\partial z} + \frac{\eta}{\rho_m C_{pm}} \left( \left\langle \frac{\partial u_{zm}}{\partial y} \right\rangle_{\{0,h\}} \right)^2 \end{aligned}$	(32)
	Continuity	$\frac{\partial \dot{m}_m}{\partial z} = 0$	(33)
		$\frac{\partial p}{\partial z} = 6 \frac{\eta \omega r}{h^2} - 12 \frac{\eta u_{zm}}{h^2} - \frac{p}{A_c} \frac{\partial A_c}{\partial z}$	(34)
PS <sub>V</sub> : melt conveying zone	Momentum	$\frac{\partial u_{zm}}{\partial z} = \frac{1}{\rho_m A_c} \frac{\partial \dot{m}_m}{\partial z} - \frac{\dot{m}_m}{\rho_m A_c^2} \frac{\partial A_c}{\partial z}$	(35)
		$\left\langle \frac{\partial u_{zm}}{\partial y} \right\rangle_{\{0,h\}} = -\omega \frac{r}{h}$	(36)
	Energy	$\begin{aligned} \frac{\partial T_m}{\partial t} = & -\frac{T_m}{\rho_m A_c} \frac{\partial \dot{m}_m}{\partial z} - \frac{\dot{m}_m}{\rho_m A_c} \frac{\partial T_m}{\partial z} - \frac{1}{\rho_m C_{pm}} \frac{q_{zym}}{\partial z} \Big _0^z - \frac{1}{\rho_m C_{pm} A_c} q_{zym} \Big _0^z \frac{\partial A_c}{\partial z} + \\ & 2 \frac{\eta}{\rho_m C_{pm}} \left( \frac{\partial u_{zm}}{\partial z} \right)^2 + 2 \frac{\eta u_{zm}}{\rho_m C_{pm} A_c} \frac{\partial u_{zm}}{\partial z} \frac{\partial A_c}{\partial z} + \frac{\eta}{\rho_m C_{pm}} \left( \left\langle \frac{\partial u_{zm}}{\partial y} \right\rangle_{\{0,h\}} \right)^2 \end{aligned}$	(37)
PS <sub>VI</sub> : melt flow zone in the die	Continuity	$\dot{m}_{in} = \dot{m}_{out} = \dot{m}_m = \dot{m}$	(38)
	Momentum	$\dot{m}_m = K_D \rho_m \frac{\Delta p}{\eta}$	(39)

Where  $K_D$  is a constant depending on the die geometry and the subscripts  $c$ ,  $s$ ,  $m$ ,  $in$   $y$   $out$  refer to the cross-sectional area, solid, melt, inlet, and outlet, respectively. In Table 6, the gradients that complement the model are shown.

Table 6. Gradients for the polymer extrusion model.

Process System	Gradient	Equation
PS <sub>I</sub> , PS <sub>III</sub> , PS <sub>IV</sub> , PS <sub>V</sub>	Spatial derivative of radius	$\frac{\partial r}{\partial z} = \begin{cases} 0, & z < 0.72 \\ 4a_2 z^3 + 3b_2 z^2 + 2c_2 z + d_2, & 0.72 \leq z < 1.94 \\ a_3, & 1.94 \leq z < 3 \end{cases}$ (40)
PS <sub>I</sub> , PS <sub>III</sub> , PS <sub>IV</sub> , PS <sub>V</sub>	Derivative of Cross-sectional area	$\frac{\partial A_c}{\partial z} = W \frac{\partial h}{\partial z}$ (41)
PS <sub>I</sub> , PS <sub>III</sub> , PS <sub>IV</sub> , PS <sub>V</sub>	Derivative of channel height	$\frac{\partial h}{\partial z} = -\frac{\partial r}{\partial z}$ (42)
PS <sub>III</sub> , PS <sub>IV</sub>	Derivative of the cross-sectional area	$\frac{\partial A_{cm}}{\partial t} = -\frac{\partial A_{cs}}{\partial t}$ (43)

### 3.6 Variables, Structural Parameters, and Constants

Based on the defined basic structure, the variables, structural parameters, and constants of the PSBM are classified. Additionally, all structural parameters need to be included in the degrees of freedom because they are regarded as unknown. The classification is shown in Table 7.

Table 7. Variables, structural parameters, and constants of the model.

Process System	Variables	Constants and Structural Parameters
PS <sub>I</sub> (solids conveying zone)	$A_c, u_{z_s}, T_s, r, h$	$\omega, C_{p_s}, \rho_s, \left. \frac{\partial q_{zy_s}}{\partial z} \right _0^z, q_{zy_s} \Big _0^z$
PS <sub>III</sub> (solid bed - melting zone)	$A_{c_s}, u_{z_s}, T_s, r, h$	$\omega, \rho_s, C_{p_s}, \left. \frac{\partial q_{zy_s}}{\partial z} \right _0^z, q_{zy_s} \Big _0^z, \Delta \hat{h}_{sm}, \dot{r}_s'''$
PS <sub>IV</sub> (melt pool - melting zone)	$A_{c_m}, \dot{m}_m, u_{z_m}(z), u_{z_m}(y), T_m, p, r, h$	$\rho_m, C_{p_m}, \left. \frac{q_{zy_m}}{\partial z} \right _0^z, q_{zy_m} \Big _0^z, \eta, \dot{r}_s'''$
PS <sub>V</sub> (melt conveying zone)	$A_c, \dot{m}_m, u_{z_m}(z), u_{z_m}(y), T_m, p, r, h$	$\omega, \rho_m, C_{p_m}, \left. \frac{q_{zy_m}}{\partial z} \right _0^z, q_{zy_m} \Big _0^z, \eta$
PS <sub>IV</sub> (melt flow zone in the die)	$\dot{m}_m, T_m, p$	$K_D, \eta$

### 3.7 Constitutive and Assessment Equations for Structural and Functional Parameters and the Definition of Constants

For each structural parameter listed in Table 7, a constitutive or assessment equation is developed by integrating sub models from existing literature with empirical equations derived from experimental data or parameter identification. These equations yield new functional parameters. The heat transfer terms in each PS are provided in Table 8.

Table 8. Heat transfer terms in PS.

Process System	Equation
PS <sub>I</sub> (solids conveying zone)	$\left. \frac{\partial q_{zy_s}}{\partial z} \right _0^z = -\frac{A_T U_s}{V_T} (T_{prof} - T_s) \quad (44)$
	$q_{zy_s} \Big _0^z = -U_s (T_{prof} - T_s) \quad (45)$
PS <sub>III</sub> (solid bed - melting zone)	$\left. \frac{\partial q_{zy_s}}{\partial z} \right _0^{dz} = -\frac{A_s U_s}{V_s} (T_{prof} - T_s) \quad (46)$
	$q_{zy_s} \Big _0^{dz} = -U_s (T_{prof} - T_s) \quad (47)$
PS <sub>IV</sub> (melt pool - melting zone)	$\left. \frac{q_{zy_m}}{\partial z} \right _0^z = -\frac{A_m U_m}{V_m} (T_{prof} - T_m) \quad (48)$
	$q_{zy_m} \Big _0^z = -U_m (T_{prof} - T_m) \quad (49)$

PS <sub>V</sub> (melt conveying zone)	$\frac{q_{zy_m}}{\partial z} \Big _0^z = -\frac{A_T U_m}{V_T} (T_{prof} - T_m)$	(50)
	$q_{zy_m} \Big _0^{dz} = -U_m (T_{prof} - T_m)$	(51)
PS <sub>IV</sub> (melt flow zone in the die)	$q_m \Big _0^z = -U_{Die} (T_{prof} - T_m)$	(52)

According to traditional thermodynamic theory, fusion occurs at a constant temperature. While this model is valid across a broad range of scenarios, some compounds may melt slowly and overheat, leading to a temperature rise beyond the equilibrium melting temperature. This indicates that resistance to diffusion may affect the melting rate, allowing for the investigation of its relationship with temperature and the calculation of the activation energy of the process (Vyazovkin, 2020). Some authors have proposed the temperature dependence of the polymer melting rate based on the Arrhenius equation (Cubeta et al., 2017; Lippits et al., 2006; Maffezzoli et al., 1989); this study follows that approach. The melting rate is shown in Equation (53):

$$\dot{r}_s''' = A_0 e^{\left(\frac{-E_{a_{sm}}}{T_s R_g}\right)} \rho_s \quad (53)$$

where  $A_0$  is the pre-exponential factor,  $E_{a_{sm}}$  is the activation energy, and  $R_g$  is the ideal gas constant. The activation energy of a process can be determined by measuring its rate at various temperatures. The viscosity of the melt polymer was calculated using the Bird-Carreau model, as shown in Equation (54), which depends on the shear rate  $|\dot{\gamma}|$  and the melt temperature  $T_m$ . In Equation (55), the Arrhenius equation was used to calculate the temperature shift factor ( $a_T$ ) (Estrada & Janna, 2022).

$$\eta = \frac{a_T A}{(1 + a_T B |\dot{\gamma}|)^C} \quad (54)$$

$$a_T = e^{\frac{E_{a_\eta}}{R_g} \left(\frac{1}{T_m} - \frac{1}{T_{ref}}\right)} \quad (55)$$

Where  $A$ ,  $B$  and  $C$  are constants of the Bird-Carreau model,  $E_{a_\eta}$  is the activation energy for viscosity, and  $T_{ref}$  is the reference temperature.  $|\dot{\gamma}|$  is given by Equation (56).

$$|\dot{\gamma}| = \left[ 2 \left( \frac{\partial u_{z_m}}{\partial z} \right)^2 + \left( \left\langle \frac{\partial u_{z_m}}{\partial y} \right\rangle_{[0,h]} \right)^2 \right]^{0.5} \quad (56)$$

To adjust the viscosity model parameters, experimental PP data were obtained using a Texas Instruments Ares-G2 capillary rheometer (New Castle, Delaware, USA). Figure 11 shows the fit of the viscosity model to the experimental data, achieving an  $R^2$  of 0.9889.

Table 9 lists the values of the constants and the parameters adjusted during the model development.

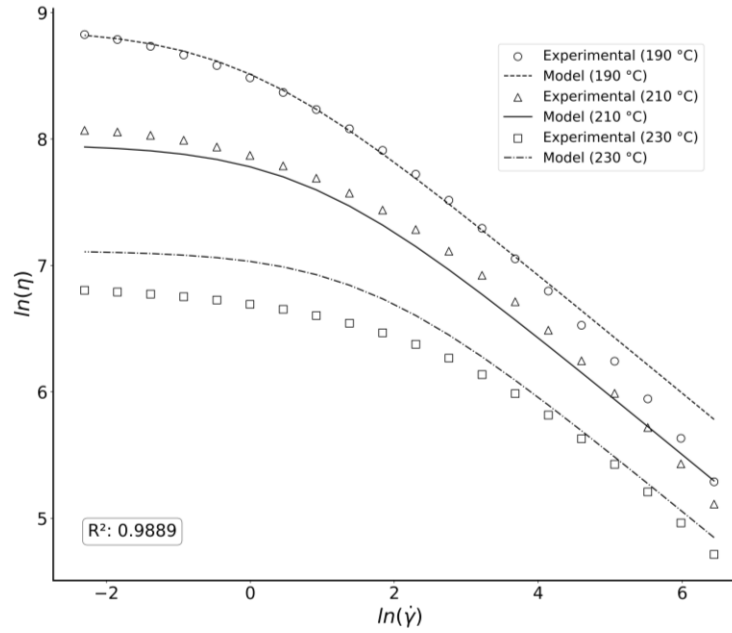


Figure 11. Behavior of polypropylene viscosity in response to shear.

Table 9. Values of fitted parameters and constants.

Symbol	Value	Reference or Method
$A$	2859.2086 Pa s	Fitted parameter
$A_0$	40.31 $\frac{kg}{s}$	Fitted parameter
$B$	0.4623 s	Fitted parameter
$C$	0.4691	Fitted parameter
$C_{pm}$	2500 $\frac{J}{kg K}$	Estrada & Janna (2022)
$C_{ps}$	1800 $\frac{J}{kg K}$	Estrada & Janna (2022)
$E_{asm}$	25204 $\frac{J}{mol}$	Drabek et al. (2018)
$E_{a\eta}$	84993.8738 $\frac{J}{mol}$	Fitted parameter
$K_D$	$4.89 \times 10^{-10}$	Fitted parameter
$p_{amb}$	85115 pa	Fitted parameter
$R_g$	8.314 $\frac{J}{mol K}$	Constant
$T_{melting}$	164.87 °C	ASTM (2021)

$T_{ref}$	210 °C	Fitted parameter
$U_m$	410 $\frac{W}{m^2K}$	Fitted parameter
$U_s$	320 $\frac{W}{m^2K}$	Fitted parameter
$\Delta \hat{h}_{sm}$	109600 $\frac{J}{kg}$	ASTM (2021)
$\rho_s$	906 $\frac{kg}{m^3}$	ISO (2019)
$\rho_m$	700 $\frac{kg}{m^3}$	Estrada & Janna (2022)

### 3.8 Degree of Freedom Analysis

A degree of freedom (DoF) count is performed to verify that the developed model is solvable. As shown in Table 6, the variables  $r$  and  $h$  have a global equation applicable to the entire channel screw, so they should only be counted once in the tally. The same applies to the parameters  $\omega$ ,  $C_{p_s}$ ,  $C_{p_m}$ ,  $\rho_s$ ,  $\rho_m$ ,  $\rho_s$ ,  $A_c$ ,  $\eta$ , and  $\dot{\gamma}_s'''$ . The model comprises 41 unknowns, distributed across 22 variables, 8 structural parameters, and 11 functional parameters. The model includes 22 equations from its basic structure, and Section 3.7 provides 11 equations for the functional parameters. The 8 remaining structural parameters are obtained from Table 9 and experimental data. This yields a degree of freedom count of  $\text{DoF} = 41 - 41 = 0$ , verifying that the mathematical structure of the model is solvable.

### 3.9 Initial and boundary conditions

The following section presents the initial and boundary conditions that describe the evolution of the material (PP) along the entire single-screw extruder. These conditions are formulated to capture the changes that allow the PP to remain in or transition between different zones within the extruder, accounting for internal transitions as well as the physical constraints imposed at the inlet and outlet of the system. It is assumed that the material enters the process under ambient temperature and pressure conditions. Equation (57) presents the function for the extrusion process ( $f_{ext}$ ) along with its domain and constraints that govern the system.

$$f_{ext} = \begin{cases} \text{Domain: } t \in [0, t_f], \quad z \in [0, L] = [0, L_c] \cup [L_c, L] \\ \left\{ \begin{array}{ll} \text{solids conveying (PDE): } z \in [0, z_I(t)], & \text{if } T_s(t, z) < T_{melt} \\ \text{melting (PDE): } z \in [z_I(t), z_{II}(t)], & \text{if } T_s(t, z) \geq T_{melt} \wedge A_{c_s}(t, z) \geq \epsilon(z) \\ \text{melt conveying (PDE): } z \in [z_{II}(t), L_c] & \text{if } A_{c_s}(t, z) < \epsilon(z) \\ \text{melt flow in the die (ODE): } z \in [L_c, L] \end{array} \right. \end{cases} \quad (57)$$

Where  $L_D$  is the length of the die,  $t_f$  is the final simulation time, and  $z_I(t)$  and  $z_{II}(t)$  represent the lengths of the solid transport and melting zones, respectively. Since  $A_{c_s}$  appears in the denominator of some model equations, there is a risk of division by zero. To prevent this issue, a condition is established as shown in Equation (58), using a fraction of the total cross-sectional area of the channel ( $\epsilon(z)$ ).

$$0 < \alpha \leq 0.01: \{\epsilon(z) = \alpha \times A_c(z)\} \quad (58)$$

The experimental data were taken when the polymer was molten, and the screw was not moving ( $\omega = 0$ ). Therefore, it is necessary to replicate these initial conditions before obtaining the data to validate the model.

Initial conditions with  $\omega(t) = 0 \quad \forall t \in [0, t_{f_1}]$

$$\begin{cases} A_{c_s}(z, 0) = A_c(z), \\ A_{c_m}(z, 0) \approx 0, \\ T_s(z, 0) = T_{amb}, \\ T_m(z, 0) = T_{melting}, \\ p(z, 0) = p_{amb} \end{cases} \quad (59)$$

Initial conditions with  $\omega(0) = 0 \wedge \omega(t) > 0 \quad \forall t \in (0, t_{f_2}]$

$$\begin{cases} A_{c_s}(z, 0) = A_{c_s}(z, t_{f_1}) \\ A_{c_m}(z, 0) = A_{c_m}(z, t_{f_1}), \\ T_s(z, 0) = T_s(z, t_{f_1}), \\ T_m(z, 0) = T_m(z, t_{f_1}), \\ p(z, 0) = p(z, t_{f_1}) \end{cases} \quad (60)$$

Where  $t_{f_1}$  and  $t_{f_2}$  are the final simulation times.

Boundary conditions with  $z = 0 \quad \forall t \in [0, t_f]$

$$\begin{cases} A_{c_s}(0, t) = A_c(0), \\ A_{c_m}(0, t) \approx 0, \\ T_s(0, t) = T_{amb}, \\ T_m(0, t) = T_{melting}, \\ p(0, t) = p_{amb} \end{cases} \quad (61)$$

Moving boundary conditions between the solid transport zone (PS<sub>I</sub>) and the melting zone (PS<sub>II</sub>):

$$0 \leq z < z_I(t): \begin{cases} T_s(z, t) < T_{melt} \\ \frac{\partial p}{\partial z} = 0 \end{cases} \quad (62)$$

Moving boundary conditions between the melting zone (PS<sub>II</sub>) and the melt conveying zone (PS<sub>V</sub>):

$$z_I(t) \leq z < z_{II}(t): \begin{cases} T_s(z, t) \geq T_{melt}, \\ A_{c_s}(z, t) > \epsilon(z) \end{cases} \quad (63)$$

Boundary condition between melt conveying zone (PS<sub>V</sub>) and melt flow in the die (PS<sub>VI</sub>):

$$z_{II}(t) \leq z \leq L_c: \begin{cases} T_s(z_{II}(t), t) = T_m(t, z_{II}(t)) = T_{melt}, \\ p(L_c, t) = p(L, t) + \frac{\dot{m}_m(t, L_c)\eta(t, L_c)}{\rho_m K_D} \end{cases}$$

Boundary condition in melt flow in the die (PS<sub>VI</sub>):

$$\{p(L, t) = p_{amb} \quad (64)$$

### 3.10 Computational Model Construction and Validation

The solution of the PDE system was carried out using the Method of Lines (MOL), which allows transforming PDE systems into ODE systems with respect to time by discretizing the spatial partial derivatives. This enables the use of an initial value problem (IVP) solver to solve the resulting ODE system (Shakeri & Dehghan, 2008). Finite difference discretization was applied using an upwind scheme in space, converting the equations with accumulation terms into ODEs, while the equations for computing the pressure profile were converted into algebraic equations. As a result, the system became a set of differential-algebraic equations (DAE). The International System of Units (SI) was used for the development and simulation of the model; however, the variables  $\omega$ ,  $p$ ,  $T$  and were plotted in *rpm*, *bar*, and  $^{\circ}C$ , respectively, as these units are commonly used in the literature.

The simulation of the single-screw plastic extruder was carried out using the Python programming language, version 3.13.0. To solve the DAE system, the `solve_ivp` function from the `scipy.integrate` module (version 1.14.1) was used, applying the "Radau" method — an implicit Runge-Kutta method of order 5 — suitable for stiff systems. The algebraic equations were solved using `fsolve` from the `scipy.optimize` module (version 1.14.1) (Virtanen et al., 2020). The set of equations was solved simultaneously. Figure 12 shows the algorithm used to solve the extrusion process model defined in Equation (57).

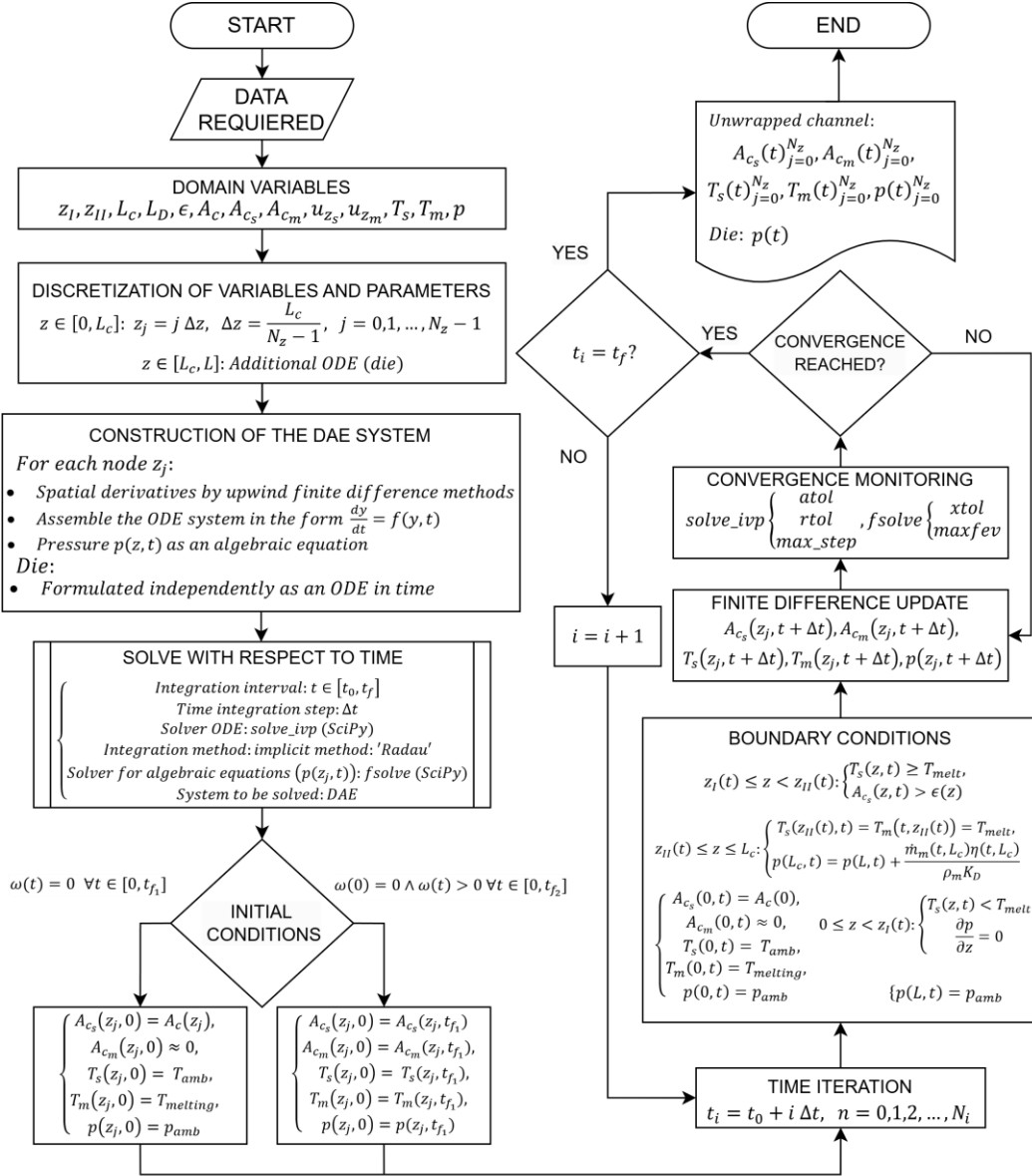


Figure 12. Pseudocode of the algorithm for the numerical solution of the extrusion process model.

To validate the simulation results of the extrusion process in a single-screw extruder, controlled runs were carried out. The data collection was conducted in two stages for a die restriction of  $R_{Die} = 4.46$  turns. First, the extruder was operated at 40 rpm and then stopped for approximately 2 to 3 minutes, until no noticeable changes were observed on the machine's control panel readings. Subsequently, the screw rotational speed ( $\omega$ ) was increased from 0 to 40 rpm within the first 10 seconds and maintained at that value until reaching 230 seconds, as shown in Figure 13. This procedure was repeated three times on different days to verify the reproducibility of the dynamic behavior and to minimize operational fluctuations and measurement errors. All measurements were recorded at a

sampling frequency of one second, allowing the capture of the transition from steady-state to dynamic conditions in the process.

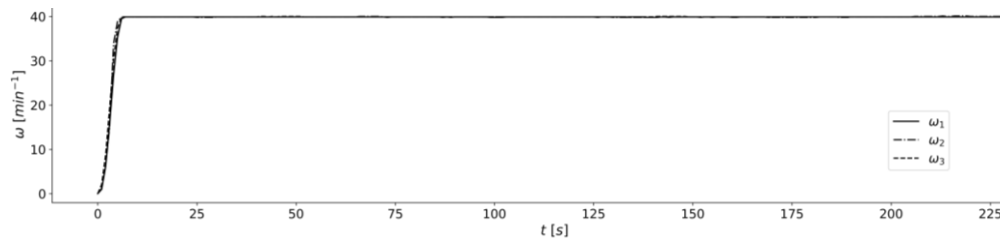


Figure 13. Experimental data from three independent runs at a fixed die restriction of  $R_{Die} = 4.46$  turns, showing the variation of the screw rotational speed ( $\omega$ ) from 0 to 40 rpm, held constant for 230 s; data were collected at 1 Hz.

The melting profile was validated by extracting the screw after one of the runs. In addition, the results were verified using the model proposed by Tadmor et al. (1974), as shown in Figure 20. The pressure profile was obtained by measuring the four points shown in Table 3, in order to capture information from the feeding, melting, melt transport, and melt flow in the die zones. Additionally, boundary conditions were included in the dataset by setting ambient pressure at the inlet ( $p(0)$ ) and outlet ( $p(L)$ ), as shown in Figure 14 for the three runs.

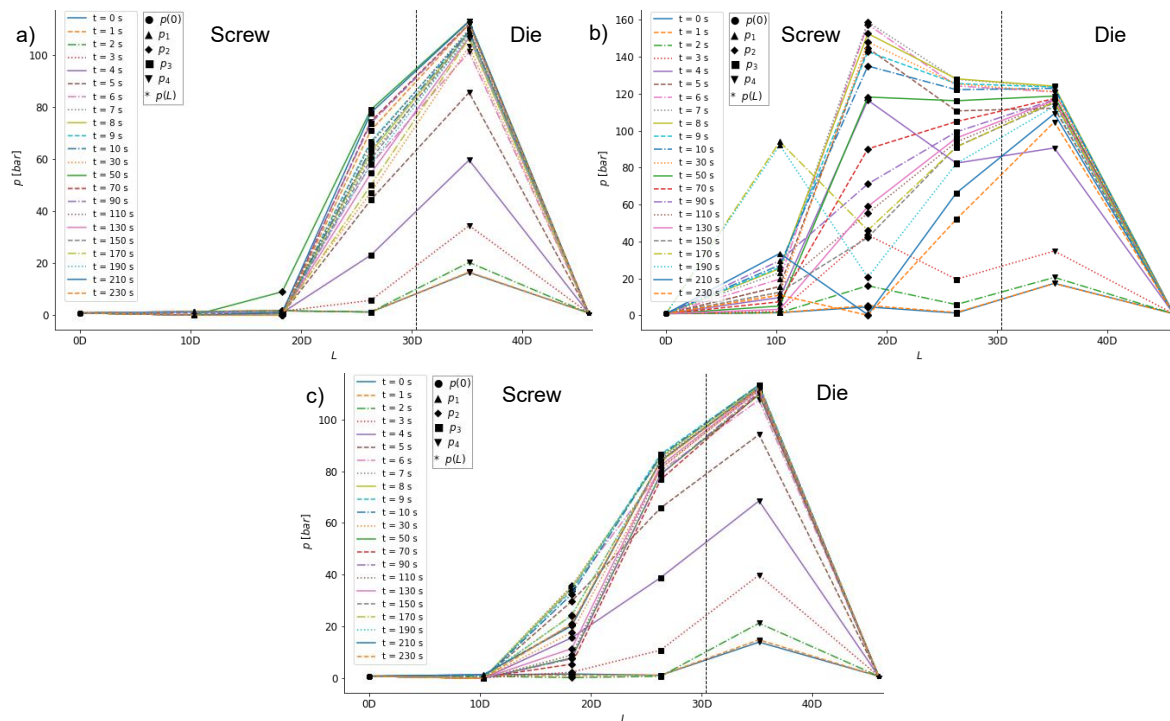


Figure 14. Experimental pressure-profile data along the channel of a single-screw extruder at a fixed die restriction of  $R_{Die} = 4.46$  turns. Pressures were measured at  $p_1$  ( $10.3 D$ ),  $p_2$  ( $18.3 D$ ),  $p_3$  ( $26.5 D$ ), and  $p_4$  ( $35.2 D$ ). The screw rotational speed ( $\omega$ ) was ramped from 0 to 40 rpm and then held at 40 rpm for a total of 230 s, with data collected at 1 Hz. a) first run, b) second run, and c) third run. Atmospheric pressure was imposed as the boundary condition at both the inlet ( $p(0D)$ ) and at the outlet ( $p(L)$ ).

The melt temperature ( $T_m$ ) was measured at the screw outlet using a Thermocomb sensor (thermocouple array) located at  $L = 32.5D$ . The results for the three runs are shown in Figure 15.

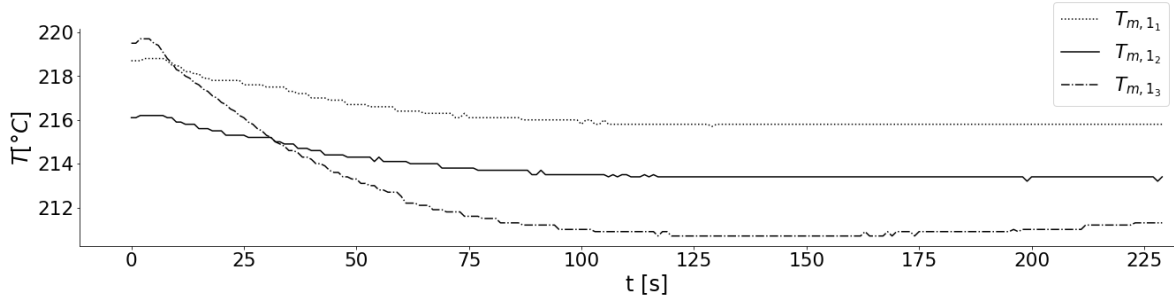


Figure 15. Experimental melt temperature data obtained from three repetitions of the extrusion process in a single-screw extruder each collected over 230 s at a sampling rate of 1 Hz.

To evaluate the accuracy of the model, the Mean Absolute Error (MAE) metric was considered, as given by Equation (65):

$$MAE = \left| \frac{1}{n} \sum_{i=1}^n (X_i - \hat{X}_i) \right| \quad (65)$$

where  $n$  is the number of data points,  $\hat{X}_i$  is the predicted output, and  $X_i$  are the measured data values.

### 3.11 Model Solution and Result Analysis

The descriptive analysis of the experimental data is presented in Table 10. A marked variability in the pressure profile is observed. For  $p_2$ , the mean values ( $\bar{x}$ ) range from 1.0 to 32.6 bar, with standard deviations ( $\sigma$ ) between 1.8 and 22.0 bar, and maximum values ranging from 9.0 to 79.5 bar. For  $p_3$ ,  $\bar{x}$  ranges from 63.4 to 94.6 bar, with  $\sigma$  between 10.9 and 21.1 bar, and maximum values from 80.8 to 128.1 bar. These results indicate that these are the most unstable or transitional zones, since both sensors are located in the melting zone. In contrast,  $p_1$  remains within the  $\bar{x}$  values of 0.3–0.4 bar, with minimum values of 0 bar and maximum values of 1.4 bar, reflecting noise inherent to the measurement. This is expected, as this sensor is located in the solid transport zone, and the oscillation may also be due to the presence of the delay zone at the end of this section, where the first traces of molten material appear (Kacir & Tadmor, 1972). For  $p_4$  values range from 107.7 to 114.0 bar, with  $\sigma$  between 12.1 and 12.9 bar, indicating stabilization of the melt pressure in the die. Regarding the melt temperature ( $T_m(32.5D)$ ),  $\bar{x}$  ranges from 212.3 to 216.3 °C, with relatively low standard deviations (0.8–2.4 °C) and maximum values ranging from 216.2 to 219.7 °C, indicating a relatively narrow interval for the evaluated operating conditions.

Table 10. Descriptive statistics of the experimental data for the pressure profile and melt temperature.

Variable	$p_{11}$	$p_{12}$	$p_{13}$	$p_{21}$	$p_{22}$	$p_{23}$	$p_{31}$	$p_{32}$	$p_{33}$	$p_{41}$	$p_{42}$	$p_{43}$	$T_{m1}$	$T_{m2}$	$T_{m3}$
$\bar{x}$	0.3	0.4	0.4	1.0	32.6	16.1	63.4	94.6	79.8	107.7	114.0	109.7	213.9	216.3	212.3
$\sigma$	0.5	0.5	0.6	1.8	22.0	7.9	13.6	21.1	10.9	12.4	12.9	12.1	0.8	0.8	2.4
min	0.0	0.0	0.0	0.0	0.0	0.3	1.2	1.2	0.8	16.4	17.2	14.0	213.2	215.7	210.7
$Q_1$	0.0	0.0	0.0	0.0	20.7	9.0	55.3	89.4	79.3	107.1	114.93	110.4	213.4	215.8	210.9
$Q_2$	0.0	0.0	0.0	0.2	28.9	18.3	62.5	95.6	81.2	109.2	116.2	111.9	213.4	215.8	211.0
$Q_3$	0.0	0.7	0.8	1.6	49.3	21.8	74.3	108.3	83.5	112.2	117.7	112.5	214.1	216.6	212.7
max	1.4	1.4	1.4	9.0	79.5	35.8	80.8	128.1	86.5	113.2	124.1	13.3	216.2	218.8	219.7

Subscripts 1, 2, and 3 correspond to each repetition of the experiment.

The simulations were carried out based on the unwrapped screw channel, but the results were scaled to be presented in terms of the actual length of the extruder. By maintaining  $\omega = 0 \forall t \in [0,130]$ , the system remains at rest, allowing the variables to evolve toward a quasi-steady state along the entire unwrapped screw channel.  $A_{c_s}$  gradually decreases due to the melting of the solid bed (PP), which in this case is driven primarily by heat conduction from the barrel walls, and the melt pool begins to upstream, in agreement with Tadmor & Gogos (2013), despite the absence of screw rotation, leading to the formation of  $A_{c_m}$ . With respect to  $T_s$  and  $T_m$ , both show uniform behavior in the final regime, as the polymer is not subject to convective transport or viscous dissipation effects. The pressure exhibited a small noise oscillating around  $p_{atm}$ , reflecting the absence of pressure gradients caused by screw rotation. Therefore,  $p_{atm}$  was used as the initial condition for the entire pressure profile  $p$ . The steady-state variable profiles thus serve as the initial conditions for the case where  $\omega(t) > 0$  with  $t > 0$ , ensuring that the simulation starts from a physically realistic state, which helps reduce numerical transients during the early stages when  $\omega$  becomes effective.

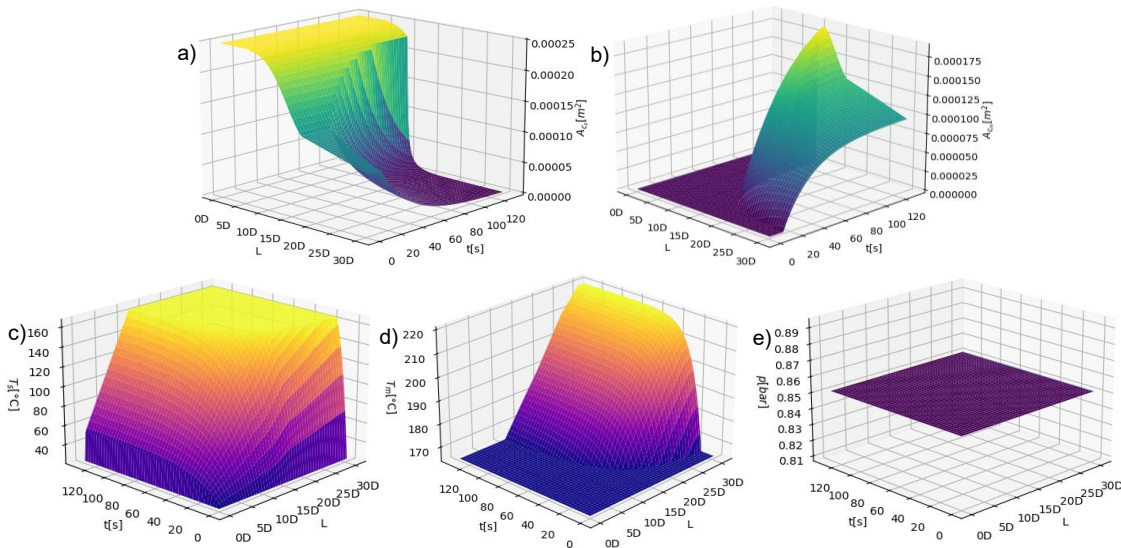


Figure 16. Initial conditions when  $\omega = 0$  for the simulation are applied to a) solid flow area ( $A_{c_s}$ ), b) melt flow area ( $A_{c_m}$ ), c) solid temperature ( $T_s$ ), d) melt temperature ( $T_m$ ), and e) pressure ( $p$ ).

When screw rotation begins ( $\omega(0) = 0 \wedge \omega(t) > 0 \forall t \in (0, 230]$ ),  $A_{c_m}$  initially occupies almost the entire channel flow area ( $A_c$ ) at the beginning of the melting zone, as shown in Figure 17, a result of the previously established initial condition. Once the rotational speed reaches 40 rpm (after 10 s),  $A_{c_m}$  begins to decrease downstream, reflecting the transport effect exerted by the screw rotation on the molten PP. On the other hand, no significant upstream movement of the melting front is observed, which may be due to the magnitude of  $\omega$  not being high enough to generate backflow capable of dragging the melt upstream (Rauwendaal, 2014; Tadmor & Gogos, 2013). The movement of the melting front was observed when simulating extrusion with the screw in motion starting from a fully solid-filled screw channel. However, this scenario was not included in the present study, as it did not match the experimental data collected. The results obtained were highly accurate despite not accounting for the granular transport physics, such as compaction and density variability, heat generation from particle friction, local melt film formation, directional friction, and other related effects.

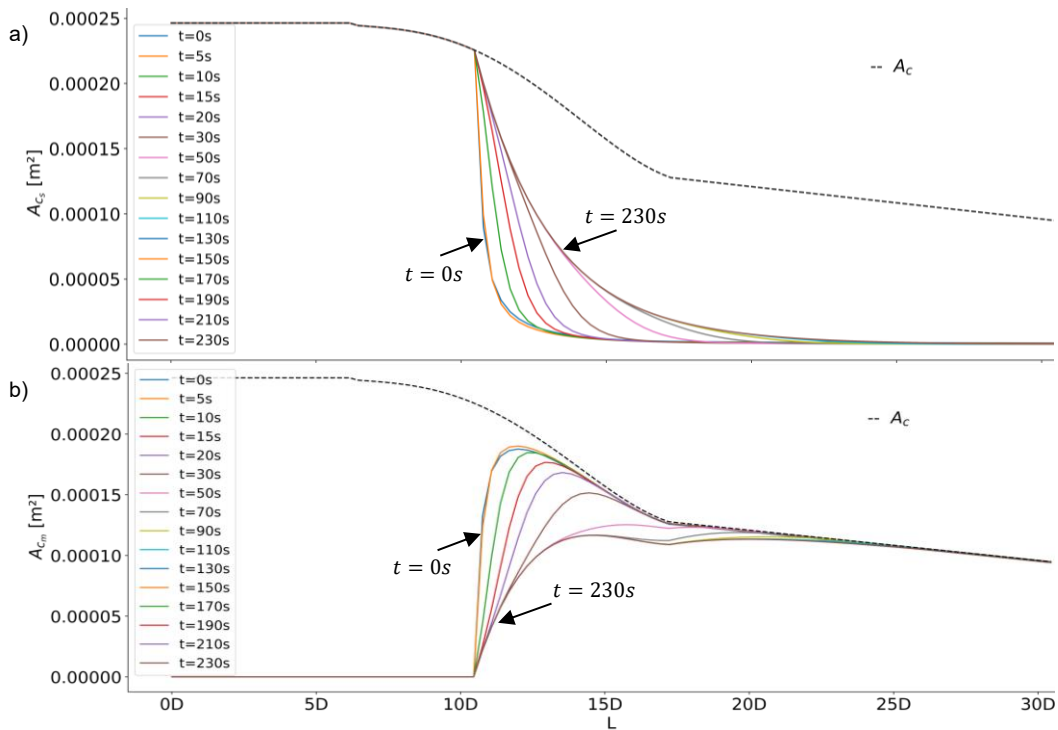


Figure 17. Dynamic profiles obtained from the simulation: of a) solid flow area ( $A_{c_s}$ ) and b) melt flow area ( $A_{c_m}$ ), both as functions of the position  $L$  along the extruder at different times.

The temperature profiles shown in Figure 18 display the progressive increase of  $T_s$  and  $T_m$ . In the initial region (up to approximately 10 D),  $T_s$  starts from the inlet condition ( $T_{amb}$ ) and rises rapidly toward the transition zone, while  $T_m$  is initialized at the melting temperature ( $T_{melt}$ ) and continues increasing downstream until stabilizing around 210–220 °C. Around 25–30 D, thermal homogenization is observed, corresponding to the final zone of the extruder. This behavior is consistent with the findings reported in the literature. At low throughputs, melting temperature profiles are relatively independent of screw geometry,

whereas at high throughputs, the screw design significantly influences melting performance and temperature fields (Kelly et al., 2006). At high screw speeds, the interaction between channel geometry, material properties, and operating conditions becomes critical for determining melt behavior, pressure profiles, and overall extrusion performance—requiring careful consideration in screw design and process optimization (Abdel-Ghany et al., 2015).

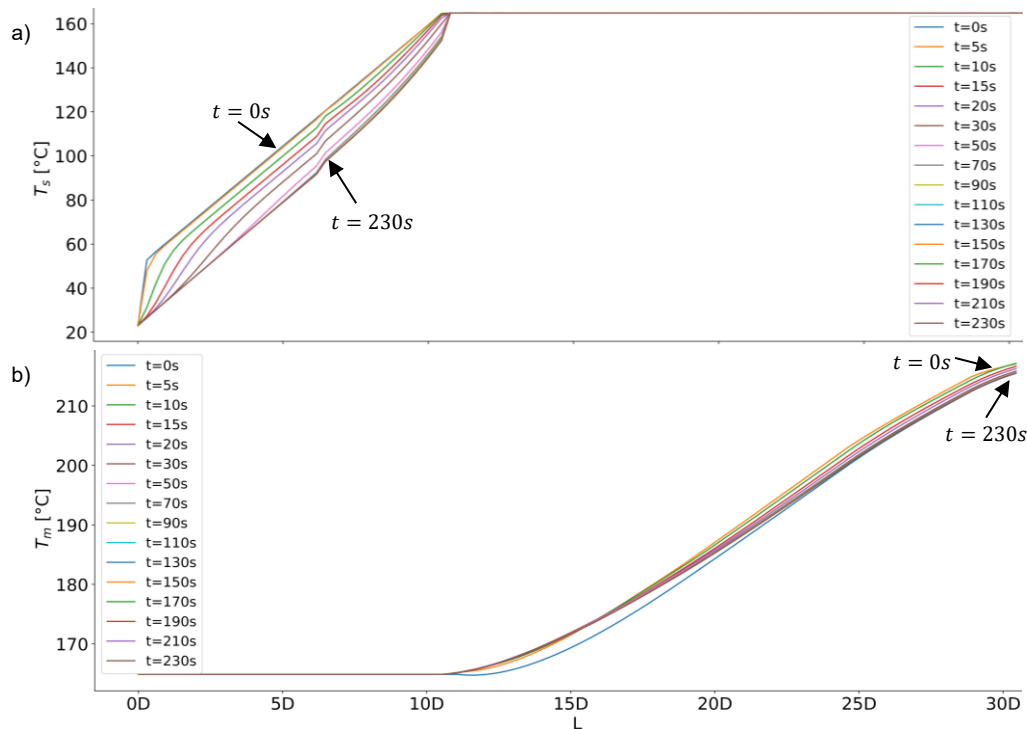


Figure 18. Dynamic profiles obtained from the simulation: a) solid temperature ( $T_s$ ) and b) melt temperature ( $T_m$ ), both as functions of the position  $L$  along the extruder at different times.

The dynamic pressure profiles are shown in Figure 19, where the pressure exhibits much faster dynamics compared to the other variables. A pressure increase is observed along the screw, reaching maximum values of 120–130 bar at the end of the helical geometry (30.4  $D$ ), where the die begins. This behavior has also been reported in previous studies (Abeykoon, Li, Martin, et al., 2011; Costin et al., 1982; Jiang et al., 2012; Nelson et al., 1986; Onwulata et al., 1992). As mentioned earlier, the screw section is governed by a system of equations that depends on both time ( $t$ ) and space ( $z$ ), while the die is modeled as an ODE system (time-dependent only). Therefore, the pressure profile obtained along the screw was connected at the screw–die boundary to the outlet of the die to ensure continuity in the overall pressure profile.

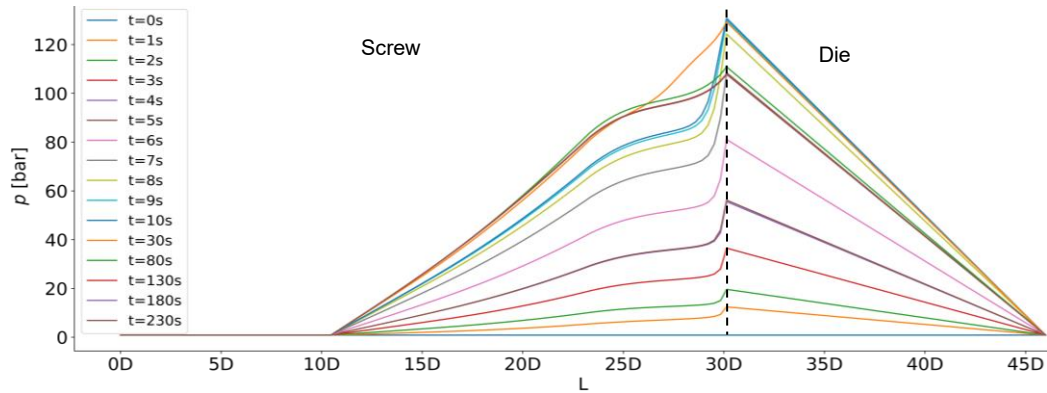


Figure 19. Dynamic profile obtained from the simulation of the pressure ( $p$ ) along the extruder, expressed as a function of the position ( $L$ ) at different time instants.

To validate the model, the plastification profile obtained under steady-state conditions was compared with the Tadmor et al. (1974) model and the actual screw observation (extracted after the experimental runs). As shown in Figure 20, there is a remarkable agreement in both the location and shape of the solid–melt interface. Both approaches indicate that the transition between the solid material and the molten zone begins near 10 D, with a slight displacement of less than 1 D compared to the melting point observed on the actual screw. This small discrepancy between the models may be attributed to the geometric simplifications assumed in the Tadmor model and the nonlinear nature of thermal and rheological effects in practice. Starting from values close to 17.5 D, it can be observed that both models exhibit the same accuracy in predicting the values of  $A_{c_s}$ . Nevertheless, the overall agreement between the curves suggests that both the DAE-based approach and Tadmor’s theoretical formulation accurately describe the onset and progression of the melting front.

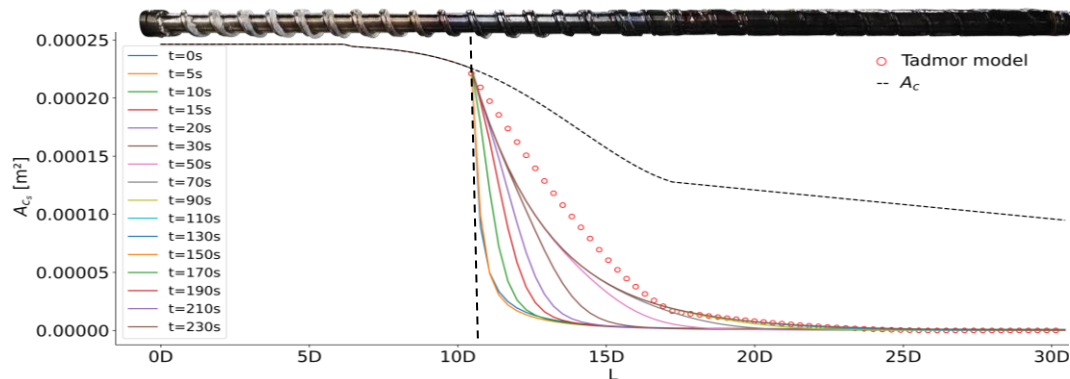


Figure 20. Model validation for the solid flow area ( $A_{c_s}$ ) was performed by comparing the results with the Tadmor model and with a screw that was extracted from the extruder after the data collection was completed.

The model results for pressure demonstrate a good approximation as shown in Figure 21, falling within the standard deviation band relative to the experimental pressure data for  $p_1$ ,  $p_2$ , and  $p_3$ , which are located in the unwrapped screw channel zone. Para  $p_4$ , which is

located in the die region, the model does not explicitly calculate this pressure. However, based on the experimental data, this pressure is expected to lie between the values of  $p_3$  and  $p_4$ . As shown in Figure 21 d), the modeled pressure ( $p_{3-4} = p(L_c)$ ) indeed falls between those values. This behavior is consistent with the interpretation that most of the pressure gradient is concentrated within the screw zone, followed by an additional drop as the flow passes through the die, which acts as a restriction with its own flow characteristics (Burbidge & Bridgwater, 1995; Pachner et al., 2017). Additionally, a transient overshoot is observed during the initial seconds, which may also be attributed to the same condition previously described. This behavior can also be seen in the experimental data. Since the model presented here focuses on the primary simulation of the extruder and not on the detailed behavior of the outlet region, the discrepancy observed in  $p_{3-4}$  is considered reasonable.

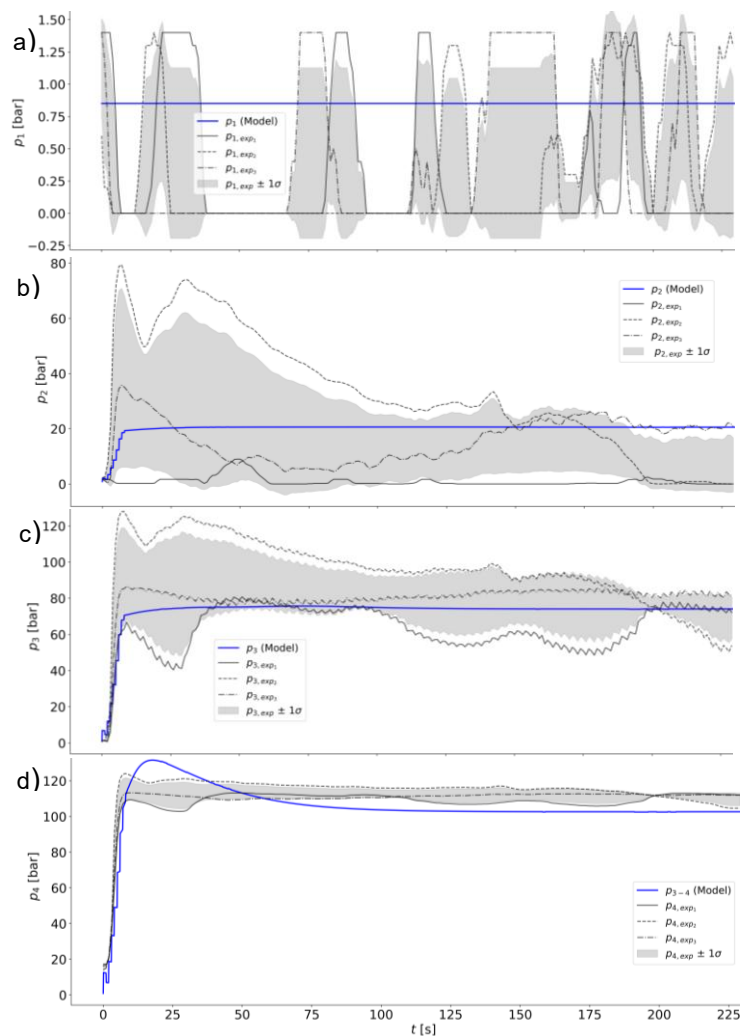


Figure 21. Comparison between the model prediction for the pressure profile and the experimental data corresponding to three repetitions. The gray band represents the standard deviation relative to the experimental mean.

The comparison between the model prediction of  $T_m$  and the experimental data is shown in Figure 22. The validation data correspond to the temperature measured at the screw outlet (30.4 D). A good prediction is observed, with the simulated  $T_m$  values lying very close to the standard deviation band ( $\sigma$ ). During the first 25 s, a transient overshoot is noted, likely caused by the transition from  $\omega = 0$  rpm to  $\omega = 40$  rpm. Although this overshoot is more pronounced in the simulation, it is also visible—albeit to a lesser extent—in the experimental data. A steady-state regime is reached around 70 seconds. Differences in the prediction may arise from the position of the thermocomb sensor, which is located slightly more than one diameter downstream of the model's prediction limit, as well as from process fluctuations not captured in the model formulation (e.g., subtle changes in the thermal conductivity of the polymer or variations in internal convection). Nevertheless, the degree of overlap between the model prediction and the experimental data confirms the robustness of the numerical approximation.

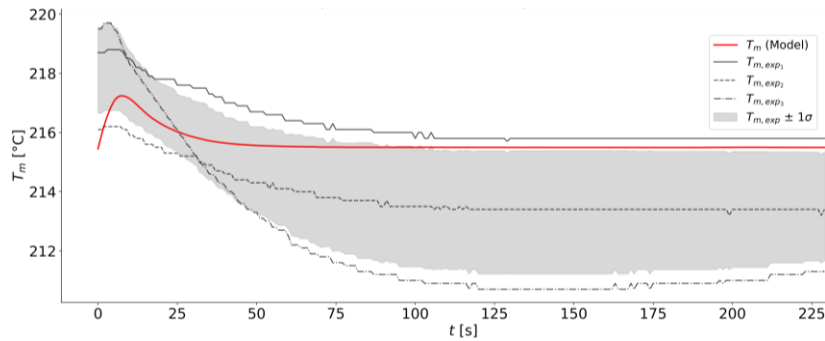


Figure 22. Model validation for the melt temperature was carried out by comparing the simulation results with experimental measurements obtained using a Thermocomb device positioned at 32.6 D along the extruder. The data were recorded at one-second intervals.

The MAE metric was used to evaluate the model's performance, and the results are presented in Table 11. For the prediction of  $A_{c_s}$ , a value of  $7.45 \times 10^{-6} \text{ m}^2$  was obtained, which is relatively small, indicating that the model is capable of accurately predicting the melting profile. In contrast, the predictions for  $p_2$  and  $p_3$ , yielded errors of 8.96 bar and 6.11 bar, respectively. These higher errors may be attributed to the variability observed in the experimental data due to melting-related phenomena, as previously discussed. Despite this, the prediction for  $p_{3-4}$  shows a trend consistent with the value reported by  $p_4$ . For  $p_1$ , an error of 0.51 bar was obtained, which is partly due to the pressure remaining near atmospheric levels—making even minimal fluctuations susceptible to noise inherent in the measurement device. Nevertheless, the model is able to capture this variable effectively. Regarding  $T_m$ , an MAE of 1.66 °C was obtained, demonstrating that the model successfully predicts this variable while preserving its temporal trends.

Table 11. Mean Absolute Error (MAE) values of the predictions made by the model.

Variable	$A_{c_s}[\text{m}^2]$	$p_1[\text{bar}]$	$p_2[\text{bar}]$	$p_3[\text{bar}]$	$T_m[^\circ\text{C}]$
MAE	$7.45 \times 10^{-6}$	0.51	8.96	6.11	1.66

## 3.12 Conclusions

The developed model demonstrated a high capability for estimating process variables in the dynamic state of single-screw extrusion, despite treating the solid as a fluid in the solid transport zone. The results showed that the mathematical formulation—based on mass, momentum, and energy balances, along with the inclusion of polymer rheology and assumptions that allow simplifications for solving the model—successfully captures the key physical mechanisms of extrusion (heat transfer, viscous dissipation, and compression), thus filling a gap in the literature by providing a 1D model capable of performing these predictions dynamically. This led to low MAE values, highlighting the accuracy and usefulness of the implemented modeling approach.

The robustness demonstrated in predicting boundary conditions and the evolution of phenomena involved in the single-screw extrusion process positions the model as a promising tool for the design and optimization of extruders. Its ability to accurately reproduce process start-up and predict steady-state regimes confirms its potential application in screw configuration design, control strategy development, and sensitivity analysis of key extrusion parameters. Although the model still has areas for improvement, it shows significant potential for validation and simulation purposes.

## 4. Artificial Neural Network Model

### 4.1 Model Objective

The developed model seeks to predict the pressure profile along a single-screw extruder using a Feedforward Artificial Neural Network (FANN). The input variables considered were  $I_{mot}$ ,  $\omega$ ,  $R_{Die}$ , and  $T_m$ . Since direct measurement of  $T_m$  presents difficulties due to its contact with the molten polymer and it is uncommon for this variable to be measured in industrial settings, the model seeks to explore whether it is possible to obtain accurate predictions by excluding this variable, leveraging the implicit relationships that  $T_m$  may have with other inputs. In this way, the model aims to optimize extrusion monitoring and reduce the need for complex temperature sensors without compromising the accuracy of pressure predictions at key points in the extruder.

### 4.2 Dimensionality Reduction

Principal Component Analysis (PCA) is a traditional dimensionality reduction technique that assumes that the observed data are a linear combination of a certain basis. Abdi & Williams (2010) described the development of this multivariate statistical technique. In this analysis, variables were first normalized using the mapminmax method [-1,1], which is given by Equation (66):

$$Y_i = Y_{min} + \frac{(Y_{max} - Y_{min})(X_i - X_{min})}{(X_{max} - X_{min})} \quad (66)$$

where  $Y_i$  are the normalized data,  $X_i$  are the measured data values, and  $X_{min}$  and  $X_{max}$  represent the minimum and maximum values of the measured data, with  $Y_{max}$  and  $Y_{min}$  set to 1 and -1, respectively. PCA was then applied to the input variables of the model, as shown in Figure 23, and revealed that the linear correlation between the variables is weak; dark red indicates a strong correlation between the variable and the principal component, while light blue corresponds to a weak correlation between the variable and the principal component. The analysis shows that  $I_{mot}$  and  $\omega$  have a moderate positive correlation of 0.20, thus indicating that as the motor current demand increases, the rotational screw

speed also increases. Additionally, the  $I_{mot}$  has a negative correlation with both  $T_m$  (-0.13) and  $R_{Die}$  (-0.22), suggesting that an increase in motor current demand may be associated with a slight decrease in these variables.  $\omega$  and  $T_m$  have an inverse relationship with a value of -0.3. In turn, the rotational screw speed ( $\omega$ ) and die restriction ( $R_{Die}$ ) have a very low correlation. Lastly, it is shown that  $T_m$  and  $R_{Die}$  have a negative correlation (-0.26), thus indicating an inverse relationship.

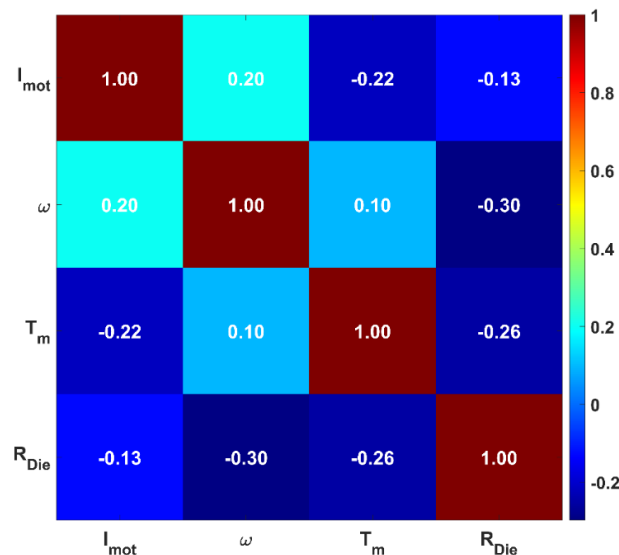


Figure 23. Correlation matrix from PCA.  $I_{mot}$  shows a positive correlation with  $\omega$  (0.20) and negative correlations with  $T_m$  (-0.13) and  $R_{Die}$  (-0.22). Additionally,  $\omega$  and  $T_m$  exhibit an inverse correlation (-0.30), while  $T_m$  and  $R_{Die}$  present a weak negative correlation (-0.26).

The analysis of total explained variance is described by Jolliffe & Cadima (2016) and shows that it is common to use a specific percentage, e.g., 70%, to decide how many principal components (PC) should be retained, although this threshold is subjective. Nevertheless, this percentage remains key to evaluating the quality of graphical representations. While the first components are often emphasized in analysis, the last ones can also be useful, especially in outlier detection or in some image analysis applications. Figure 24 shows that  $I_{mot}$  explains most of the data variability, accounting for 97.1455% of the total variability.  $\omega$  (1.8044%),  $T_m$  (1.0489%), and  $R_{Die}$  (0.0004%) do not significantly contribute to the explained variance. This suggests that motor current demand ( $I_{mot}$ ) has a primary role in the model, while the other variables are secondary.

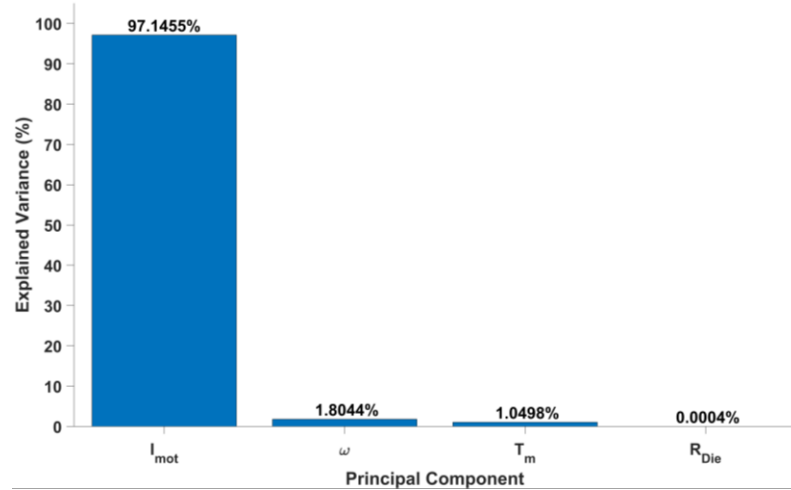


Figure 24. Percentage of variance explained by each principal component. Motor current demand ( $I_{mot}$ ) explains most of the data variability (97.1%), while  $\omega$  (1.8%),  $T_m$  (1.0%), and  $R_{Die}$  (0.0%) contribute minimally to the explained variance.

### 4.3 Feedforward Artificial Neural Networks

Data were randomly divided to ensure that there are no patterns related to the order in which they were combined; thereby reducing the risk of overfitting by guaranteeing that the training and test data were representative. Additionally, a seed was added so that the data generation is consistent in each trial. The dataset was split with 70 % allocated for training, 15% for validation, and the remaining 15 % for testing. Five configurations of FANNs were tested. Furthermore, the extrusion process has been modeled based on a 1D hyperbolic PDE analysis of mass transport (Diagne et al., 2016b, 2016a). When solving PDEs with PINNs, S. Wang et al. (2023) recommend initially using the hyperbolic tangent ( $\tanh$ ) activation function, which is given by Equation (67):

$$\tanh(x) = \frac{e^x - e^{-x}}{e^x + e^{-x}} \quad (67)$$

Its range is  $[-1, 1]$ . The hyperbolic tangent was used as the activation function in this model. The values of the weights ( $W^i$ ) and the biases ( $B^i$ ) were initialized randomly. Mean Squared Error (MSE) and the Coefficient of Determination ( $R^2$ ) were used as metrics to evaluate the accuracy of the model, as shown in Equations (68) and (69) :

$$MSE = \frac{1}{n} \sum_{i=1}^n (X_i - \hat{X}_i)^2 \quad (68)$$

$$R^2 = 1 - \frac{\sum_{i=1}^n (X_i - \hat{X}_i)^2}{\sum_{i=1}^n (X_i - \bar{X}_i)^2} \quad (69)$$

where  $n$  is the number of data points,  $\hat{X}_i$  is the predicted output, and  $\bar{X}_i$  is the mean value of the observed data. The Levenberg-Marquardt backpropagation algorithm was used as optimizer. It is a variant of traditional backpropagation that utilizes an approximation of the Newton method to update the weights of a neural network using the Hessian matrix and gradient (Bilski & Wilamowski, 2017).

Models were trained and validated on a Lenovo Legion 5 Pro laptop with an 11th Gen Intel(R) Core (TM) i7-11800H @ 2.30GHz processor (16 CPUs) and 32 GB of RAM. The programming language MATLAB, version 24.2.0.2712019 (R2024b), was used for the training and validation of the FANNs model. ANNs modeling has been studied to improve their performance, focusing on the data collection process for training, data processing, activation functions, weight initialization, optimizers, and error functions. Additionally, efforts have been made to improve the architecture of ANNs; however, there is no theoretical basis for this, although some methods can be used in specific cases (Benardos & Vosniakos, 2007). In this work, the general method of trial and error was employed.

## 4.4 Results and Discussion

Table 12 presents the architectures tested in the FANNs used to predict the pressure profile along a single-screw extruder, the values obtained for the metrics used to evaluate the accuracy of the model (MSE and  $R^2$ ) for each dataset (training, validation, testing, and overall), the number of neurons per layer ( $NN$ ), as well as the number of epochs ( $E$ ) and the computational time ( $t$ ) required for training each proposed architecture. No learning rate was entered into the model since the 'trainlm' (Levenberg-Marquardt) algorithm in MATLAB adjusts the learning rate directly. It uses an adaptive learning rate ( $\lambda$ ), which increases when an iteration raises the performance function and decreases after each successful step (reduction in the performance function). The default value of  $\lambda$  is 0.001, the decrease factor is 0.1, the increase factor is 10, and the maximum value is  $1 \times 10^{10}$ . The input variables used in the FANNs are  $I_{mot}$ ,  $\omega$ ,  $R_{Die}$  and  $T_m$ . The outputs of the FANNs are the predicted pressure profiles at four points along the extruder ( $p_1, p_2, p_3, p_4$ ) as indicated in Table 3.

Table 12. Results of the Feedforward Artificial Neural Network Architectures.

Inputs	NN			Metrics								E	t
	IL	HL 1	HL 2	MSE				R <sup>2</sup>					
				Train	Val	Test	All	Train	Val	Test	All		
$I_{mot}, \omega, R_{Die}, T_m$	4	10	8	0.0075	0.0078	0.0078	0.0077	0.9894	0.9888	0.9889	0.9892	195	108
$I_{mot}, \omega, R_{Die}, T_m$	4	8	6	0.0092	0.0091	0.0093	0.0092	0.9869	0.9869	0.9868	0.9869	209	41
$I_{mot}, \omega, R_{Die}$	3	10	8	0.0093	0.0097	0.0097	0.0096	0.9867	0.9861	0.9863	0.9866	224	80
$I_{mot}, \omega, R_{Die}$	3	8	6	0.0099	0.0094	0.0099	0.0097	0.9858	0.9864	0.9860	0.9859	509	147
$I_{mot}, \omega$	2	10	8	0.0261	0.0254	0.0255	0.0257	0.9623	0.9631	0.9634	0.9626	234	65

The training results of the different FANNs architectures yielded low MSE values ranging from 0.0075 to 0.0261,  $R^2$  values varied between 0.9623 and 0.9894, thus indicating a high model fitting capability. In the validation and test datasets, MSE values ranged from 0.0078 to 0.0255, and  $R^2$  values were between 0.9631 and 0.9889, demonstrating a strong predictive capacity of the models. Additionally, there is a minimal difference between the MSE values obtained from the training dataset compared to those of the validation and test datasets, which suggest that tested models do not present overfitting. In general, it is observed that  $R^2$  values are consistently high in all cases, indicating that FANNs have been able to adequately model the relationship between input variables and pressure profile in the extruder. Despite variations in the number of neurons in hidden layers ( $HL$ ) 1 and 2, there is not a significant difference in  $E$  and  $t$  among tested architectures; therefore, these factors do not have a substantial impact on model performance.

The specific mechanical energy (SME) is an indicator of the extrusion process and is derived from independent variables such as barrel temperature, rotational screw speed, and die geometry (Fayose & Huan, 2014). In a study on the energy consumption by a single-screw extruder conducted by Abeykoon et al. (2010), they found that the rotational screw speed is the most significant parameter in determining the motor energy demand. As shown in the analysis of the percentage of variance explained in Figure 24,  $I_{mot}$  explains 97.1% of the total data variability. Therefore, the architectures were tested, and greater importance was given to the  $I_{mot}$  variable as an input to the model. The first and second architectures shown in Table 4 consider the four measured variables in the extruder ( $I_{mot}$ ,  $\omega$ ,  $R_{Die}$  and  $T_m$ ) as model inputs. The first FANN achieved the highest performance of all tests. Measurement of  $T_m$  involves direct contact with the melt inside the extruder, unlike the variables  $I_{mot}$ ,  $\omega$ , and  $R_{Die}$ , which are external measurements that do not require direct contact with it. In the third and fourth architectures, the variable  $T_m$  was excluded, and it was observed that omitting this variable only slightly decreased the accuracy of the model; the best results were obtained in the third architecture. In the last two tested architectures, only  $I_{mot}$  and  $\omega$  were used as model inputs, thus showing that excluding  $R_{Die}$  from the model reduced the prediction accuracy, as it plays an important role in controlling the material flow in the die, directly affecting the pressure profile.

The third FANN in Table 12 is of particular interest because it uses only  $I_{mot}$ ,  $\omega$ , and  $R_{Die}$  as input variables, omitting  $T_m$ , which offers a significant advantage by reducing the number of input variables required by the FANN for pressure profile prediction. Additionally,  $T_m$  is not frequently measured in industrial environments. Regarding performance, this architecture shows an  $R^2$  of 0.9867 for the training set, 0.9861 for the validation set, and 0.9863 for the test set, with MSE values ranging from 0.0093 to 0.0097 across all datasets. The number of epochs ( $E$ ) and convergence time ( $t$ ) yielded values of  $E = 224$  and  $t = 80$  s. These indicate high prediction accuracy, even without considering melting temperature ( $T_m$ ) as an input variable. It is possible that the effect of  $T_m$  on the pressure profile is indirectly captured by variables such as  $I_{mot}$ ,  $\omega$  and  $R_{Die}$ , which are related to heat transfer and the rheological behavior of the polymer during the extrusion process. The die restriction ( $R_{Die}$ ) is a material flow control element that directly affects the pressure profile

within the extruder, it determines how the material is transported and heated during the process. It has been found that viscous dissipation caused by shear contributes approximately 80% of the heat needed to melt the polymer (Hyvärinen et al., 2020).  $R_{Die}$  imposes pressure due to the resistance that must be overcome, which increases dissipation and, consequently, material temperature. By including  $R_{Die}$  in the model, the FANN gains indirect information on the behavior of  $T_m$ , as  $T_m$  and the flow respond to the pressure demand at the die, adapting internal flow and temperature conditions to meet this restriction. In this way,  $R_{Die}$  plays an important role in process dynamics, becoming as significant as  $I_{mot}$ , and providing the necessary information for the FANN to make more accurate predictions without explicitly requiring  $T_m$ . This FANN diagram is shown in Figure 25.

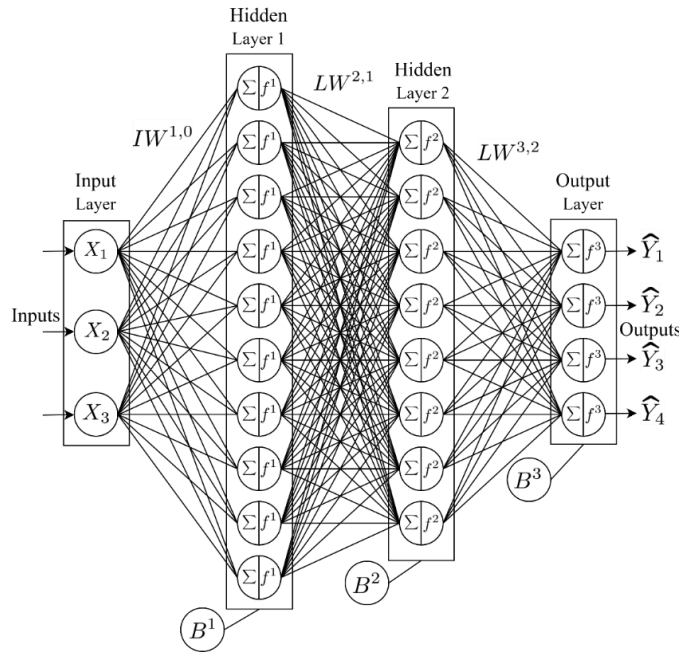


Figure 25. Diagram of a three-hidden-layer artificial neural network used for predicting the pressure profile in a single-screw extruder, with interconnected neurons processing input features through nonlinear activation functions.

The equation that defines this FANN shown in Figure 25 and is obtained as follows:

Hidden layer 1:

$$Net^1 = IW^{1,0} \cdot I + B^1 \quad (70)$$

Activation function of hidden layer 1:

$$A^1 = f^1(Net^1) = f^1(IW^{1,0} \cdot I + B^1) \quad (71)$$

Hidden layer 2:

$$Net^2 = LW^{2,1} \cdot A^1 + B^2 \quad (72)$$

Activation function of hidden layer 2:

$$A^2 = f^2(Net^2) = f^2(LW^{2,1} \cdot A^1 + B^2) \quad (73)$$

Output layer:

$$Net^3 = LW^{3,2} \cdot A^2 + B^3 \quad (74)$$

Activation function of output layer:

$$O = f^3(Net^3) = f^3(LW^{3,2} \cdot A^2 + B^3) \quad (75)$$

where  $I$  is the identity matrix,  $IW^{1,0}$ ,  $LW^{2,1}$  and  $LW^{3,2}$  are the weight matrices from the input layer to the first hidden layer, from the first hidden layer to the second hidden layer, and from the second hidden layer to the output layer, respectively.  $B^1$ ,  $B^2$ , and  $B^3$  are the bias vectors for the first hidden layer, second hidden layer, and output layer, respectively. By substituting  $A^1$  and  $A^2$  into  $O$ , we obtain:

$$O = f^3(LW^{3,2} \cdot f^2(LW^{2,1} \cdot f^1(IW^{1,0} \cdot I + B^1) + B^2) + B^3) \quad (76)$$

Equation (76) represents the general equation of a FANN with three layers. The FANN of interest has inputs  $I_{mot}$ ,  $\omega$ , and  $R_{Die}$ , and its architecture is defined by 3 *Inputs*, 10 neurons in the first hidden layer (*HL*), 8 neurons in the second hidden layer (*HL*), and 4 neurons in the output layer (*OL*). Parameters have the following dimensions:  $IW^{1,0}$ :  $(3 \times 10)$ ,  $LW^{2,1}$ :  $(10 \times 8)$ ,  $LW^{3,2}$ :  $(8 \times 4)$ ,  $B^1$ :  $(10 \times 1)$ ,  $B^2$ :  $(8 \times 1)$  and  $B^3$ :  $(4 \times 1)$ , resulting in a total of 164 parameters, including weights and biases, that need to be adjusted to improve the performance of the network.

Figure 26 presents a scatter plot of the actual pressure and the predictions made by the FANN for the pressure profile ( $p_1, p_2, p_3, p_4$ ). There is lower precision in the prediction of  $p_1$ , which corresponds to the solid transport zone that extends to where the solid plug reaches the melting point. In this zone (delay zone), the melting mechanism has a delay, which is where the first traces of molten material are generated (Kacir & Tadmor, 1972). Therefore, with only a thin film of molten material, there is greater noise in the measurement. This same issue is observed for  $p_2$ , as the sensor is located in the melting zone, but with a greater presence of molten material, the noise decreases.  $p_3$  is positioned at the end of the melting zone, which is why there is very little noise in the measurement, as the polymer is almost entirely molten. The prediction for  $p_4$ , located at the end of the solid transport zone and the beginning of the molten flow zone in the die, is very high. Real data nearly overlaps the predictions made by the FANN completely. In this area, the polymer is fully molten, thus eliminating the noise caused by the presence of solids, leaving

only the inherent measurement noise. It is noteworthy that  $p_4$  (melt pressure) is the measurement of greatest interest in the process as a quality parameter for the product (Abeykoon et al., 2020). Therefore, the model aims to achieve the highest prediction accuracy for this measure.

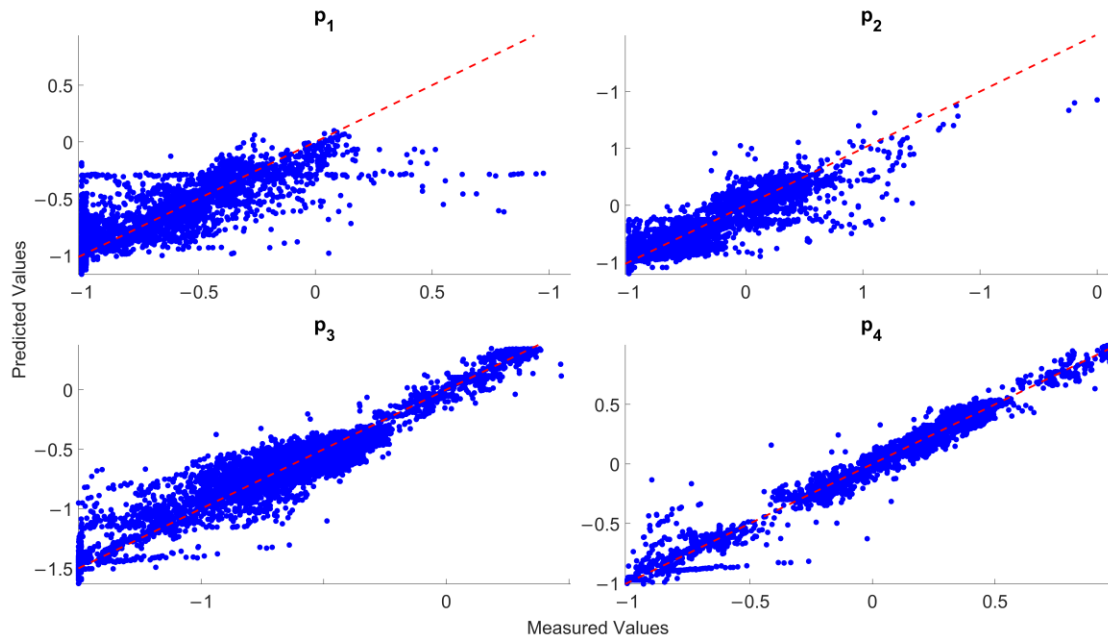


Figure 26. Scatter plot of the pressure profile ( $p_1, p_2, p_3, p_4$ ) with normalized test data ( $R^2 = 0.9863$  and  $MSE = 0.0097$ ).

The accuracy demonstrated by the FANN highlights the potential of these models to predict process variables like the pressure profile in a single-screw plastic extruder. This performance also opens the possibility of real-time implementation within the process control system, as ANNs can function effectively as soft sensors. Such sensors are a cost-effective alternative to expensive physical sensors, can easily complement physical sensors, and can be applied directly while continuously evaluating data during operation (Savytskyi et al., 2020). The implemented FANN showed a high capacity to capture dynamic changes occurring in the process in response to disturbances, thus making them a valuable tool for assessing energy efficiency and optimizing energy consumption.

Traditional machine learning models face limitations with low data availability; various solutions have been proposed to address this, e.g., data augmentation through slight modifications of existing data; embedding domain knowledge into the structure of FANNs using white-box models that integrate physical laws or black-box models, which require extensive data; integration of differential equations to supplement missing data in PINNs as a solution to this challenge (Buchaniec et al., 2021). Feng et al. (2019) demonstrated that deep and narrow neural networks can address problems in material science, where data availability is often limited. They suggest specific training methods, such as pre-

training with a stacked autoencoder in deep neural networks (DNN) using a small dataset. Finally, applying artificial neural network models to new materials, operating conditions and different equipment can reduce prediction accuracy, or make adaptation challenging if there is not enough data reflecting these changes in the process.

## 4.5 Conclusions

In this work, the use of FANNs was proposed to predict the pressure profile in a single-screw plastic extruder, including motor current demand and melt temperature as input variables. Based on the model performance, the potential of ANNs as soft sensors is highlighted, presenting them as an alternative to physical sensors when these fail or need replacement, thus enabling uninterrupted process control and continuous plant operation. Despite limitations, such as the requirement for large datasets, application to different materials, and changes in extruder geometry, ANNs can play a significant role in process optimization and real-time monitoring.

Motor current demand ( $I_{mot}$ ) is an important input variable ( $I$ ) for the ANN model when predicting the pressure profile due to its correlation with polymer transport during the extrusion process. Additionally, as it accounts for most of the variance in the data, including it in the model ensures high prediction accuracy. In addition, it is shown that including  $R_{Die}$  as an input variable in the ANN model increases the accuracy in predicting the pressure profile along the single-screw extruder; since this variable plays a key role in flow dynamics within the die, its absence results in a significant loss of prediction accuracy. It is recommended that this variable continues to be used in future analysis and industrial applications.

## 5. Conclusions and Recommendations

### 5.1 Conclusions

The acquisition of experimental data and the characterization of the extrusion system highlighted the high complexity of single-screw extrusion processes, as evidenced by the detailed measurement of the screw and barrel geometry, as well as the determination of the rheological parameters and melting point of the polypropylene (PP). In addition, a database was created consisting of  $1 \text{ s}^{-1}$  sampling records of screw rotational speed, melt temperature, and pressure at four strategic points. These measurements were obtained under screw speed perturbations (0–160 rpm) and variations in die restriction.

The developed model demonstrated a high capability for estimating process variables in the dynamic state of single-screw extrusion, despite treating the solid as a fluid in the solid transport zone. The results showed that the mathematical formulation—based on mass, momentum, and energy balances, along with the inclusion of polymer rheology and assumptions that allow simplifications for solving the model—successfully captures the key physical mechanisms of extrusion (heat transfer, viscous dissipation, and compression), thus filling a gap in the literature by providing a 1D model capable of performing these predictions dynamically. This led to low MAE values, highlighting the accuracy and usefulness of the implemented modeling approach.

The robustness demonstrated in predicting boundary conditions and the evolution of phenomena involved in the single-screw extrusion process positions the model as a promising tool for the design and optimization of extruders. Its ability to accurately reproduce process start-up and predict steady-state regimes confirms its potential application in screw configuration design, control strategy development, and sensitivity analysis of key extrusion parameters. Although the model still has areas for improvement, it shows significant potential for validation and simulation purposes.

Since pressure is an indicator of final product quality in polymer extrusion processes, predicting the pressure profile in single-screw extruders using Feedforward Artificial Neural Networks (FANN) has great potential for implementation in less-sensor strategies. As demonstrated, it is possible to accurately predict the pressure profile using data that do not directly contact the molten mass, such as rotational screw speed, motor current demand, and die restriction. Implementing this approach as a virtual sensor can be highly beneficial for preventing unscheduled extruder shutdowns in industrial plants, where physical sensors may fail or deteriorate. Ensuring operational continuity translates into economic savings. Therefore, FANN models can effectively enable continuous monitoring of the extrusion process and the quality of the final product.

Motor current demand ( $I_{mot}$ ) is an important input variable ( $I$ ) for the ANN model when predicting the pressure profile due to its correlation with polymer transport during the extrusion process. Additionally, as it accounts for most of the variance in the data, including it in the model ensures high prediction accuracy. In addition, it is shown that including  $R_{Die}$  as an input variable in the ANN model increases the accuracy in predicting the pressure profile along the single-screw extruder; since this variable plays a key role in flow dynamics within the die, its absence results in a significant loss of prediction accuracy. It is recommended that this variable continues to be used in future analysis and industrial applications.

## 5.2 Recommendations

It is recommended to further refine the experimental calibration of the rheological parameters, as well as the specific physical and thermal properties of the polymer used in the simulation, in order to improve the overall accuracy of the model. Additionally, it is suggested to review and enhance the mathematical formulation in the solid transport zone, which is currently simplified, by incorporating additional effects such as compaction, solid friction, and wall slip, with the aim of increasing the model's precision.

It is also advised to evaluate the differential equation model under various operating conditions, including changes in die restriction and dynamic variations in screw rotational speed, to strengthen the model's robustness and predictive capability across a wide range of industrial scenarios.

Test the artificial neural network (ANN) model by performing both interpolation and extrapolation of the predictions to evaluate its performance under these conditions. Additionally, assess its robustness in the presence of disturbances, verifying whether the predictions remain stable. It is also recommended to explore other AI-based models for predicting the pressure profile, in order to compare their performance and potentially improve prediction accuracy and generalization.

Explore hybrid strategies by integrating the rigorous physics-based model of differential equations—which has demonstrated high accuracy in predicting the polymer

temperature—with artificial intelligence models such as artificial neural networks (ANNs). As shown in Section 4, melt temperature measurement is either uncommon or difficult to obtain in these processes, yet this variable significantly improves the accuracy of ANN-based models for predicting the pressure profile in single-screw extruders. Therefore, using the temperature predicted by the differential equation model as an input to the ANN would be highly valuable.

Additionally, it is proposed to evaluate the use of Physics-Informed Neural Networks (PINNs) to directly estimate the mass flow rate, and to integrate this output with the ANN that predicts the pressure profile. The goal is to develop a robust less-sensor control strategy capable of monitoring and regulating the extrusion process in real time, even in scenarios where physical sensors fail or are not available due to damage or the absence of installation.

## **A. Appendix: Development of a Dynamic Model for a Single-Screw Extruder**

## General Equations for Microscopic Balances

### Continuity Equation:

$$\text{Accumulation Term} + \text{Convective Term} = 0 \quad (77)$$

$$\frac{\partial \rho}{\partial t} + \frac{\partial(\rho u_x)}{\partial x} + \frac{\partial(\rho u_y)}{\partial y} + \frac{\partial(\rho u_z)}{\partial z} = 0 \quad (78)$$

### Mass Balance Per Species:

$$\text{Accumulation Term} + \text{Convective Term} = \text{Source Term} \quad (79)$$

$$\frac{\partial \rho_k}{\partial t} + \frac{\partial(\rho_k u_x)}{\partial x} + \frac{\partial(\rho_k u_y)}{\partial y} + \frac{\partial(\rho_k u_z)}{\partial z} = \dot{r}_k''' \quad (80)$$

### Momentum Balance:

$$\text{Accumulation Term} + \text{Convective Term} = - \text{Molecular Transport Term} - \text{External Forces Transport Term} + \text{Source Term} \quad (81)$$

$$\begin{aligned} & \begin{bmatrix} \frac{\partial(\rho u_x)}{\partial t} \\ \frac{\partial(\rho u_y)}{\partial t} \\ \frac{\partial(\rho u_z)}{\partial t} \end{bmatrix} + \begin{bmatrix} \frac{\partial(\rho u_x u_x)}{\partial x} & \frac{\partial(\rho u_x u_y)}{\partial y} & \frac{\partial(\rho u_x u_z)}{\partial z} \\ \frac{\partial(\rho u_y u_x)}{\partial x} & \frac{\partial(\rho u_y u_y)}{\partial y} & \frac{\partial(\rho u_y u_z)}{\partial z} \\ \frac{\partial(\rho u_z u_x)}{\partial x} & \frac{\partial(\rho u_z u_y)}{\partial y} & \frac{\partial(\rho u_z u_z)}{\partial z} \end{bmatrix} \\ & = - \begin{bmatrix} \frac{\partial p}{\partial x} \\ \frac{\partial p}{\partial y} \\ \frac{\partial p}{\partial z} \end{bmatrix} + \mu \nabla \cdot \begin{bmatrix} 2 \frac{\partial u_x}{\partial x} & \frac{\partial u_x}{\partial y} + \frac{\partial u_y}{\partial x} & \frac{\partial u_z}{\partial x} + \frac{\partial u_x}{\partial z} \\ \frac{\partial u_x}{\partial y} + \frac{\partial u_y}{\partial x} & 2 \frac{\partial u_y}{\partial y} & \frac{\partial u_z}{\partial y} + \frac{\partial u_y}{\partial z} \\ \frac{\partial u_x}{\partial z} + \frac{\partial u_z}{\partial x} & \frac{\partial u_y}{\partial z} + \frac{\partial u_z}{\partial y} & 2 \frac{\partial u_z}{\partial z} \end{bmatrix} + \rho \begin{bmatrix} \frac{\partial f_x}{\partial x} \\ \frac{\partial f_y}{\partial y} \\ \frac{\partial f_z}{\partial z} \end{bmatrix} + \dot{r}_u''' \end{aligned} \quad (82)$$

### Energy Balance:

$$\text{Accumulation Term} + \text{Convective Term} = - \text{Diffusive Term} + \text{Viscous Dissipation Term} + \text{Source Term} \quad (83)$$

$$\begin{aligned}
& \frac{\partial(\rho C_p T)}{\partial t} + \frac{\partial(u_x \rho C_p T)}{\partial x} + \frac{\partial(u_y \rho C_p T)}{\partial y} + \frac{\partial(u_z \rho C_p T)}{\partial z} \\
& = -\frac{\partial q_x'''}{\partial x} + \frac{\partial q_y'''}{\partial y} + \frac{\partial q_z'''}{\partial z} \\
& + \mu \left( 2 \left[ \left( \frac{\partial u_x}{\partial x} \right)^2 + \left( \frac{\partial u_y}{\partial y} \right)^2 + \left( \frac{\partial u_z}{\partial z} \right)^2 \right] \right. \\
& \left. + \left[ \left( \frac{\partial u_x}{\partial y} + \frac{\partial u_y}{\partial x} \right)^2 + \left( \frac{\partial u_x}{\partial z} + \frac{\partial u_z}{\partial x} \right)^2 + \left( \frac{\partial u_y}{\partial z} + \frac{\partial u_z}{\partial y} \right)^2 \right] \right) + \dot{r}_i'''
\end{aligned} \tag{84}$$

## Geometry

The total flow area or cross-sectional area of the channel in the melting zone is given by

$$A_c = A_{c_s} + A_{c_m} \tag{85}$$

$$A_c = hW \tag{86}$$

$$A_{c_s} = hW_s \tag{87}$$

$$A_{c_m} = hW - hW_s \tag{88}$$

where  $A_c$  is the channel of cross-sectional area,  $A_{c_s}$  is the solid bed flow area,  $A_{c_m}$  is the melt pool flow area and  $W_s$  is the solid bed width in the channel. Figure 27 shows the geometric measurements taken from the screw radius  $r$  and the  $R^2$  values for each polynomial fitted to the piecewise function shown in Equation (89).

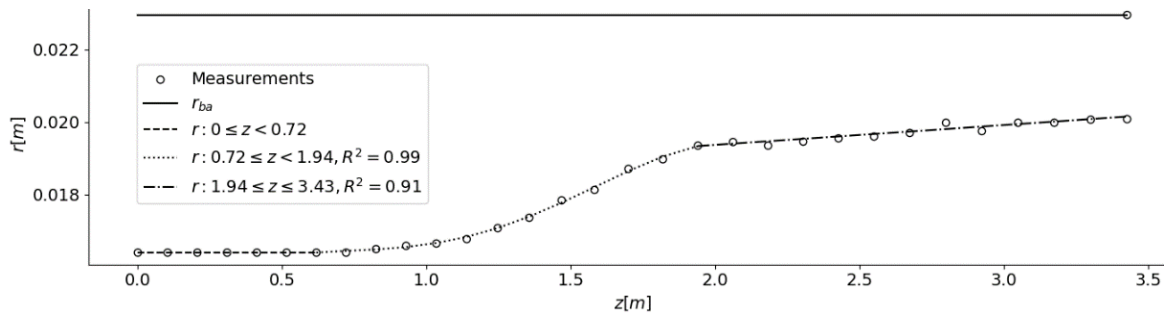


Figure 27. Screw radius.

$$r = \begin{cases} 16.41 \times 10^{-3}, & \text{if } z < 0.72 \\ -27.51 \times 10^{-4}z^4 + 12.82 \times 10^{-3}z^3 - 19.39 \times 10^{-3}z^2 + 12.45 \times 10^{-3}z + 13.49 \times 10^{-3}, & \text{if } 0.72 \leq z < 1.94 \\ 54.60 \times 10^{-5}z + 18.28 \times 10^{-3}, & \text{if } z \geq 1.94 \end{cases} \quad (89)$$

the channel height  $h$  is given by

$$h = r_{ba} - r \quad (90)$$

where  $r_{ba}$  is the barrel radius. The heat transfer area of the solid bed with the barrel wall can be viewed as a trapezoid, as shown below

$$A_s = A_T - A_m = \left( W_s|_z + W_s|_{z+\partial z} \right) \frac{\partial z}{2} = \left( A_{cs}|_z + A_{cs}|_{z+\partial z} \right) \frac{\partial z}{2h} \quad (91)$$

$$A_m = Wdz - A_s \quad (92)$$

where  $A_T$ ,  $A_s$  and  $A_m$  are the heat transfer area of the two phases, the solid phase, and the melt phase, respectively.  $W_s|_z$  and  $W_s|_{z+\partial z}$  are the channel width of the solid bed at  $z$  and  $z + \partial z$ , respectively. The volume of the solid bed  $V_s$  and the melt pool  $V_m$  in the fluid element are given by

$$V_s = A_s h \quad (93)$$

$$V_m = V_T - V_s \quad (94)$$

$$V_T = A_c dz \quad (95)$$

the total volume  $V_T$  in the fluid element can also be defined as  $V_T = V_s + V_m$ . Additionally, we have  $h = f(z)$ ,  $W_s = f(t, z)$  and  $W_m = f(t, z)$ . Now, differentiating Equations (85) and (86) with respect to  $t$

$$\frac{\partial A_c}{\partial t} = \frac{\partial A_{cs}}{\partial t} + \frac{\partial A_{cm}}{\partial t} \quad (96)$$

$$\frac{\partial A_c}{\partial t} = \frac{\partial (hW)}{\partial t} = 0 \quad (97)$$

substituting Equation (97) into Equation (96), we obtain

$$\frac{\partial A_{cm}}{\partial t} = -\frac{\partial A_{cs}}{\partial t} \quad (98)$$

the unit analysis of Equation (98) is as follows

$$\left[ \frac{m^2}{s} \right] = - \left[ \frac{m^2}{s} \right] \quad (99)$$

differentiating Equation (2) with respect to  $z$  we obtain

$$\frac{\partial A_c}{\partial z} = W \frac{\partial h}{\partial z} \quad (100)$$

differentiating Equations (89) and (90) with respect to  $z$  we arrive at

$$\frac{\partial r}{\partial z} = \begin{cases} 0, & \text{if } z < 0.72 \\ -110.04 \times 10^{-4} z^3 + 38.46 \times 10^{-3} z^2 - 38.78 \times 10^{-3} z + 24.90 \times 10^{-3}, & \text{if } 0.72 \leq z < 1.94 \\ 54.60 \times 10^{-5}, & \text{if } z \geq 1.94 \end{cases} \quad (101)$$

$$\frac{\partial h}{\partial z} = -\frac{\partial r}{\partial z} \quad (102)$$

## PS<sub>I</sub> - Solids Conveying Zone

The solids in the solid conveying zone are approximated as a fluid and pressure changes are negligible. The physical properties, such as specific heat capacity of the solid  $C_{ps}$ , the overall heat transfer coefficient from the barrel to the solid  $U_s$ , and the solid density  $\rho_s$ , are constant. The balances in the fluid element are developed based on these assumptions.

**Momentum Balance:** the transient momentum transport in the mass direction dissipates before any substantial change in the location of the material occurs. The solid bed is adhered to the screw walls. The screw velocity is taken as the velocity of the solid, it results in

$$u_{zs} = r\omega \quad (103)$$

the spatial gradient of the velocity is

$$\frac{\partial u_{z_s}}{\partial z} = \frac{\partial r}{\partial z} \omega \quad (104)$$

The unit analysis of Equation (104) is as follows

$$\left[ \frac{m}{s \ m} \right] = \left[ \frac{m}{m} \right] \left[ \frac{1}{s} \right] \quad (105)$$

$$\left[ \frac{m}{s \ m} \right] = \left[ \frac{m}{s \ m} \right] \quad (106)$$

**Internal Energy Balance:** for an incompressible fluid, it follows that  $C_{V_s} \approx C_{p_s}$ . The accumulation term of the fluid component is given by

$$\frac{\partial(\delta x \delta y \delta z \rho_s C_{p_s} T_s)}{\partial t} = \delta x \delta y \delta z \rho_s C_{p_s} \frac{\partial T_s}{\partial t} \quad (107)$$

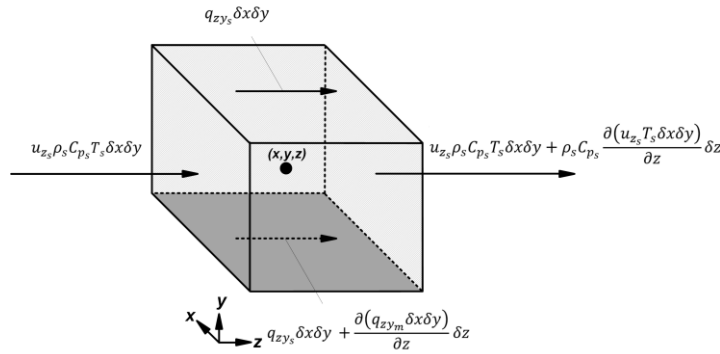


Figure 28. Internal energy balance in and out of the fluid element in the solids conveying zone.

Heat transfer occurs in the  $y$ -axis but varies only along  $z$ -axis, while the flow area changes with  $z$ . In Figure 28, the convective term and non-convective term across its boundaries are represented by

$$\begin{aligned} & u_{z_s} \rho_s C_{p_s} T_s \delta x \delta y - \left( u_{z_s} \rho_s C_{p_s} T_s \delta x \delta y + \rho_s C_{p_s} \frac{\partial(u_{z_s} T_s \delta x \delta y)}{\partial z} \delta z \right) \\ & = -\rho_s C_{p_s} \frac{\partial(u_{z_s} T_s \delta x \delta y)}{\partial z} \delta z \end{aligned} \quad (108)$$

$$q_{zy_s} \delta x \delta y - \left( q_{zy_s} \delta x \delta y + \frac{\partial(q_{zy_m} \delta x \delta y)}{\partial z} \delta z \right) = - \frac{\partial(q_{zy_m} \delta x \delta y)}{\partial z} \delta z \quad (109)$$

the internal energy balance in the fluid element is then shown

$$\delta x \delta y \delta z \rho_s C_{p_s} \frac{\partial T_s}{\partial t} = -\rho_s C_{p_s} \frac{\partial(u_{z_s} T_s \delta x \delta y)}{\partial z} \delta z - \frac{\partial(q_{zy_m} \delta x \delta y)}{\partial z} \delta z \quad (110)$$

replacing  $\delta x \delta y$  with  $A_c$ , it results in

$$\rho_s C_{p_s} A_c \frac{\partial T_s}{\partial t} = -\rho_s C_{p_s} \frac{\partial(u_{z_s} T_s A_c)}{\partial z} - \frac{\partial(q_{zy_m} A_c)}{\partial z} \quad (111)$$

the non-convective term or heat transfer term, is expressed as

$$\frac{\partial q_{zy_s}}{\partial z} \Big|_0^z = - \frac{A_T U_s}{V_T} (T_b - T_s) \quad (112)$$

$$q_{zy_s} \Big|_0^z = -U_s (T_b - T_s) \quad (113)$$

by differentiating and rearranging the Equation (111), we obtain

$$\rho_s C_{p_s} A_c \frac{\partial T_s}{\partial t} = -\rho_s C_{p_s} u_{z_s} A_c \frac{\partial T_s}{\partial z} - \rho_s C_{p_s} u_{z_s} T_s \frac{\partial A_c}{\partial z} - \rho_s C_{p_s} A_c T_s \frac{\partial u_{z_s}}{\partial z} - A_c \frac{\partial q_{zy_s}}{\partial z} \Big|_0^{dz} - q_{zy_s} \Big|_0^{dz} \frac{\partial A_c}{\partial z} \quad (114)$$

$$\frac{\partial T_s}{\partial t} = -u_{z_s} \frac{\partial T_s}{\partial z} - \frac{u_{z_s} T_s}{A_c} \frac{\partial A_c}{\partial z} - T_s \frac{\partial u_{z_s}}{\partial z} - \frac{1}{\rho_s C_{p_s}} \frac{\partial q_{zy_s}}{\partial z} \Big|_0^{dz} - \frac{q_{zy_s} \Big|_0^{dz}}{\rho_s C_{p_s} A_c} \frac{\partial A_c}{\partial z} \quad (115)$$

the unit analysis of Equation (115) is as follows

$$\begin{aligned}
\left[\frac{K}{s}\right] = & -[K] \left[\frac{m^3}{kg}\right] \left[\frac{kg}{m^3 s}\right] - \left[\frac{m}{s}\right] \left[\frac{K}{m}\right] - \left[\frac{m}{s}\right] [K] \left[\frac{m^3}{kg}\right] \left[\frac{kg}{m^3 m}\right] \\
& - \left[\frac{m}{s}\right] [K] \frac{1}{[m^2]} \left[\frac{m^2}{m}\right] - [K] \left[\frac{m}{s m}\right] \\
& - \left[\frac{m^3}{kg}\right] \left[\frac{kg K}{J}\right] \frac{[m^2]}{[m^3]} \left[\frac{J}{s m^2 K}\right] [K] \\
& - \left[\frac{m^3}{kg}\right] \left[\frac{kg K}{J}\right] \frac{1}{[m^2]} \left[\frac{J}{s m^2 K}\right] [K] \left[\frac{m^2}{m}\right]
\end{aligned} \tag{116}$$

$$\left[\frac{K}{s}\right] = - \left[\frac{K}{s}\right] - \left[\frac{K}{s}\right] - \left[\frac{K}{s}\right] - \left[\frac{K}{s}\right] - \left[\frac{K}{s}\right] - \left[\frac{K}{s}\right] - \left[\frac{K}{s}\right] \tag{117}$$

## PS<sub>II</sub> - Melting Zone

PS<sub>II</sub> is the change of state of polypropylene from solid bed to melt pool and is composed of PS<sub>III</sub> and PS<sub>IV</sub>. It is assumed that the total pressure of the system is given in the melt pool in PS<sub>IV</sub>.

**Mass Balance:** the total mass of PS<sub>II</sub> is given by Equation (118).

$$\dot{m} = \dot{m}_m + \dot{m}_s \tag{118}$$

where  $\dot{m}$ ,  $\dot{m}_s$ , and  $\dot{m}_m$  are the total, solid bed, and melt mass flow rates, respectively.

## PS<sub>III</sub> - Solid Bed

The physical properties of the solid bed in the melting zone, such as specific heat capacity  $C_{p_s}$ , solid density  $\rho_s$  and overall heat transfer coefficient from the barrel to the solid bed  $U_s$ , are constant. The balances in the fluid element are developed based on these assumptions.

**Mass Balance:** the flow area for the solid bed changes with  $t$ ; therefore, the accumulation term of the fluid component is

$$\frac{\partial(\rho_s \delta_x \delta_y \delta_z)}{\partial t} = \rho_s \frac{\partial(\delta x \delta y)}{\partial t} \delta z \tag{119}$$

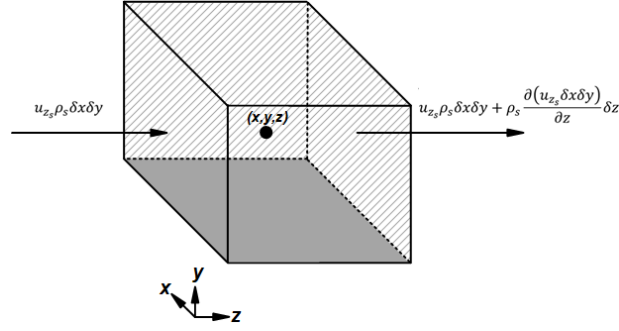


Figure 29. Mass balance in and out of the fluid element for the solid bed in the melting zone.

The convective term is given by the product of the solid bed density  $\rho_s$  and the component of the velocity  $u_{z_s}$  normal to the face. Figure 29 shows that the net mass flow into the element through its boundaries is given by:

$$u_{z_s} \rho_s \delta x \delta y - \left( u_{z_s} \rho_s \delta x \delta y + \rho_s \frac{\partial(u_{z_s} \delta x \delta y)}{\partial z} \delta z \right) = -\rho_s \frac{\partial(u_{z_s} \delta x \delta y)}{\partial z} \delta z \quad (120)$$

the source term into the element across its boundaries is given by

$$\delta x \delta y \delta z \dot{r}_k''' = -\delta x \delta y \delta z \dot{r}_s''' \quad (121)$$

the mass balance in the fluid element is then shown

$$\rho_s \frac{\partial(\delta x \delta y)}{\partial t} \delta z = -\rho_s \frac{\partial(u_{z_s} \delta x \delta y)}{\partial z} \delta z + \delta x \delta y \delta z \dot{r}_s''' \quad (122)$$

replacing  $\delta x \delta y$  with  $A_{c_s}$ , it results in

$$\rho_s \frac{\partial A_{c_s}}{\partial t} = -\frac{\partial(u_{z_s} A_{c_s} \rho_s)}{\partial z} + A_{c_s} \dot{r}_s''' \quad (123)$$

by differentiating and rearranging the Equation (123), we obtain

$$\frac{\partial A_{c_s}}{\partial t} = -u_{z_s} \frac{\partial A_{c_s}}{\partial z} - A_{c_s} \frac{\partial u_{z_s}}{\partial z} + \frac{A_{c_s}}{\rho_s} \dot{r}_s''' \quad (124)$$

the melting rate is obtained from

$$\dot{r}_s''' = -A_0 e^{\left(\frac{-E_{a_s}}{T_s R_g}\right)} \rho_s \quad (125)$$

where  $A_0$  is the pre-exponential factor,  $E_{a_s}$  is the activation energy, and  $R_g$  is the ideal gas constant. The unit analysis of Equation (124) is as follows

$$\left[\frac{m^2}{s}\right] = -\left[\frac{m}{s}\right] \left[\frac{m^2}{m}\right] - [m^2] \left[\frac{m}{s m}\right] - [m^2] \left[\frac{m^3}{kg}\right] \left[\frac{kg}{m^3 s}\right] \quad (126)$$

$$\left[\frac{m^2}{s}\right] = -\left[\frac{m^2}{s}\right] - \left[\frac{m^2}{s}\right] - \left[\frac{m^2}{s}\right] \quad (127)$$

**Momentum Balance:** the transient momentum transport in the mass direction dissipates before any substantial change in the location of the material occurs. The solid bed is adhered to the screw walls. The screw velocity is taken as the velocity of the solid, it results in

$$u_{z_s} = r \omega \quad (128)$$

the spatial gradient of the velocity is

$$\frac{\partial u_{z_s}}{\partial z} = \frac{\partial r}{\partial z} \omega \quad (129)$$

the unit analysis of Equation (129) is as follows

$$\left[\frac{m}{s m}\right] = \left[\frac{m}{m}\right] \left[\frac{1}{s}\right] \quad (130)$$

$$\left[\frac{m}{s m}\right] = \left[\frac{m}{s m}\right] \quad (131)$$

**Internal Energy Balance:** for an incompressible fluid, it follows that  $C_{V_s} \approx C_{p_s}$ . The accumulation term of the fluid component is given by

$$\frac{\partial(\delta x \delta y \delta z \rho_s C_{p_s} T_s)}{\partial t} = \rho_s C_{p_s} \frac{\partial(\delta x \delta y T_s)}{\partial t} \delta_z \quad (132)$$

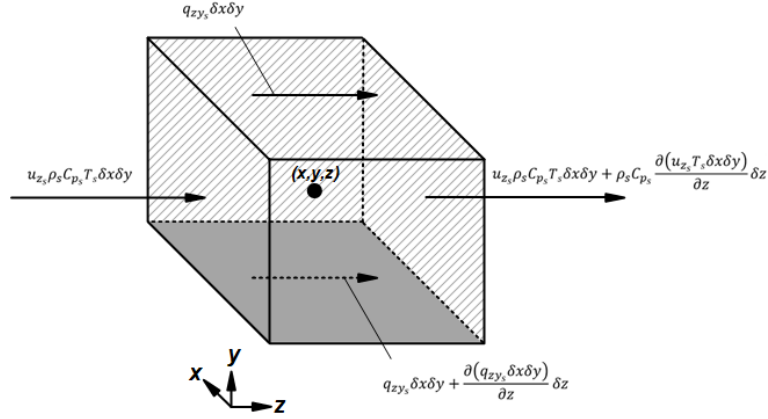


Figure 30. Internal energy balance in and out of the fluid element for the solid bed in the melting zone.

Heat transfer occurs in the  $y$ -axis but varies only along the  $z$ -axis, while the flow area changes with  $z$ . In Figure 30, the convective term and non-convective term across its boundaries are represented by

$$u_{zs} \rho_s C_{ps} T_s \delta x \delta y - \left( u_{zs} \rho_s C_{ps} T_s \delta x \delta y + \rho_s C_{ps} \frac{\partial(u_{zs} T_s \delta x \delta y)}{\partial z} \delta z \right) = -\rho_s C_{ps} \frac{\partial(u_{zs} T_s \delta x \delta y)}{\partial z} \delta z \quad (133)$$

$$q_{zy_s} \delta x \delta y - \left( q_{zy_s} \delta x \delta y + \frac{\partial(q_{zy_s} \delta x \delta y)}{\partial z} \delta z \right) = -\frac{\partial(q_{zy_s} \delta x \delta y)}{\partial z} \delta z \quad (134)$$

the non-convective term, or heat transfer term, is expressed as

$$\frac{\partial q_{zy_s}}{\partial z} \Big|_0^{dz} = -\frac{A_s U_s}{V_s} (T_b - T_s) \quad (135)$$

$$q_{zy_s} \Big|_0^{dz} = -U_s (T_b - T_s) \quad (136)$$

the source term into the element across its boundaries is given by

$$\delta x \delta y \delta z \dot{r}_i''' = -\delta x \delta y \delta z \Delta \hat{h}_{sm} \dot{r}_s''' \quad (137)$$

the energy balance in the fluid element is then shown

$$\rho_s C_{p_s} \frac{\partial(T_s \delta x \delta y)}{\partial t} \delta z = -\rho_s C_{p_s} \frac{\partial(u_{z_s} T_s \delta x \delta y)}{\partial z} \delta z - \frac{\partial(q_{z y_s} \delta x \delta y)}{\partial z} \delta z - \delta x \delta y \delta z \Delta \hat{h}_{sm} \dot{r}_s''' \quad (138)$$

replacing  $\delta x \delta y$  with  $A_{c_s}$ , it results in

$$\rho_s C_{p_s} \frac{\partial(T_s A_{c_s})}{\partial t} = -\rho_s C_{p_s} \frac{\partial(u_{z_s} T_s A_{c_s})}{\partial z} - \frac{\partial(q_{z y_s} A_{c_s})}{\partial z} - A_{c_s} \Delta \hat{h}_{sm} \dot{r}_s''' \quad (139)$$

by differentiating and rearranging the Equation (139), we obtain

$$\begin{aligned} \rho_s C_{p_s} A_{c_s} \frac{\partial T_s}{\partial t} + \rho_s C_{p_s} T_s \frac{\partial A_{c_s}}{\partial t} \\ = -\rho_s C_{p_s} u_{z_s} A_{c_s} \frac{\partial T_s}{\partial z} - \rho_s C_{p_s} T_s A_{c_s} \frac{\partial u_{z_s}}{\partial z} - \rho_s C_{p_s} u_{z_s} T_s \frac{\partial A_{c_s}}{\partial z} \\ - A_{c_s} \left. \frac{\partial q_{z y_s}}{\partial z} \right|_0^{dz} - q_{z y_s} \Big|_0^{dz} \frac{\partial A_{c_s}}{\partial z} - A_{c_s} \Delta \hat{h}_{sm} \dot{r}_s''' \end{aligned} \quad (140)$$

$$\begin{aligned} \frac{\partial T_s}{\partial t} = -\frac{T_s}{A_{c_s}} \frac{\partial A_{c_s}}{\partial t} - u_{z_s} \frac{\partial T_s}{\partial z} - T_s \frac{\partial u_{z_s}}{\partial z} - \frac{u_{z_s} T_s}{A_{c_s}} \frac{\partial A_{c_s}}{\partial z} - \frac{1}{\rho_s C_{p_s}} \left. \frac{\partial q_{z y_s}}{\partial z} \right|_0^{dz} \\ - \frac{1}{\rho_s C_{p_s} A_{c_s}} q_{z y_s} \Big|_0^{dz} \frac{\partial A_{c_s}}{\partial z} - \frac{1}{\rho_s C_{p_s}} \Delta \hat{h}_{sm} \dot{r}_s''' \end{aligned} \quad (141)$$

The unit analysis of Equation (141) is as follows

$$\begin{aligned} \left[ \frac{K}{s} \right] = -\left[ \frac{K}{m^2} \right] \left[ \frac{m^2}{s} \right] - \left[ \frac{m}{s} \right] \left[ \frac{K}{m} \right] - [K] \left[ \frac{m}{s m} \right] - \left[ \frac{m}{s} \right] \left[ \frac{K}{m^2} \right] \left[ \frac{m^2}{m} \right] \\ - \left[ \frac{m^3}{kg} \right] \left[ \frac{kg K}{J} \right] \left[ \frac{m^2}{m^3} \right] \left[ \frac{J}{s m^2 K} \right] [K] \\ - \left[ \frac{m^3}{kg} \right] \left[ \frac{kg K}{J} \right] \frac{1}{m^2} \left[ \frac{J}{s m^2 K} \right] [K] \left[ \frac{m^2}{m} \right] \\ - \left[ \frac{m^3}{kg} \right] \left[ \frac{kg K}{J} \right] \left[ \frac{J}{kg} \right] \left[ \frac{kg}{m^3 s} \right] \end{aligned} \quad (142)$$

$$\left[\frac{K}{s}\right] = -\left[\frac{K}{s}\right] - \left[\frac{K}{s}\right] - \left[\frac{K}{s}\right] - \left[\frac{K}{s}\right] - \left[\frac{K}{s}\right] - \left[\frac{K}{s}\right] - \left[\frac{K}{s}\right] \quad (143)$$

## PS<sub>IV</sub> - Melt Pool

The physical properties of the melt pool in the melting zone, such as specific heat capacity  $C_{p_m}$ , solid density  $\rho_m$  and overall heat transfer coefficient from the barrel to the melt pool  $U_m$ , are constant. The balances in the fluid element are developed based on these assumptions.

**Mass Balance:** the flow area for the melt flow changes with  $z$ ; therefore, the accumulation term of the fluid component is

$$\frac{\partial(\rho_m \delta x \delta y \delta z)}{\partial t} = \rho_m \frac{\partial(\delta x \delta y)}{\partial t} \delta z \quad (144)$$

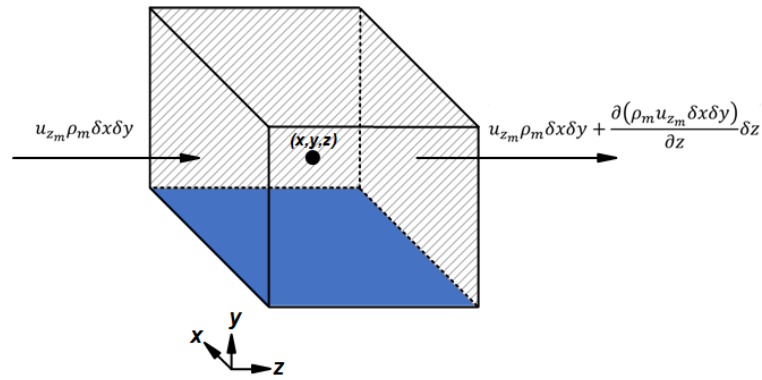


Figure 31. Mass balance in and out of the fluid element for melt pool in the melting zone.

The convective term is given by the product of the melt pool density  $\rho_m$  and the component of the velocity  $u_{z_m}$  normal to the face and the flow area changes with  $z$ . Figure 31 shows that the net mass flow into the element through its boundaries is given by:

$$u_{z_m} \rho_m \delta x \delta y - \left( u_{z_m} \rho_m \delta x \delta y + \frac{\partial(\rho_m u_{z_m} \delta x \delta y)}{\partial z} \delta z \right) = - \frac{\partial(\rho_m u_{z_m} \delta x \delta y)}{\partial z} \delta z \quad (145)$$

the source term into the element across its boundaries is given by

$$\delta x \delta y \delta z \dot{r}_m''' = \delta x \delta y \delta z \dot{r}_s''' \quad (146)$$

the source term in the element across its boundaries is given by Equation (125). The mass balance in the fluid element is then shown

$$\rho_m \frac{\partial(\delta x \delta y)}{\partial t} \delta z = -\rho_m \frac{\partial(u_{z_m} \delta x \delta y)}{\partial z} \delta z - \delta x \delta y \delta z \dot{r}_s''' \quad (147)$$

replacing  $\delta x \delta y$  with  $A_{c_m}$  and  $\dot{m}_m = \rho_m A_{c_m} u_{z_m}$  it results in

$$\frac{\partial \dot{m}_m}{\partial z} = -\rho_m \frac{\partial A_{c_m}}{\partial t} - A_{c_m} \dot{r}_s''' \quad (148)$$

the unit analysis of Equation (148) is as follows

$$\left[ \frac{kg}{s \cdot m} \right] = - \left[ \frac{kg}{m^3} \right] \left[ \frac{m^2}{s} \right] + [m^2] \left[ \frac{kg}{m^3 \cdot s} \right] \quad (149)$$

$$\left[ \frac{kg}{m \cdot s} \right] = - \left[ \frac{kg}{m \cdot s} \right] + \left[ \frac{kg}{m \cdot s} \right] \quad (150)$$

**Momentum Balance:** the transient momentum transport in the mass direction dissipates before any substantial change in the location of the material occurs.

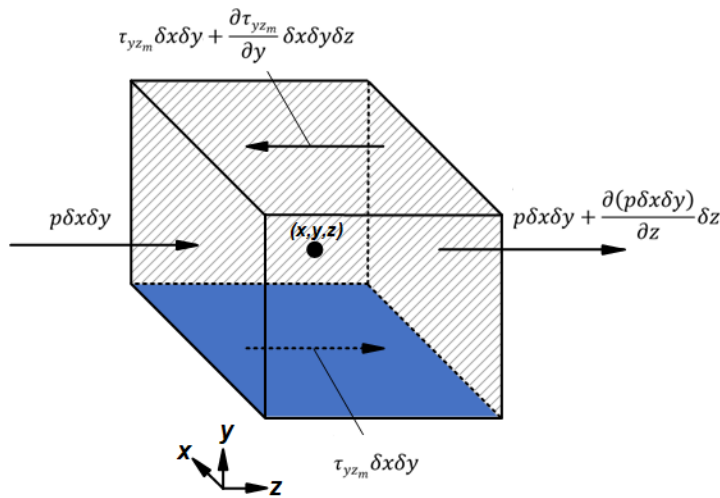


Figure 32. Momentum balance in and out of the fluid element for melt pool in the melting zone.

It is assumed that  $\frac{\partial u_{zm}}{\partial y} \gg \frac{\partial u_{zm}}{\partial z}$ . Figure 32 shows that the z-direction components of forces due to pressure  $p$  and the stress tensor component  $\tau_{yzm}$  are considered. The magnitude of a force resulting from surface stress is calculated by multiplying the stress by the area. Forces aligned with the direction of a coordinate axis are considered positive, while those in the opposite direction are considered negative.

$$p\delta x\delta y - \left( p\delta x\delta y + \frac{\partial(p\delta x\delta y)}{\partial z} \delta z \right) = -\frac{\partial(p\delta x\delta y)}{\partial z} \delta z \quad (151)$$

$$-\tau_{yzm} \delta x\delta y - \left[ -\left( \tau_{yzm} \delta x\delta y\delta z + \frac{\partial\tau_{yzm}}{\partial y} \delta x\delta y\delta z \right) \right] = \frac{\partial\tau_{yzm}}{\partial y} \delta x\delta y\delta z \quad (152)$$

the component of viscous stress is

$$\tau_{yzm} = -\mu\dot{\gamma}_{yzm} = -\mu \left( \frac{\partial u_{ym}}{\partial z} + \frac{\partial u_{zm}}{\partial y} \right) \quad (153)$$

$u_{ym}$  is not taken into account. The momentum balance in the fluid element is then shown

$$\frac{\partial(p\delta x\delta y)}{\partial z} \delta z = -\frac{\partial\tau_{yzm}}{\partial y} \delta x\delta y\delta z \quad (154)$$

replacing Equation (153) into Equation (154) and substituting  $\delta x\delta y$  with  $A_{cm}$ , results in the following expression

$$\mu A_{cm} \frac{\partial}{\partial y} \left( \frac{\partial u_{zm}}{\partial y} \right) = \frac{\partial(pA_{cm})}{\partial z} \quad (155)$$

by differentiating and rearranging the Equation (155), we obtain

$$\mu A_{cm} \frac{\partial^2 u_{zm}}{\partial y^2} = A_{cm} \frac{\partial p}{\partial z} + p \frac{\partial A_{cm}}{\partial z} \quad (156)$$

$$\frac{\partial^2 u_{zm}}{\partial y^2} = \frac{1}{\mu} \frac{\partial p}{\partial z} + \frac{p}{\mu A_{cm}} \frac{\partial A_{cm}}{\partial z} \quad (157)$$

the unit analysis of Equation (157) is as follows

$$\left[ \frac{1}{s \, m} \right] = \left[ \frac{m \, s}{kg} \right] \left[ \frac{kg}{m \, s^2 \, m} \right] + \left[ \frac{kg}{m \, s^2} \right] \left[ \frac{m \, s}{kg} \right] \left[ \frac{1}{m^2} \right] \left[ \frac{m^2}{m} \right] \quad (158)$$

$$\left[ \frac{1}{s \, m} \right] = \left[ \frac{1}{s \, m} \right] + \left[ \frac{1}{s \, m} \right] \quad (159)$$

solving for  $\frac{\partial^2 u_{zm}}{\partial y^2}$  from Equation (157) and taking  $\frac{\partial^2 u_{zm}}{\partial y^2} = \beta$ , then integrating twice with respect to  $y$ , we obtain

$$\frac{\partial^2 u_{zm}}{\partial y^2} = \frac{1}{\eta} \frac{\partial p}{\partial z} + \frac{p}{\eta A_{c_m}} \frac{\partial A_{c_m}}{\partial z} \quad (160)$$

$$\beta = \frac{1}{\eta} \frac{\partial p}{\partial z} + \frac{p}{\eta A_{c_m}} \frac{\partial A_{c_m}}{\partial z} \quad (161)$$

$$\int \frac{\partial^2 u_{zm}}{\partial y^2} dy = \int \beta dy \quad (162)$$

$$\frac{\partial u_{zm}}{\partial y} = \beta y + C_1 \quad (163)$$

$$\int \frac{\partial u_{zm}}{\partial y} dy = \int (\beta y + C_1) dy \quad (164)$$

$$u_{zm}(y) = \frac{\beta}{2} y^2 + C_1 y + C_2 \quad (165)$$

where the boundary conditions are

$$u_{zm}(y = 0) = \omega r = u_{zs} \quad (166)$$

$$u_{zm}(y = h) = 0 \quad (167)$$

the values of  $C_1$  and  $C_2$  are

$$C_1 = -\left(\frac{1}{2}\beta h + \frac{u_{z_s}}{h}\right) \quad (168)$$

$$C_2 = u_{z_s} \quad (169)$$

replacing the Equations (168) and (169) into Equations (163) and (165), we obtain

$$\frac{\partial u_{z_m}}{\partial y} = \beta y - \left(\frac{1}{2}\beta h + \frac{u_{z_s}}{h}\right) \quad (170)$$

$$u_{z_m}(y) = \frac{\beta}{2}y^2 - \left(\frac{1}{2}\beta h + \frac{u_{z_s}}{h}\right)y + u_{z_s} \quad (171)$$

the mean of Equation (170) is given by

$$\left\langle \frac{\partial u_{z_m}}{\partial y} \right\rangle_{[0,h]} = \frac{1}{h} \int_0^h \frac{\partial u_{z_m}}{\partial y} dy = \frac{1}{h} u_{z_m} \Big|_0^h \quad (172)$$

$$\left\langle \frac{\partial u_{z_m}}{\partial y} \right\rangle_{[0,h]} = \frac{1}{h} \left( \frac{1}{2}\beta y^2 - \left(\frac{1}{2}\beta h + \frac{u_{z_s}}{h}\right)y + u_{z_s} \right) \Big|_0^h \quad (173)$$

by performing the operations, we arrive at

$$\left\langle \frac{\partial u_{z_m}}{\partial y} \right\rangle_{[0,h]} = -\frac{u_{z_s}}{h} \quad (174)$$

the mean of Equation (171) is given by

$$\langle u_{z_m} \rangle = \frac{1}{h} \int_0^h u_{z_m}(y) dy \quad (175)$$

$$\langle u_{z_m} \rangle = \frac{1}{h} \left( \frac{1}{6}\beta y^3 - \left(\frac{1}{4}\beta h + \frac{u_{z_s}}{2h}\right)y^2 + u_{z_s}y \right) \Big|_0^h \quad (176)$$

by performing the operations, we arrive at

$$\langle u_{z_m} \rangle = u_{z_m} = \frac{u_{z_s}}{2} - \frac{1}{12} h^2 \beta \quad (177)$$

replacing  $\beta$  in Equation (177) and rearranging, we arrive at

$$\frac{\partial p}{\partial z} = 6 \frac{\mu u_{z_s}}{h^2} - 12 \frac{\mu u_{z_m}}{h^2} - \frac{p}{A_{c_m}} \frac{\partial A_{c_m}}{\partial z} \quad (178)$$

the unit analysis of Equation (178) is as follows

$$\left[ \frac{kg}{m s^2 m} \right] = \left[ \frac{kg}{m s} \right] \left[ \frac{m}{s} \right] \frac{1}{[m^2]} - \left[ \frac{kg}{m s} \right] \left[ \frac{m}{s} \right] \frac{1}{[m^2]} - \left[ \frac{kg}{m s^2} \right] \frac{1}{[m^2]} \left[ \frac{m^2}{m} \right] \quad (179)$$

$$\left[ \frac{kg}{m^2 s^2} \right] = \left[ \frac{kg}{m^2 s^2} \right] - \left[ \frac{kg}{m^2 s^2} \right] - \left[ \frac{kg}{m^2 s^2} \right] \quad (180)$$

the mean velocity of the melt pool is given by

$$u_{z_m} = \frac{\dot{m}_m}{\rho_m A_{c_m}} \quad (181)$$

differentiating Equation (181) with respect to  $z$  yields

$$\frac{\partial u_{z_m}}{\partial z} = \frac{1}{\rho_m A_{c_m}} \frac{\partial \dot{m}_m}{\partial z} - \frac{\dot{m}_m}{\rho_m A_{c_m}^2} \frac{\partial A_{c_m}}{\partial z} \quad (182)$$

There are several types of empirical models for the stress tensor of non-Newtonian fluids, one of which is the generalized Newtonian model. The stress tensor for incompressible Newtonian fluids is given by Equation (183):

$$\tau = -\mu(\nabla \mathbf{u} + (\nabla \mathbf{u})^T) \equiv -\mu \dot{\gamma} \quad (183)$$

where  $\dot{\gamma}$  is the rate-of-strain tensor. The generalized Newtonian fluid model is shown in Equation (184), which is obtained by simply substituting the Newtonian viscosity  $\mu$  with the non-Newtonian viscosity  $\eta$ , which is a function of  $\dot{\gamma}$ .

$$\tau = -\eta(\nabla \mathbf{u} + (\nabla \mathbf{u})^T) \equiv -\eta \dot{\gamma} \quad (184)$$

The viscosity  $\eta$  is given by the Carreau-Arrhenius model as follows

$$\eta = \frac{a_T A}{(1 + a_T B |\dot{\gamma}|)^C} \quad (185)$$

$$a_T = e^{\frac{E_{a\eta}}{Rg} \left( \frac{1}{T_m} - \frac{1}{T_{ref}} \right)} \quad (186)$$

$$|\dot{\gamma}| = \sqrt{\frac{1}{2} (\dot{\gamma} : \dot{\gamma})} \quad (187)$$

$$\frac{1}{2} (\dot{\gamma} : \dot{\gamma}) = 2 \left( \frac{\partial u_{zm}}{\partial z} \right)^2 + \left( \frac{\partial u_{zm}}{\partial y} \right)^2 \quad (188)$$

$$|\dot{\gamma}| = \left[ 2 \left( \frac{\partial u_{zm}}{\partial z} \right)^2 + \left( \frac{\partial u_{zm}}{\partial y} \right)^2 \right]^{0.5} \quad (189)$$

by approximating  $\frac{\partial u_{zm}}{\partial y} \approx \langle \frac{\partial u_{zm}}{\partial y} \rangle_{[0,h]}$ , we arrive at

$$|\dot{\gamma}| = \left[ 2 \left( \frac{\partial u_{zm}}{\partial z} \right)^2 + \left( \langle \frac{\partial u_{zm}}{\partial y} \rangle_{[0,h]} \right)^2 \right]^{0.5} \quad (190)$$

**Internal Energy Balance:** for an incompressible fluid, it follows that  $C_{V_m} \approx C_{p_m}$ . The accumulation term of the fluid component is given by

$$\frac{\partial(\delta x \delta y \delta z \rho_m C_{p_m} T_m)}{\partial t} = \rho_m C_{p_m} \frac{\partial(\delta x \delta y T_m)}{\partial t} \delta z \quad (191)$$

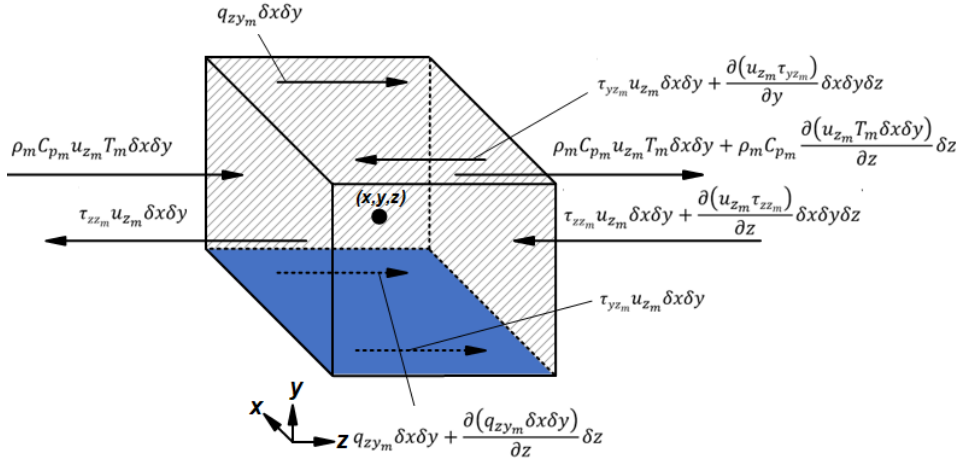


Figure 33. Internal energy balance in and out of the fluid element for the solid bed in the melting zone.

Heat transfer occurs in the  $y$ -axis but varies only along the  $z$ -axis, while the flow area changes with  $z$ . In Figure 33, the convective term and non-convective term across its boundaries are represented by

$$\begin{aligned} \rho_m C_{p_m} u_{z_m} T_m \delta x \delta y - \left( \rho_m C_{p_m} u_{z_m} T_m \delta x \delta y + \rho_m C_{p_m} \frac{\partial (u_{z_m} T_m \delta x \delta y)}{\partial z} \delta z \right) \\ = -\rho_m C_{p_m} \frac{\partial (u_{z_m} T_m \delta x \delta y)}{\partial z} \delta z \end{aligned} \quad (192)$$

$$-q_{zy_m} \delta x \delta y - \left[ - \left( q_{zy_m} \delta x \delta y - \frac{\partial (q_{zy_m} \delta x \delta y)}{\partial z} \delta z \right) \right] = -\frac{\partial (q_{zy_m} \delta x \delta y)}{\partial z} \delta z \quad (193)$$

the non-convective energy term or heat transfer term, is expressed as

$$\frac{q_{zy_m}}{\partial z} \Big|_0^z = \int_0^z \frac{q_{zy_m}}{\partial z} \partial z = -\frac{A_m U_m}{V_m} (T_b - T_m) \quad (194)$$

$$q_{zy_m} \Big|_0^z = -U_m (T_b - T_m) \quad (195)$$

the sum of internal (thermal), kinetic and gravitational potential energies are common ways to describe the energy of a fluid. The viscous dissipation terms for the energy balance are as follows

$$-\tau_{zzm} u_{zm} \delta x \delta y + \left( \tau_{zzm} u_{zm} \delta x \delta y + \frac{\partial(u_{zm} \tau_{zzm} \delta x \delta y)}{\partial z} \delta z \right) = \frac{\partial(u_{zm} \tau_{zzm} \delta x \delta y)}{\partial z} \delta z \quad (196)$$

$$-\tau_{yzm} u_{zm} \delta x \delta y + \left( \tau_{yzm} u_{zm} \delta x \delta y + \frac{\partial(u_{zm} \tau_{yzm})}{\partial y} \delta x \delta y \delta z \right) = \frac{\partial(u_{zm} \tau_{yzm})}{\partial y} \delta x \delta y \delta z \quad (197)$$

when extracting the changes in mechanical energy from the total energy to obtain the changes in internal energy, Equations (196) and (197) becomes

$$\frac{\partial(u_{zm} \tau_{zzm} \delta x \delta y)}{\partial z} \delta z - u_{zm} \frac{\partial \tau_{zzm}}{\partial z} \delta x \delta y \delta z = \tau_{zzm} \frac{\partial(u_{zm} \delta x \delta y)}{\partial z} \delta z \quad (198)$$

$$\frac{\partial(u_{zm} \tau_{yzm})}{\partial y} \delta x \delta y \delta z - u_{zm} \frac{\partial \tau_{yzm}}{\partial y} \delta x \delta y \delta z = \tau_{yzm} \frac{\partial u_{zm}}{\partial y} \delta x \delta y \delta z \quad (199)$$

the component of viscous stress  $\tau_{zzm}$  is

$$\tau_{zzm} = -\mu \dot{\gamma}_{zzm} = -2\mu \left( \frac{\partial u_{zm}}{\partial z} \right) \quad (200)$$

the internal energy balance in the fluid element is then shown

$$\begin{aligned} & \rho_m c_{pm} \frac{\partial(\delta x \delta y T_m)}{\partial t} \delta z \\ & = -c_{pm} \frac{\partial(\rho_m u_{zm} T_m \delta x \delta y)}{\partial z} \delta z - \frac{\partial(q_{zym} \delta x \delta y)}{\partial z} \delta z \\ & \quad - \tau_{zzm} \frac{\partial(u_{zm} \delta x \delta y)}{\partial z} \delta z - \tau_{yzm} \frac{\partial u_{zm}}{\partial y} \delta x \delta y \delta z \end{aligned} \quad (201)$$

replacing Equations (153) and (200) in (201) (with  $u_{ym}$  being neglected), substituting  $\delta x \delta y$  with  $A_{cm}$  and  $\dot{m}_m = \rho_m A_{cm} u_{zm}$ , results in the following expression

$$\begin{aligned}
\rho_m C_{p_m} \frac{\partial(A_{c_m} T_m)}{\partial t} &= -C_{p_m} \frac{\partial(\dot{m}_m T_m)}{\partial z} - \frac{\partial(q_{zy_m} A_{c_m})}{\partial z} + 2\mu \left( \frac{\partial u_{z_m}}{\partial z} \right) \frac{\partial(u_{z_m} A_{c_m})}{\partial z} \\
&+ A_{c_m} \mu \left( \frac{\partial u_{z_m}}{\partial y} \right)^2
\end{aligned} \tag{202}$$

approximating  $\frac{\partial u_{z_m}}{\partial y} \approx \langle \frac{\partial u_{z_m}}{\partial y} \rangle_{[0,h]}$ , and differentiating and rearranging Equation (202), we obtain

$$\begin{aligned}
\rho_m C_{p_m} A_{c_m} \frac{\partial T_m}{\partial t} + \rho_m C_{p_m} T_m \frac{\partial A_{c_m}}{\partial t} &= -C_{p_m} \dot{m}_m \frac{\partial T_m}{\partial z} - C_{p_m} T_m \frac{\partial \dot{m}_m}{\partial z} - A_{c_m} \frac{q_{zy_m}}{\partial z} \Big|_0^{dz} - q_{zy_m} \Big|_0^{dz} \frac{\partial A_{c_m}}{\partial z} \\
&+ 2\mu A_{c_m} \left( \frac{\partial u_{z_m}}{\partial z} \right)^2 + 2\mu u_{z_m} \frac{\partial u_{z_m}}{\partial z} \frac{\partial A_{c_m}}{\partial z} + \mu A_{c_m} \left( \langle \frac{\partial u_{z_m}}{\partial y} \rangle_{[0,h]} \right)^2
\end{aligned} \tag{203}$$

$$\begin{aligned}
\frac{\partial T_m}{\partial t} &= -\frac{T_m}{A_{c_m}} \frac{\partial A_{c_m}}{\partial t} - \frac{\dot{m}_m}{\rho_m A_{c_m}} \frac{\partial T_m}{\partial z} - \frac{T_m}{\rho_m A_{c_m}} \frac{\partial \dot{m}_m}{\partial z} - \frac{1}{\rho_m C_{p_m}} \frac{q_{zy_m}}{\partial z} \Big|_0^{dz} \\
&- \frac{1}{\rho_m C_{p_m} A_{c_m}} q_{zy_m} \Big|_0^{dz} \frac{\partial A_{c_m}}{\partial z} + 2 \frac{\mu}{\rho_m C_{p_m}} \left( \frac{\partial u_{z_m}}{\partial z} \right)^2 \\
&+ 2 \frac{\mu u_{z_m}}{\rho_m C_{p_m} A_{c_m}} \frac{\partial u_{z_m}}{\partial z} \frac{\partial A_{c_m}}{\partial z} + \frac{\mu}{\rho_m C_{p_m}} \left( \langle \frac{\partial u_{z_m}}{\partial y} \rangle_{[0,h]} \right)^2
\end{aligned} \tag{204}$$

the unit analysis of Equation (204) is as follows

$$\begin{aligned}
\left[ \frac{K}{s} \right] &= -\frac{[K]}{[m^2]} \left[ \frac{m^2}{t} \right] - \left[ \frac{kg}{s} \right] \left[ \frac{m^3}{kg} \right] \frac{1}{[m^2]} \left[ \frac{K}{m} \right] - \frac{[K]}{[m^2]} \left[ \frac{m^3}{kg} \right] \left[ \frac{kg}{s m} \right] \\
&- \left[ \frac{m^3}{kg} \right] \left[ \frac{kg K}{J} \right] \left[ \frac{m^2}{m^3} \right] \left[ \frac{J}{s m^2 K} \right] [K] \\
&- \left[ \frac{m^3}{kg} \right] \left[ \frac{kg K}{J} \right] \frac{1}{[m^2]} \left[ \frac{J}{s m^2 K} \right] [K] \left[ \frac{m^2}{m} \right] \\
&+ \left[ \frac{kg}{m s} \right] \left[ \frac{m^3}{kg} \right] \left[ \frac{K s^2}{m^2} \right] \left[ \frac{m^2}{s^2 m^2} \right] \\
&+ \left[ \frac{kg}{m s} \right] \left[ \frac{m}{s} \right] \left[ \frac{m^3}{kg} \right] \left[ \frac{K s^2}{m^2} \right] \frac{1}{[m^2]} \left[ \frac{m}{s m} \right] \left[ \frac{m^2}{m} \right] \\
&+ \left[ \frac{kg}{m s} \right] \left[ \frac{m^3}{kg} \right] \left[ \frac{K s^2}{m^2} \right] \left[ \frac{m^2}{s^2 m^2} \right]
\end{aligned} \tag{205}$$

$$\left[\frac{K}{s}\right] = -\left[\frac{K}{s}\right] - \left[\frac{K}{s}\right] - \left[\frac{K}{s}\right] - \left[\frac{K}{s}\right] - \left[\frac{K}{s}\right] + \left[\frac{K}{s}\right] + \left[\frac{K}{s}\right] + \left[\frac{K}{s}\right] \quad (206)$$

## PS<sub>v</sub> - Melt Conveying Zone

The physical properties of the melt in the melt conveying zone, such as specific heat capacity  $C_{p_m}$ , solid density  $\rho_m$  and overall heat transfer coefficient from the barrel to the melt  $U_m$ , are constant. The balances in the fluid element are developed based on these assumptions.

**Continuity Equation:** the flow area does not change with  $t$ ; therefore, the accumulation term of the fluid component is

$$\frac{\partial(\rho_m \delta x \delta y \delta z)}{\partial t} = 0 \quad (207)$$

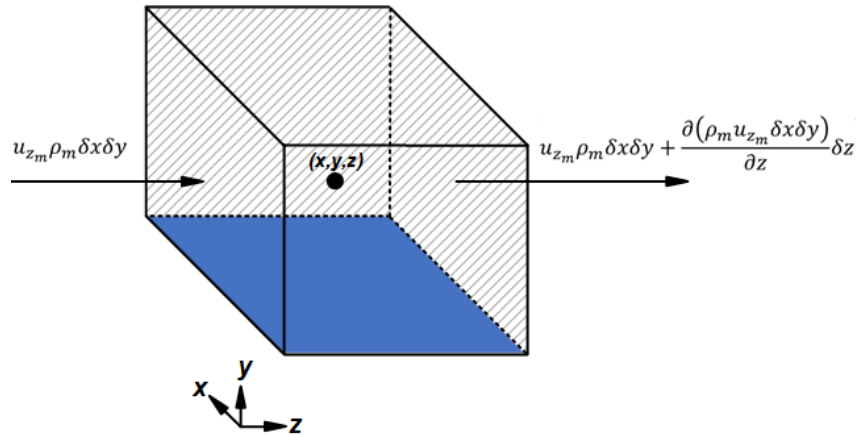


Figure 34. Continuity equation in and out of the fluid element for melt in the melt conveying zone.

The convective term is given by the product of the melt density  $\rho_m$  and the component of the velocity  $u_{z_m}$  normal to the face. Figure 34 shows that the net mass flow into the element through its boundaries is given by:

$$u_{z_m} \rho_m \delta x \delta y - \left( u_{z_m} \rho_m \delta x \delta y + \frac{\partial(\rho_m u_{z_m} \delta x \delta y)}{\partial z} \delta z \right) = - \frac{\partial(\rho_m u_{z_m} \delta x \delta y)}{\partial z} \delta z \quad (208)$$

the continuity equation in the fluid element is then shown

$$\frac{\partial(\rho_m u_{zm} \delta x \delta y)}{\partial z} \delta z = 0 \quad (209)$$

substituting  $\delta x \delta y$  with  $A_c$ , it results in

$$\frac{\partial \dot{m}_m}{\partial z} = 0 \quad (210)$$

**Momentum Balance:** the transient momentum transport in the mass direction dissipates before any substantial change in the location of the material occurs. The accumulation term of the fluid component is given by

$$\frac{\partial(\delta x \delta y \delta z \rho_m u_{zm})}{\partial t} = 0 \quad (211)$$

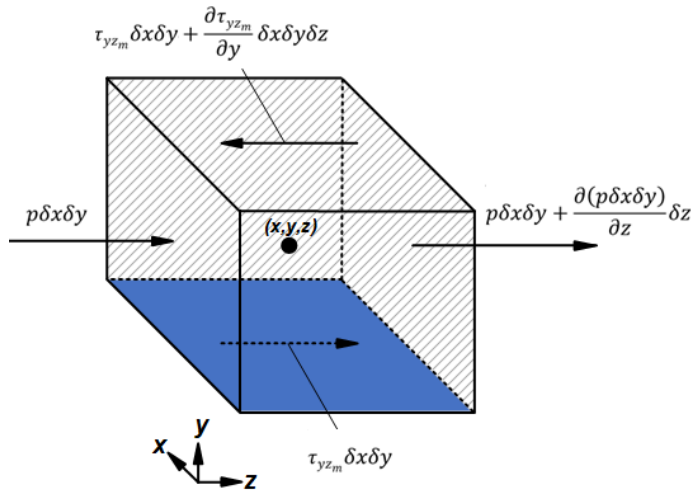


Figure 35. Momentum balance in and out of the fluid element for melt in the melt conveying zone.

It is assumed that  $\frac{\partial u_{zm}}{\partial y} \gg \frac{\partial u_{zm}}{\partial z}$ . In Figure 35 components in the  $z$ -direction of forces due to pressure  $p$  and the stress component  $\tau_{yzm}$  are considered. The magnitude of a force resulting from surface stress is calculated by multiplying the stress by the area. Forces aligned with the direction of a coordinate axis are considered positive, while those in the opposite direction are considered negative. The net force in the  $x$ -direction is the sum of the force components acting in that direction on the fluid element.

$$p \delta x \delta y - \left( p \delta x \delta y + \frac{\partial(p \delta x \delta y)}{\partial z} \delta z \right) = - \frac{\partial(p \delta x \delta y)}{\partial z} \delta z \quad (212)$$

$$-\tau_{yzm} \delta x \delta y + \left( \tau_{yzm} \delta x \delta y + \frac{\partial \tau_{yzm}}{\partial y} \delta x \delta y \delta z \right) = \frac{\partial \tau_{yzm}}{\partial y} \delta x \delta y \delta z \quad (213)$$

$u_{ym}$  is not taken into account. The momentum balance in the fluid element is then shown

$$\frac{\partial(p \delta x \delta y)}{\partial z} \delta z = \frac{\partial \tau_{yzm}}{\partial y} \delta x \delta y \delta z \quad (214)$$

replacing Equation (153) into Equation (214) and substituting  $\delta x \delta y$  with  $A_c$ , results in the following expression

$$\frac{\partial(p A_c)}{\partial z} = -\eta A_c \frac{\partial}{\partial y} \left( \frac{\partial u_{zm}}{\partial y} \right) \quad (215)$$

by differentiating and rearranging the Equation (215), we obtain

$$\mu A_c \frac{\partial^2 u_{zm}}{\partial y^2} = A_c \frac{\partial p}{\partial z} + p \frac{\partial A_c}{\partial z} \quad (216)$$

$$\frac{\partial^2 u_{zm}}{\partial y^2} = \frac{1}{\mu} \frac{\partial p}{\partial z} + \frac{p}{\mu A_c} \frac{\partial A_c}{\partial z} \quad (217)$$

the unit analysis of Equation (217) is as follows

$$\left[ \frac{1}{s \, m} \right] = \left[ \frac{s \, m}{kg} \right] \left[ \frac{kg}{m \, s^2 \, m} \right] + \left[ \frac{kg}{m \, s^2} \right] \left[ \frac{s \, m}{kg} \right] \frac{1}{[m^2]} \left[ \frac{m^2}{m} \right] \quad (218)$$

$$\left[ \frac{1}{s \, m} \right] = \left[ \frac{1}{s \, m} \right] + \left[ \frac{1}{s \, m} \right] \quad (219)$$

$\frac{\partial u_{zm}}{\partial y}$  is approximated as  $\langle \frac{\partial u_{zm}}{\partial y} \rangle_{[0,h]}$  and by integrating  $\frac{\partial^2 u_{zm}}{\partial y^2}$  twice with respect to  $y$ , we arrive at the same Equation (171), leading to the same result as Equation (177), with only  $A_{cm}$  being replaced by  $A_c$ .

$$\frac{\partial p}{\partial z} = 6 \frac{\mu u_{zs}}{h^2} - 12 \frac{\mu \langle u_{zm} \rangle}{h^2} - \frac{p}{A_c} \frac{\partial A_c}{\partial z} \quad (220)$$

**Internal Energy Balance:** for an incompressible fluid, it must be that  $C_{V_m} \approx C_{p_m}$ . The accumulation term of the fluid component is given by

$$\frac{\partial(\delta x \delta y \delta z \rho_m C_{p_m} T_m)}{\partial t} = \rho_m C_{p_m} \frac{\partial T_m}{\partial t} \delta x \delta y \delta z \quad (221)$$

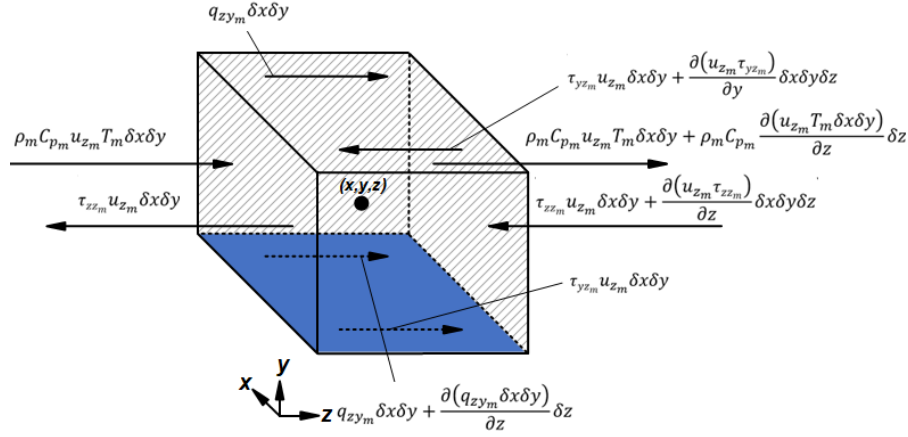


Figure 36. Internal energy balance in and out of the fluid element for the solid bed in the melting zone.

The heat transfer occurs from the  $y$ -axis but only varies in  $z$ -axis. In Figure 36, the convective term and non-convective term across its boundaries are represented by

$$\begin{aligned} & \rho_m C_{p_m} u_{z_m} T_m \delta x \delta y - \left( \rho_m C_{p_m} u_{z_m} T_m \delta x \delta y + C_{p_m} \frac{\partial(\rho_m u_{z_m} T_m \delta x \delta y)}{\partial z} \delta z \right) \\ & = -C_{p_m} \frac{\partial(\rho_m u_{z_m} T_m \delta x \delta y)}{\partial z} \delta z \end{aligned} \quad (222)$$

$$-q_{zy_m} \delta x \delta y - \left[ - \left( q_{zy_m} \delta x \delta y - \frac{\partial(q_{zy_m} \delta x \delta y)}{\partial z} \delta z \right) \right] = - \frac{\partial(q_{zy_m} \delta x \delta y)}{\partial z} \delta z \quad (223)$$

the non-convective energy term or heat transfer term, is expressed as

$$\frac{q_{zy_m}}{\partial z} \Big|_0^z = - \frac{A_T U_m}{V_T} (T_b - T_m) \quad (224)$$

$$q_{zy_m}|_0^{dz} = -U_m(T_b - T_m) \quad (225)$$

the viscous dissipation terms for the energy balance are given for Equations (198) and (199). The internal energy balance in the fluid element is then shown

$$\begin{aligned} \rho_m C_{p_m} \frac{\partial T_m}{\partial t} \delta x \delta y \delta z &= -C_{p_m} \frac{\partial(\rho_m u_{z_m} T_m \delta x \delta y)}{\partial z} \delta z - \frac{\partial(q_{zy_m} \delta x \delta y)}{\partial z} \delta z \\ &\quad - \tau_{zz_m} \frac{\partial(u_{z_m} \delta x \delta y)}{\partial z} \delta z - \tau_{yz_m} \frac{\partial u_{z_m}}{\partial y} \delta x \delta y \delta z \end{aligned} \quad (226)$$

replacing the Equations (153) and (200) into Equation (226) (with  $u_{y_m}$  being neglected), substituting  $\delta x \delta y$  with  $A_c$  and  $\dot{m}_m = \rho_m A_c u_{z_m}$ , results in the following expression

$$\begin{aligned} \rho_m C_{p_m} A_c \frac{\partial T_m}{\partial t} &= -C_{p_m} \frac{\partial(\dot{m}_m T_m)}{\partial z} - \frac{\partial(q_{zy_m} A_c)}{\partial z} + 2\mu \left( \frac{\partial u_{z_m}}{\partial z} \right) \frac{\partial(u_{z_m} A_c)}{\partial z} \\ &\quad + A_c \mu \left( \frac{\partial u_{z_m}}{\partial y} \right) \frac{\partial u_{z_m}}{\partial y} \end{aligned} \quad (227)$$

approximating  $\frac{\partial u_{z_m}}{\partial y} \approx \langle \frac{\partial u_{z_m}}{\partial y} \rangle_{[0,h]}$ , and differentiating and rearranging the Equation (227), we obtain

$$\begin{aligned} \rho_m C_{p_m} A_c \frac{\partial T_m}{\partial t} &= -C_{p_m} T_m \frac{\partial \dot{m}_m}{\partial z} - \dot{m}_m C_{p_m} \frac{\partial T_m}{\partial z} - A_c \frac{q_{zy_m}}{\partial z} \Big|_0^{dz} - q_{zy_m} \Big|_0^{dz} \frac{\partial A_c}{\partial z} \\ &\quad + 2\mu A_c \left( \frac{\partial u_{z_m}}{\partial z} \right)^2 + 2\mu u_{z_m} \frac{\partial u_{z_m}}{\partial z} \frac{\partial A_c}{\partial z} + \mu A_c \left( \langle \frac{\partial u_{z_m}}{\partial y} \rangle_{[0,h]} \right)^2 \end{aligned} \quad (228)$$

$$\begin{aligned} \frac{\partial T_m}{\partial t} &= -\frac{T_m}{\rho_m A_c} \frac{\partial \dot{m}_m}{\partial z} - \frac{\dot{m}_m}{\rho_m A_c} \frac{\partial T_m}{\partial z} - \frac{1}{\rho_m C_{p_m}} \frac{q_{zy_m}}{\partial z} \Big|_0^{dz} \\ &\quad - \frac{1}{\rho_m C_{p_m} A_c} q_{zy_m} \Big|_0^{dz} \frac{\partial A_c}{\partial z} + 2 \frac{\mu}{\rho_m C_{p_m}} \left( \frac{\partial u_{z_m}}{\partial z} \right)^2 \\ &\quad + 2 \frac{\mu u_{z_m}}{\rho_m C_{p_m} A_c} \frac{\partial u_{z_m}}{\partial z} \frac{\partial A_c}{\partial z} + \frac{\mu}{\rho_m C_{p_m}} \left( \langle \frac{\partial u_{z_m}}{\partial y} \rangle_{[0,h]} \right)^2 \end{aligned} \quad (229)$$

$\frac{\partial u_{z_m}}{\partial z}$  is given by Equation (182), with only  $A_{c_m}$  being replaced by  $A_c$

$$\frac{\partial u_{zm}}{\partial z} = \frac{1}{\rho_m A_c} \frac{\partial \dot{m}_m}{\partial z} - \frac{\dot{m}_m}{\rho_m A_c^2} \frac{\partial A_c}{\partial z} \quad (230)$$

the unit analysis of Equation (203) is as follows

$$\begin{aligned} \left[ \frac{K}{s} \right] &= - \left[ \frac{m^3}{kg} \right] \left[ \frac{K}{m^2} \right] \left[ \frac{kg}{s m} \right] - \left[ \frac{kg}{s} \right] \left[ \frac{m^3}{kg} \right] \left[ \frac{1}{m^2} \right] \left[ \frac{K}{m} \right] \\ &\quad - \left[ \frac{m^3}{kg} \right] \left[ \frac{kg K}{J} \right] \left[ \frac{m^2}{m^3} \right] \left[ \frac{J}{s m^2 K} \right] [K] \\ &\quad - \left[ \frac{m^3}{kg} \right] \left[ \frac{kg K}{J} \right] \left[ \frac{1}{m^2} \right] \left[ \frac{J}{s m^2 K} \right] [K] \left[ \frac{m^2}{m} \right] \\ &\quad + \left[ \frac{kg}{m s} \right] \left[ \frac{m^3}{kg} \right] \left[ \frac{K s^2}{m^2} \right] \left[ \frac{m^2}{s^2 m^2} \right] \\ &\quad + \left[ \frac{kg}{m s} \right] \left[ \frac{m}{s} \right] \left[ \frac{m^3}{kg} \right] \left[ \frac{K s^2}{m^2} \right] \left[ \frac{1}{m^2} \right] \left[ \frac{m}{s m} \right] \left[ \frac{m^2}{m} \right] \\ &\quad + \left[ \frac{kg}{m s} \right] \left[ \frac{m^3}{kg} \right] \left[ \frac{K s^2}{m^2} \right] \left[ \frac{m^2}{s^2 m^2} \right] \end{aligned} \quad (231)$$

$$\left[ \frac{K}{s} \right] = - \left[ \frac{K}{s} \right] - \left[ \frac{K}{s} \right] - \left[ \frac{K}{s} \right] - \left[ \frac{K}{s} \right] + \left[ \frac{K}{s} \right] + \left[ \frac{K}{s} \right] + \left[ \frac{K}{s} \right] \quad (232)$$

## PS<sub>v1</sub> - Melt Flow in the Die

For the melt flow zone in the die, it is modeled as a whole, and therefore, macroscopic models are applied. The physical properties are considered constant. The balances are developed based on these assumptions.

**Continuity Equation:** it is assumed that the melt mass flow rate at the inlet ( $\dot{m}_{m_{in}}$ ) is equal to that at the outlet ( $\dot{m}_{m_{out}}$ ), as shown in Equation

$$\dot{m}_{m_{in}} = \dot{m}_{m_{out}} = \dot{m}_m \quad (233)$$

**Momentum Balance:** the relationship between mass flow rate and pressure drop through the geometry is shown in Equation (234). In this case, a geometric factor  $K_D$  is defined, capturing the shape and dimensions of the die.

$$\dot{m}_m = K_D \rho_m \frac{\Delta p}{\eta} \quad (234)$$

## References

- Abdel-Ghany, W. E., Ebeid, S. J., & Fikry, I. (2015). Effect of Geometry and Rotational Speed on the Axial Pressure Profile of a Single Screw Extrusion. *IJISSET-International Journal of Innovative Science, Engineering & Technology*, 2, 82–88.
- Abdi, H., & Williams, L. J. (2010). Principal component analysis. In *Wiley Interdisciplinary Reviews: Computational Statistics* (Vol. 2, Issue 4, pp. 433–459). <https://doi.org/10.1002/wics.101>
- Abeykoon, C. (2014). A novel model-based controller for polymer extrusion. *IEEE Transactions on Fuzzy Systems*, 22(6), 1413–1430. <https://doi.org/10.1109/TFUZZ.2013.2293348>
- Abeykoon, C. (2016). Single screw extrusion control: A comprehensive review and directions for improvements. *Control Engineering Practice*, 51, 69–80. <https://doi.org/10.1016/j.conengprac.2016.03.008>
- Abeykoon, C., Li, K., Martin, P. J., & Kelly, A. L. (2011). Modelling of melt pressure development in polymer extrusion: Effects of process settings and screw geometry. *Proceedings of 2011 International Conference on Modelling, Identification and Control, ICMIC 2011*, 197–202. <https://doi.org/10.1109/icmic.2011.5973700>
- Abeykoon, C., Li, K., McAfee, M., Martin, P. J., & Irwin, G. W. (2011). Extruder melt temperature control with fuzzy logic. *IFAC Proceedings Volumes (IFAC-PapersOnline)*, 44(1 PART 1), 8577–8582. <https://doi.org/10.3182/20110828-6-IT-1002.01576>
- Abeykoon, C., Li, K., McAfee, M., Martin, P. J., Niu, Q., Kelly, A. L., & Deng, J. (2011). A new model based approach for the prediction and optimisation of thermal homogeneity in single screw extrusion. *Control Engineering Practice*, 19(8), 862–874. <https://doi.org/10.1016/j.conengprac.2011.04.015>
- Abeykoon, C., McAfee, M., Li, K., Martin, P. J., Deng, J., & Kelly, A. L. (2010). *Modelling the Effects of Operating Conditions on Motor Power Consumption in Single Screw Extrusion* (pp. 9–20). [https://doi.org/10.1007/978-3-642-15597-0\\_57](https://doi.org/10.1007/978-3-642-15597-0_57)
- Abeykoon, C., McMillan, A., & Nguyen, B. K. (2021). Energy efficiency in extrusion-related polymer processing: A review of state of the art and potential efficiency

- improvements. In *Renewable and Sustainable Energy Reviews* (Vol. 147). Elsevier Ltd. <https://doi.org/10.1016/j.rser.2021.111219>
- Abeykoon, C., Pérez, P., & Kelly, A. L. (2020). The effect of materials' rheology on process energy consumption and melt thermal quality in polymer extrusion. *Polymer Engineering and Science*, 60(6), 1244–1265. <https://doi.org/10.1002/pen.25377>
- Adesanya, A., Abdulkareem, A., & Adesina, L. M. (2020). Predicting extrusion process parameters in Nigeria cable manufacturing industry using artificial neural network. *Heliyon*, 6(7). <https://doi.org/10.1016/j.heliyon.2020.e04289>
- Alvarez, H., Lamanna, R., Vega, P., & Revollar, S. (2009). Metodología para la obtención de modelos semifísicos de base fenomenológica aplicada a una sulfitoradora de jugo de caña de azúcar. *RIAI - Revista Iberoamericana de Automatica e Informatica Industrial*, 6(3), 10–20. [https://doi.org/10.1016/S1697-7912\(09\)70260-2](https://doi.org/10.1016/S1697-7912(09)70260-2)
- ASTM. (2021). *Standard Test Method for Transition Temperatures and Enthalpies of Fusion and Crystallization of Polymers by Differential Scanning Calorimetry (ASTM D3418-21)*. American Society for Testing and Materials. <https://store.astm.org/d3418-21.html>
- Benardos, P. G., & Vosniakos, G. C. (2007). Optimizing feedforward artificial neural network architecture. *Engineering Applications of Artificial Intelligence*, 20(3), 365–382. <https://doi.org/10.1016/j.engappai.2006.06.005>
- Bilski, J., & Wilamowski, B. M. (2017). Parallel Levenberg-Marquardt Algorithm Without Error Backpropagation. *Springer International Publishing ICAISC 2017, Part I, LNAI, 10245*, 25–39. <https://doi.org/10.1007/978-3-319-59063-9>
- Buchaniec, S., Gnatowski, M., & Brus, G. (2021). Integration of classical mathematical modeling with an artificial neural network for the problems with limited dataset. *Energies*, 14(16). <https://doi.org/10.3390/en14165127>
- Burbidge, A., & Bridgwater, J. (1995). The single screw extrusion of pastes. *Chemical Engineering Science*, 50, 2531–2543.
- Cai, S., Wang, Z., Wang, S., Perdikaris, P., & Karniadakis, G. E. (2021). Physics-informed neural networks for heat transfer problems. *Journal of Heat Transfer*, 143(6). <https://doi.org/10.1115/1.4050542>
- Campbell, G. A., Wetzel, M. D., & Spalding, M. A. (2022). A proposed mechanism for solid bed encapsulation: Based on comparing three dimensional and one-dimensional screw melting models. *Polymer Engineering and Science*, 62(10), 3377–3389. <https://doi.org/10.1002/pen.26110>
- Carson, J. S. (2005). Introduction to modeling and simulation. *Proceedings of the Winter Simulation Conference, 2005.*, 8 pp.-. <https://doi.org/10.1109/WSC.2005.1574235>

- Chiu, S.-H., & Pong, S.-H. (2000). In-line Viscosity Fuzzy Control. *Journal of Applied Polymer Science*, 9(7), 1249–1255. [https://doi.org/10.1002/1097-4628\(20010214\)79:7<1249::AID-APP120>3.0.CO;2-9](https://doi.org/10.1002/1097-4628(20010214)79:7<1249::AID-APP120>3.0.CO;2-9)
- Costin, M. H., Taylor, P. A., & Wright, J. D. (1982). On the Dynamics and Control of a Plasticating Extruder. *POLYMER ENGINEERING AND SCIENCE*, 22(17).
- Cubeta, U., Bhattacharya, D., & Sadtchenko, V. (2017). Melting of superheated molecular crystals. *Journal of Chemical Physics*, 147(1). <https://doi.org/10.1063/1.4985663>
- Cunha, A. G., Covas, J. A., & Ohveira, P. (1998). Optimization of polymer extrusion with genetic algorithms. *IMA Journal of Mathematics Applied in Business & Industry*, 9, 267–277. <https://doi.org/10.1093/imaman/9.3.267>
- David, M., Alvarez, H., Ocampo-Martinez, C., & Sánchez-Peña, R. (2020). Dynamic modelling of alkaline self-pressurized electrolyzers: a phenomenological-based semiphysical approach. *International Journal of Hydrogen Energy*, 45(43), 22394–22407. <https://doi.org/10.1016/j.ijhydene.2020.06.038>
- De Tommaso, J., Rossi, F., Moradi, N., Pirola, C., Patience, G. S., & Galli, F. (2020). Experimental methods in chemical engineering: Process simulation. In *Canadian Journal of Chemical Engineering* (Vol. 98, Issue 11, pp. 2301–2320). Wiley-Liss Inc. <https://doi.org/10.1002/cjce.23857>
- Denysiuk, R., Recio, G., Covas, J. A., & Gaspar-Cunha, A. (2018). Using multiobjective optimization algorithms and decision making support to solve polymer extrusion problems. *Polymer Engineering and Science*, 58(4), 493–502. <https://doi.org/10.1002/pen.24732>
- Diagne, M., Shang, P., & Wang, Z. (2016a). Feedback Stabilization for the Mass Balance Equations of an Extrusion Process. *IEEE Transactions on Automatic Control*, 61(3), 760–765. <https://doi.org/10.1109/TAC.2015.2444232>
- Diagne, M., Shang, P., & Wang, Z. (2016b). Well-posedness and exact controllability of the mass balance equations for an extrusion process. *Mathematical Methods in the Applied Sciences*, 39(10), 2659–2670. <https://doi.org/10.1002/mma.3719>
- Drabek, J., Zatloukal, M., & Martyn, M. (2018). Effect of molecular weight on secondary Newtonian plateau at high shear rates for linear isotactic melt blown polypropylenes. *Journal of Non-Newtonian Fluid Mechanics*, 251, 107–118. <https://doi.org/10.1016/j.jnnfm.2017.11.009>
- Dyadichev, V. V., Kolesnikov, A. V., Menyuk, S. G., & Dyadichev, A. V. (2019). Improvement of extrusion equipment and technologies for processing secondary combined polymer materials and mixtures. *Journal of Physics: Conference Series*, 1210(1). <https://doi.org/10.1088/1742-6596/1210/1/012035>

- EL, M. Tency., & M, H. (2024). Applications of Fuzzy Logics in Modern Systems: A Simple Survey. *International Journal of Research Publication and Reviews*, 5(5), 7598–7600. <https://doi.org/10.55248/gengpi.5.0524.1316>
- Esenttia. (2021). *05H82-AV - Esenttia S.A.*  
[https://www.esenttia.co/zp/api/webroot/productos/BT\\_Espanol/BT\\_ES\\_05H82-AV.pdf](https://www.esenttia.co/zp/api/webroot/productos/BT_Espanol/BT_ES_05H82-AV.pdf)
- Estrada, O., & Janna, F. C. (2022). A novel melting model for polymer extrusion: Mechanically induced transition layer removal. *Polymer Engineering and Science*, 62(10), 3290–3309. <https://doi.org/10.1002/pen.26104>
- Estrada, O., Ortiz, J. C., Hernández, A., López, I., Chejne, F., & del Pilar Noriega, M. (2020). Experimental study of energy performance of grooved feed and grooved plasticating single screw extrusion processes in terms of SEC, theoretical maximum energy efficiency and relative energy efficiency. *Energy*, 194. <https://doi.org/10.1016/j.energy.2019.116879>
- Faegh, M., Ghungrad, S., Oliveira, J. P., Rao, P., & Haghghi, A. (2025). A review on physics-informed machine learning for process-structure-property modeling in additive manufacturing. *Journal of Manufacturing Processes*, 133, 524–555. <https://doi.org/10.1016/j.jmapro.2024.11.066>
- Fayose, F. T., & Huan, Z. (2014). Specific mechanical energy requirement of a locally developed extruder for selected starchy crops. *Food Science and Technology Research*, 20(4), 793–798. <https://doi.org/10.3136/fstr.20.793>
- Feng, S., Zhou, H., & Dong, H. (2019). Using deep neural network with small dataset to predict material defects. *Materials and Design*, 162, 300–310. <https://doi.org/10.1016/j.matdes.2018.11.060>
- Flumerfelt, R. W., Pierick, M. W., Cooper, S. L., & Bird, R. B. (1969). Generalized Plane Couette Flow of a Non-Newtonian Fluid. *Industrial & Engineering Chemistry Fundamentals*, 8(2). <https://doi.org/10.1021/i160030a028>
- Gaspar-Cunha, A., & Covas, J. A. (2004). Reduced Pareto Set Genetic Algorithm: Application to Polymer Extrusion. *Metaheuristics for Multiobjective Optimisation*, 221–249. [https://doi.org/10.1007/978-3-642-17144-4\\_](https://doi.org/10.1007/978-3-642-17144-4_)
- Golpour Kandeh, S., Ramazani Khorshid Doost, R., Doost, K., & Kabaranzadeh Ghadim, M. (2022). Design of a fault detection expert system to diagnose errors in the Polypropylene production process. *Journal of Industrial and Systems Engineering*, 14(3), 237–258.
- Greene, J. P. (2021). 3 - Microstructures of Polymers. In J. P. Greene (Ed.), *Automotive Plastics and Composites* (pp. 27–37). William Andrew Publishing. <https://doi.org/https://doi.org/10.1016/B978-0-12-818008-2.00009-X>

- Grimard, J., Dewasme, L., & Wouwer, A. Vande. (2016). A review of dynamic models of Hot-melt extrusion. In *Processes* (Vol. 4, Issue 2). MDPI AG. <https://doi.org/10.3390/pr4020019>
- Guerrero, C., & Carreau, P. J. (1993). A MATHEMATICAL MODEL FOR PREDICTING THE DYNAMIC TEMPERATURE BEHAVIOR OF A SINGLE-SCREW PLASTICATING EXTRUDER. *Journal of Polymer Engineering*, 12(3), 155–177.
- Guo, P., Ni, X., & Zheng, J. (1993). Polymer Extrusion Production Control Using Active Recognition and Adaptive Control System. *[Proceedings 1993] Second IEEE International Conference on Fuzzy Systems*, 779–784. <https://doi.org/10.1109/FUZZY.1993.327541>
- Herzog, D., Roland, W., Marschik, C., & Berger-Weber, G. R. (2024). Generalized predictions of the pumping characteristics and viscous dissipation of single-screw extruders including three-dimensional curvature effects. *Polymer Engineering & Science*, 64(11), 5566–5587. <https://doi.org/10.1002/pen.26934>
- Hosain, M. L., & Fdhila, R. B. (2015). Literature Review of Accelerated CFD Simulation Methods towards Online Application. *Energy Procedia*, 75, 3307–3314. <https://doi.org/10.1016/j.egypro.2015.07.714>
- Hyvärinen, M., Jabeen, R., & Kärki, T. (2020). The modelling of extrusion processes for polymers-A review. In *Polymers* (Vol. 12, Issue 6). MDPI AG. <https://doi.org/10.3390/polym12061306>
- Ibrahim, D. (2016). An Overview of Soft Computing. *Procedia Computer Science*, 102, 34–38. <https://doi.org/10.1016/j.procs.2016.09.366>
- ISO. (2019). Plastics — Methods for determining the density of non-cellular plastics — Part 1: Immersion method, liquid pycnometer method and titration method (ISO 1183-1:2019). In *International Organization for Standardization* (Vol. 3). 3. <https://www.iso.org/standard/74990.html>
- Janiesch, C., Zschech, P., & Heinrich, K. (2021). Machine learning and deep learning. *Electronic Markets*, 31(3), 685–695. <https://doi.org/10.1007/s12525-021-00475-2>
- Janjanam, D., Ganesh, B., & Manjunatha, L. (2021). Design of an expert system architecture: An overview. *Journal of Physics: Conference Series*, 1767(1). <https://doi.org/10.1088/1742-6596/1767/1/012036>
- Jiang, Z., Yang, Y., Mo, S., Yao, K., & Gao, F. (2012). Polymer extrusion: From control system design to product quality. *Industrial and Engineering Chemistry Research*, 51(45), 14759–14770. <https://doi.org/10.1021/ie301036c>
- Jolliffe, I. T., & Cadima, J. (2016). Principal component analysis: A review and recent developments. In *Philosophical Transactions of the Royal Society A: Mathematical,*

- Physical and Engineering Sciences* (Vol. 374, Issue 2065). Royal Society of London.  
<https://doi.org/10.1098/rsta.2015.0202>
- Kacir, L., & Tadmor, Z. (1972). Solids Conveying in Screw Extruders Part 111: The Delay Zone". *Polymer Engineering and Science*, 12, 387–395.  
<https://doi.org/https://doi.org/10.1002/pen.760120511>
- Kadyirov, A., Gataullin, R., & Karaeva, J. (2019). Numerical simulation of polymer solutions in a single-screw extruder. *Applied Sciences (Switzerland)*, 9(24).  
<https://doi.org/10.3390/app9245423>
- Kamble, A. J., & Rewaskar, R. P. (2020). Soft computing - Fuzzy Logic: An overview. *International Journal of Fuzzy Mathematical Archive*, 18(01), 45–52.  
<https://doi.org/10.22457/ijfma.v18n1a06214>
- Kelly, A. L., Brown, E. G., & Coates, P. D. (2006). The effect of screw geometry on melt temperature profile in single screw extrusion. *Polymer Engineering and Science*, 46(12), 1706–1714. <https://doi.org/10.1002/pen.20657>
- Kent, R. (2018). Targeting and controlling energy costs. In *Energy Management in Plastics Processing (Third Edition)* (Third Edition, pp. 79–104). Elsevier.  
<https://doi.org/10.1016/B978-0-08-102507-9.50003-9>
- Kim, D. J., Kim, S. II, & Kim, H. S. (2022). Thermal simulation trained deep neural networks for fast and accurate prediction of thermal distribution and heat losses of building structures. *Applied Thermal Engineering*, 202.  
<https://doi.org/10.1016/j.applthermaleng.2021.117908>
- Kroesser, F. W., & Middleman, S. (1965). The Calculation of Screw Characteristics for the Extrusion of non-Newtonian Melts. *Polymer Engineering and Science*, 5(4), 230–234. <https://doi.org/10.1002/pen.760050405>
- Lai, E., & Wen, D. (2000). Modeling of the Plasticating Process in a Single-Screw Extruder: A Fast-Track Approach. *POLYMER ENGINEERING AND SCIENCE*, 40(5), 1074–1084.
- Lambora, A., Gupta, K., & Chop, K. (2019). Genetic Algorithm- A Literature Review. 2019 *International Conference on Machine Learning, Big Data, Cloud and Parallel Computing (COMITCon)*, 380–384. <https://doi.org/0.1109/COMITCon.2019.8862255>
- Lanyi, F. J., Wenzke, N., Kaschta, J., & Schubert, D. W. (2020). On the Determination of the Enthalpy of Fusion of  $\alpha$ -Crystalline Isotactic Polypropylene Using Differential Scanning Calorimetry, X-Ray Diffraction, and Fourier-Transform Infrared Spectroscopy: An Old Story Revisited. *Advanced Engineering Materials*, 22(9).  
<https://doi.org/10.1002/adem.201900796>

- Lema, L., Garcia-Tirado, J., Builes-Montaño, C., & Alvarez, H. (2019). Phenomenological-Based model of human stomach and its role in glucose metabolism. *Journal of Theoretical Biology*, *460*, 88–100. <https://doi.org/10.1016/j.jtbi.2018.10.024>
- Liao, S. H. (2005). Expert system methodologies and applications-a decade review from 1995 to 2004. *Expert Systems with Applications*, *28*(1), 93–103. <https://doi.org/10.1016/j.eswa.2004.08.003>
- Lippits, D. R., Rastogi, S., & Höhne, G. W. H. (2006). Melting kinetics in polymers. *Physical Review Letters*, *96*(21). <https://doi.org/10.1103/PhysRevLett.96.218303>
- Long, Z., Lu, Y., Ma, X., & Dong, B. (2018). PDE-Net: Learning PDEs from Data. In *International conference on machine learning* (pp. 3208–3216). PMLR.
- Lovegrove, J. G. A., & Williams, J. G. (1973). SOLIDS CONVEYING IN A SINGLE EXTRUDER; THE ROLE OF GRAVITY SCREW FORCES. *Journal Mechanical Engineering Science*, *15*(2), 114–122. [https://doi.org/10.1243/JMES\\_JOUR\\_1973\\_015\\_021\\_02](https://doi.org/10.1243/JMES_JOUR_1973_015_021_02)
- Maffezzoli, A. M., Kenny, J. M., Nicolais, L., & others. (1989). Welding of PEEK/carbon fiber composite laminates. *SAMPE Journal*, *25*, 35–39.
- Marschik, C., Roland, W., & Osswald, T. A. (2022). Melt Conveying in Single-Screw Extruders: Modeling and Simulation. In *Polymers* (Vol. 14, Issue 5). MDPI. <https://doi.org/10.3390/polym14050875>
- McAfee, M., & Thompson, S. (2007). A novel approach to dynamic modelling of polymer extrusion for improved process control. *Proceedings of the Institution of Mechanical Engineers. Part I: Journal of Systems and Control Engineering*, *221*(4), 617–628. <https://doi.org/10.1243/09596518JSCE357>
- Mckay, B., Lennox, B., Willis, M., Barton, G. W., & Montage, G. (1996). Extruder modelling: a comparison of two paradigms. *UKACC International Conference on Control '96*, *2*, 734–739. <https://doi.org/10.1049/cp:19960643>
- Mekras, N., & Artemakis, I. (2012). Using artificial neural networks to model extrusion processes for the manufacturing of polymeric micro-tubes. *IOP Conference Series: Materials Science and Engineering*, *40*(1). <https://doi.org/10.1088/1757-899X/40/1/012041>
- Mendel, J. M. (1995). Fuzzy Logic Systems for Engineering: A tutorial. *Proceedings of the IEEE*, *83*(3), 345–377. <https://doi.org/10.1109/5.364485>
- Mills, N., Jenkins, M., & Kukureka, S. (2020a). Chapter 3 - Amorphous polymers and the glass transition. In N. Mills, M. Jenkins, & S. Kukureka (Eds.), *Plastics (Fourth Edition)* (pp. 33–48). Butterworth-Heinemann. <https://doi.org/10.1016/B978-0-08-102499-7.00003-5>

- Mills, N., Jenkins, M., & Kukureka, S. (2020b). Semi-crystalline polymers. In *Plastics* (pp. 49–66). Elsevier. <https://doi.org/10.1016/B978-0-08-102499-7.00004-7>
- Nabhan, B. J., Mohammed, T. W., Al-Moameri, H. H., & Ghalib, L. (2024). The Effect of Chain Tacticity on the Thermal Energy Parameters of Isotactic and Syndiotactic Polypropylene. *Tikrit Journal of Engineering Sciences*, 31(2), 117–127. <https://doi.org/10.25130/tjes.31.2.11>
- Nädäban, S. (2022). Fuzzy Logic and Soft Computing—Dedicated to the Centenary of the Birth of Lotfi A. Zadeh (1921–2017). In *Mathematics* (Vol. 10, Issue 17). MDPI. <https://doi.org/10.3390/math10173216>
- Naghypour, A., Salehpour, A., & Iranag, B. S. (2024). Optimizing UPVC profile production using adaptive neuro-fuzzy inference system. *International Journal of Information Technology (Singapore)*. <https://doi.org/10.1007/s41870-024-02198-x>
- Nastaj, A., & Wilczyński, K. (2020). Optimization for starve fed/flood fed single screw extrusion of polymeric materials. *Polymers*, 12(1). <https://doi.org/10.3390/polym12010149>
- Nastaj, A., & Wilczyński, K. (2022). Computational Scale-Up for Flood Fed/Starve Fed Single Screw Extrusion of Polymers. *Polymers*, 14(2). <https://doi.org/10.3390/polym14020240>
- Nelson, R. W., Chan, D., Yang, B., & Lee, L. J. (1986). Dynamic Behavior of a Single Screw Plasticating Extruder Part I: Experimental Study. *POLYMER ENGINEERING AND SCIENCE*, 26(2).
- Ong, P., Ho, C. S., Chin, D. D. V. S., Sia, C. K., Ng, C. H., Wahab, M. S., & Bala, A. S. (2019). Diameter prediction and optimization of hot extrusion-synthesized polypropylene filament using statistical and soft computing techniques. *Journal of Intelligent Manufacturing*, 30(4), 1957–1972. <https://doi.org/10.1007/s10845-017-1365-8>
- Onwulata, C. I., Mulvaney, S. J., Hsieh, F., & Heymann, H. (1992). Step Changes in Screw Speed Affect Extrusion Temperature and Pressure and Extrudate Characteristics. *JOURNAL OF FOOD SCIENCE*, 57(2).
- Pachner, S., Löw-Baselli, B., Affenzeller, M., & Miethlinger, J. (2017). A Generalized 2D Output Model of Polymer Melt Flow in Single-Screw Extrusion. *International Polymer Processing*, 32(2), 209–216. <https://doi.org/doi:10.3139/217.3326>
- Patel, H., Thakkar, A., Pandya, M., & Makwana, K. (2018). Neural network with deep learning architectures. *Journal of Information and Optimization Sciences*, 39(1), 31–38. <https://doi.org/10.1080/02522667.2017.1372908>

- Perera, Y. S., Li, J., & Abeykoon, C. (2024). Adaptive Neuro-Fuzzy Controller for Real-Time Melt Pressure Control in Polymer Extrusion Processes. *2024 European Control Conference (ECC)*, 2023–2028. <https://doi.org/10.23919/ECC64448.2024.10590713>
- Perera, Y. S., Li, J., Kelly, A. L., & Abeykoon, C. (2023). *Melt Pressure Prediction in Polymer Extrusion Processes with Deep Learning*. IEEE.
- Plastics Europe. (2023). *Plastics - the fast Facts 2023*. <https://plasticseurope.org/knowledge-hub/plastics-the-fast-facts-2023/>
- Precup, R. E., & Hellendoorn, H. (2011). A survey on industrial applications of fuzzy control. *Computers in Industry*, 62(3), 213–226. <https://doi.org/10.1016/j.compind.2010.10.001>
- Presiga, N., Alvarez, H., & Hormaza, A. (2023). Phenomenological-based model of direct blue 2 adsorption on corncob in a fixed-bed. *Canadian Journal of Chemical Engineering*, 102(3), 1302–1321. <https://doi.org/10.1002/cjce.25137>
- Pricci, A., de Tullio, M. D., & Percoco, G. (2023). Modeling of extrusion-based additive manufacturing for pelletized thermoplastics: Analytical relationships between process parameters and extrusion outcomes. *CIRP Journal of Manufacturing Science and Technology*, 41, 239–258. <https://doi.org/10.1016/j.cirpj.2022.11.020>
- Raissi, M., Perdikaris, P., & Karniadakis, G. E. (2019). Physics-informed neural networks: A deep learning framework for solving forward and inverse problems involving nonlinear partial differential equations. *Journal of Computational Physics*, 378, 686–707. <https://doi.org/10.1016/j.jcp.2018.10.045>
- Rauwendaal, C. (2014). *Polymer extrusion*. Carl Hanser Verlag GmbH Co KG.
- Rauwendaal, C. (2016). Heat transfer in twin screw compounding extruders. *AIP Conference Proceedings*, 1779. <https://doi.org/10.1063/1.4965484>
- Rauwendaal, C. (2018). *Understanding Extrusion*. <https://doi.org/10.3139/9781569906996>
- Rawal, A., & Davies, P. J. (2005). Expert system for the optimisation of melt extruded net structures. *Plastics, Rubber and Composites*, 34(2), 47–53. <https://doi.org/10.1179/174328905X48513>
- Resonnek, V., & Schöppner, V. (2019). Self-optimizing barrel temperature setting control of single screw extruders for improving the melt quality. *AIP Conference Proceedings*, 2065. <https://doi.org/10.1063/1.5088268>
- Roland, W., Marschik, C., Kommenda, M., Haghofer, A., Dorl, S., & Winkler, S. (2021). Predicting the Non-Linear Conveying Behavior in Single-Screw Extrusion: A Comparison of Various Data-Based Modeling Approaches used with CFD Simulations. *International Polymer Processing*, 36(5), 529–544.

- Roland, W., & Miethlinger, J. (2018). Heuristic analysis of viscous dissipation in single-screw extrusion. *Polymer Engineering and Science*, *58*(11), 2055–2070. <https://doi.org/10.1002/pen.24817>
- Santamaría, A. (2020). Rheology and Polymers: Born to Be Friends. In F. J. Galindo-Rosales, L. Campo-Deaño, A. M. Afonso, M. A. Alves, & F. T. Pinho (Eds.), *Proceedings of the Iberian Meeting on Rheology (IBEREO 2019)* (pp. 96–99). Springer International Publishing.
- Savytskyi, O., Tymoshenko, M., Hramm, O., & Romanov, S. (2020). Application of soft sensors in the automated process control of different industries. *E3S Web of Conferences*, *166*. <https://doi.org/10.1051/e3sconf/202016605003>
- Schmitt, L. M. (2001). Theory of genetic algorithms. *Theoretical Computer Science*, *259*(1–2), 1–61. [www.elsevier.com/locate/tcsFundamentalStudy](http://www.elsevier.com/locate/tcsFundamentalStudy)
- Shaalan, A. S., El-Nagar, A. M., El-Bardini, M., & Sharaf, M. (2020). Embedded fuzzy sliding mode control for polymer extrusion process. *ISA Transactions*, *103*, 237–251. <https://doi.org/10.1016/j.isatra.2020.03.026>
- Shakeri, F., & Dehghan, M. (2008). The method of lines for solution of the one-dimensional wave equation subject to an integral conservation condition. *Computers and Mathematics with Applications*, *56*(9), 2175–2188. <https://doi.org/10.1016/j.camwa.2008.03.055>
- Singh, M. K., & Singh, A. (2022). Chapter 9 - Thermal characterization of materials using differential scanning calorimeter. In M. K. Singh & A. Singh (Eds.), *Characterization of Polymers and Fibres* (pp. 201–222). Woodhead Publishing. <https://doi.org/https://doi.org/10.1016/B978-0-12-823986-5.00006-3>
- Speranza, V., Salomone, R., & Pantani, R. (2023). Effects of Pressure and Cooling Rates on Crystallization Behavior and Morphology of Isotactic Polypropylene. *Crystals*, *13*(6). <https://doi.org/10.3390/cryst13060922>
- Stokes, V. K. (2020). Concepts from Polymer Physics. In *Introduction to Plastics Engineering* (pp. 229–245). John Wiley & Sons, Ltd. <https://doi.org/10.1002/9781119536550.ch10>
- Tadmor, Z., & Gogos, C. G. (2013). *Principles of polymer processing*. John Wiley & Sons.
- Tadmor, Z., Lipshitz, S. D., & Lavie, R. (1974). Dynamic Model of a Plasticating Extruder. *POLYMER ENGINEERING AND SCIENCE*, *14*(2), 112–119. <https://doi.org/10.1002/pen.760140206>
- Tagashira, K., Maruyama, M., Mizutani, Y., Kajioka, H., Sakai, K., Okada, K. N., & Hikosaka, M. (2019). Melting behavior and structural and morphological changes of isotactic polypropylene from heat treatment. *Polymer Journal*, *51*(2), 227–235. <https://doi.org/10.1038/s41428-018-0145-4>

- Tan, C. F., Wahidin, L. S., Khalil, S. N., Tamaldin, N., Hu, J., & Rauterberg, G. W. M. (2016). The application of expert system: a review of research and applications. *ARPN Journal of Engineering and Applied Sciences*, 11(4), 2448–2453. [www.arpnjournals.com](http://www.arpnjournals.com)
- Tan, L. P., Lotfi, A., Lai, E., & Hull, J. B. (2004). Soft computing applications in dynamic model identification of polymer extrusion process. *Applied Soft Computing Journal*, 4(4), 345–355. <https://doi.org/10.1016/j.asoc.2003.10.004>
- Taur, J. S., Tao, C. W., & Tsai, C. C. (1995). Temperature Control of a Plastic Extrusion Barrel Using PID Fuzzy Controllers. *Proceedings IEEE Conference on Industrial Automation and Control Emerging Technology Applications*, 370–375. <https://doi.org/10.1109/iacet.1995.527590>
- Tsai, C. C., & Lu, C. H. (1998). Fuzzy supervisory predictive PID control of a plastics extruder barrel. *Journal of the Chinese Institute of Engineers, Transactions of the Chinese Institute of Engineers, Series A/Chung-Kuo Kung Ch'eng Hsueh K'an*, 21(5), 619–624. <https://doi.org/10.1080/02533839.1998.9670423>
- Udoewa, V., & Kumar, V. (2012). Computational Fluid Dynamics. In *Applied Computational Fluid Dynamics*. InTech. <https://doi.org/10.5772/28614>
- van Puyvelde, P., & Grizzuti, N. (2020). Special issue: Polymer engineering rheology. In *Journal of Polymer Engineering* (Vol. 40, Issue 9, p. 713). De Gruyter Open Ltd. <https://doi.org/10.1515/polyeng-2020-0223>
- Virtanen, P., Gommers, R., Oliphant, T. E., Haberland, M., Reddy, T., Cournapeau, D., Burovski, E., Peterson, P., Weckesser, W., Bright, J., van der Walt, S. J., Brett, M., Wilson, J., Millman, K. J., Mayorov, N., Nelson, A. R. J., Jones, E., Kern, R., Larson, E., ... Vázquez-Baeza, Y. (2020). SciPy 1.0: fundamental algorithms for scientific computing in Python. *Nature Methods*, 17(3), 261–272. <https://doi.org/10.1038/s41592-019-0686-2>
- Vyazovkin, S. (2020). Activation energies and temperature dependencies of the rates of crystallization and melting of polymers. In *Polymers* (Vol. 12, Issue 5). MDPI AG. <https://doi.org/10.3390/POLYM12051070>
- Wang, S., Sankaran, S., Wang, H., & Perdikaris, P. (2023). AN EXPERT'S GUIDE TO TRAINING PHYSICS-INFORMED NEURAL NETWORKS. *ArXiv*, [abs/2308.08468](https://arxiv.org/abs/2308.08468).
- Wang, Z. H., Li, Y. T., & Wen, F. C. (2023). A Novel In-Line Polymer Melt Viscosity Sensing System of Integrated Soft Sensor and Machine Learning. *IEEE Sensors Journal*, 23(11), 12181–12189. <https://doi.org/10.1109/JSEN.2023.3267682>
- Wilczyński, K. J., Nastaj, A., Lewandowski, A., & Wilczyński, K. (2014). A composite model for starve fed single screw extrusion of thermoplastics. *Polymer Engineering and Science*, 54(10), 2362–2374. <https://doi.org/10.1002/pen.23797>

- Wilczyński, K., Nastaj, A., & Wilczyński, K. J. (2013). Melting Model for Starve Fed Single Screw Extrusion of Thermoplastics. *International Polymer Processing*, 28, 34–42. <https://doi.org/https://doi.org/10.3139/217.2640>
- Wilczyński, K. (1996). A computer model for single-screw plasticating extrusion. *Polymer - Plastics Technology and Engineering*, 35(3), 449–477. <https://doi.org/10.1080/03602559608000931>
- Wilczyński, K., Nastaj, A., Lewandowski, A., Krzysztof Wilczyński, K., & Buziak, K. (2019). Fundamentals of global modeling for polymer extrusion. In *Polymers* (Vol. 11, Issue 12). MDPI AG. <https://doi.org/10.3390/polym11122106>
- Witt, J., & Gish, J. (1996). Intelligent Advisor to Assist Extruder Operators: A Case Study. *Journal of Plastic Film & Sheeting*, 12(3), 180–194. <https://doi.org/10.1177/87560879960120030>
- Worth, R. A., Parnaby, J., & Helmy, H. A. A. (1977). Wall Slip and Its Implications in the Design of Single Screw Melt-Fed Extruders\*. *Polymer Engineering and Science*, 17(4). <https://doi.org/10.1002/pen.760170409>
- Xie, H., Li, C., & Wang, Q. (2023). Thermosetting Polymer Modified Asphalts: Current Status and Challenges. *Polymer Reviews*, 64(2), 690–759. <https://doi.org/10.1080/15583724.2023.2286706>
- Yue, L., Guo, H., Kennedy, A., Patel, A., Gong, X., Ju, T., Gray, T., & Manas-Zloczower, I. (2020). Vitrimerization: Converting Thermoset Polymers into Vitrimers. *ACS Macro Letters*, 9(6), 836–842. <https://doi.org/10.1021/acsmacrolett.0c00299>
- Yusuf, I., Iksan, N., & Herman, N. S. (2010). *A Temperature Control for Plastic Extruder Used Fuzzy Genetic Algorithms* (Vol. 2). Proceedings of the International MultiConference of Engineers and Computer scientists.
- Zadeh, L. A. (1965). Fuzzy sets. *Information and Control*, 8(3), 338–353. [https://doi.org/10.1016/S0019-9958\(65\)90241-X](https://doi.org/10.1016/S0019-9958(65)90241-X)
- Zhou, K., He, Z., Yin, S., & Chen, W. (2014). Numerical simulation for exploring the effect of viscosity on singlescrew extrusion process of propellant. *Procedia Engineering*, 84, 933–939. <https://doi.org/10.1016/j.proeng.2014.10.518>